Lubricant starvation in elastohydrodynamic large-size spinning contacts

Alberto Porras Vazquez

N°d'ordre NNT : 2020LYSEI109

THESE de DOCTORAT DE L'UNIVERSITE DE LYON
opérée au sein de
INSA de Lyon

Ecole Doctorale N° 162
Ecole doctorale des Sciences pour l'Ingénieur de Lyon : Mécanique, Energétique, Génie Civil, Acoustique (MEGA)

Spécialité/ discipline de doctorat :
Génie Mécanique

Soutenue publiquement le 07/12/2020, par :
Alberto Porras Vázquez

Lubricant starvation in elastohydrodynamic large-size spinning contacts

---

Devant le jury composé de :

Cayer-Barrioz, J.	Directeur de Recherche - HdR (ECL)	Examinatrice
Glovnea, R.	Reader (University of Sussex)	Examinateur
Křupka, I.	Professeur (Brno University of Technology)	Rapporteur
Philippon, D.	Maître de Conférences (INSA-Lyon)	Co-directeur
Seabra, J.	Professeur (University of Porto)	Rapporteur
Vergne, P.	Directeur de Recherche - HdR (INSA-Lyon)	Directeur
Fillot, N.	Maître de Conférences (INSA-Lyon)	Invité
Morales-Espejel, G. E.	Principal Scientist - HdR (SKF RTD)	Invité

Département FEDORA – INSA Lyon - Ecoles Doctorales – Quinquennal 2016-2020

SIGLE	ECOLE DOCTORALE	NOM ET COORDONNEES DU RESPONSABLE
CHIMIE	**CHIMIE DE LYON** http://www.edchimie-lyon.fr Sec. : Renée EL MELHEM Bât. Blaise PASCAL, 3e étage secretariat@edchimie-lyon.fr INSA : R. GOURDON	**M. Stéphane DANIELE** Institut de recherches sur la catalyse et l'environnement de Lyon IRCELYON-UMR 5256 Équipe CDFA 2 Avenue Albert EINSTEIN 69 626 Villeurbanne CEDEX directeur@edchimie-lyon.fr
E.E.A.	**ÉLECTRONIQUE, ÉLECTROTECHNIQUE, AUTOMATIQUE** http://edeea.ec-lyon.fr Sec. : M.C. HAVGOUDOUKIAN ecole-doctorale.eea@ec-lyon.fr	**M. Gérard SCORLETTI** École Centrale de Lyon 36 Avenue Guy DE COLLONGUE 69 134 Écully Tél : 04.72.18.60.97 Fax 04.78.43.37.17 gerard.scorletti@ec-lyon.fr
E2M2	**ÉVOLUTION, ÉCOSYSTÈME, MICROBIOLOGIE, MODÉLISATION** http://e2m2.universite-lyon.fr Sec. : Sylvie ROBERJOT Bât. Atrium, UCB Lyon 1 Tél : 04.72.44.83.62 INSA : H. CHARLES secretariat.e2m2@univ-lyon1.fr	**M. Philippe NORMAND** UMR 5557 Lab. d'Ecologie Microbienne Université Claude Bernard Lyon 1 Bâtiment Mendel 43, boulevard du 11 Novembre 1918 69 622 Villeurbanne CEDEX philippe.normand@univ-lyon1.fr
EDISS	**INTERDISCIPLINAIRE SCIENCES-SANTÉ** http://www.ediss-lyon.fr Sec. : Sylvie ROBERJOT Bât. Atrium, UCB Lyon 1 Tél : 04.72.44.83.62 INSA : M. LAGARDE secretariat.ediss@univ-lyon1.fr	**Mme Sylvie RICARD-BLUM** Institut de Chimie et Biochimie Moléculaires et Supramoléculaires (ICBMS) - UMR 5246 CNRS - Université Lyon 1 Bâtiment Curien - 3ème étage Nord 43 Boulevard du 11 novembre 1918 69622 Villeurbanne Cedex Tel : +33(0)4 72 44 82 32 sylvie.ricard-blum@univ-lyon1.fr
INFOMATHS	**INFORMATIQUE ET MATHÉMATIQUES** http://edinfomaths.universite-lyon.fr Sec. : Renée EL MELHEM Bât. Blaise PASCAL, 3e étage Tél : 04.72.43.80.46 infomaths@univ-lyon1.fr	**M. Hamamache KHEDDOUCI** Bât. Nautibus 43, Boulevard du 11 novembre 1918 69 622 Villeurbanne Cedex France Tel : 04.72.44.83.69 hamamache.kheddouci@univ-lyon1.fr
Matériaux	**MATÉRIAUX DE LYON** http://ed34.universite-lyon.fr Sec. : Stéphanie CAUVIN Tél : 04.72.43.71.70 Bât. Direction ed.materiaux@insa-lyon.fr	**M. Jean-Yves BUFFIÈRE** INSA de Lyon MATEIS - Bât. Saint-Exupéry 7 Avenue Jean CAPELLE 69 621 Villeurbanne CEDEX Tél : 04.72.43.71.70 Fax : 04.72.43.85.28 jean-yves.buffiere@insa-lyon.fr
MEGA	**MÉCANIQUE, ÉNERGÉTIQUE, GÉNIE CIVIL, ACOUSTIQUE** http://edmega.universite-lyon.fr Sec. : Stéphanie CAUVIN Tél : 04.72.43.71.70 Bât. Direction mega@insa-lyon.fr	**M. Jocelyn BONJOUR** INSA de Lyon Laboratoire CETHIL Bâtiment Sadi-Carnot 9, rue de la Physique 69 621 Villeurbanne CEDEX jocelyn.bonjour@insa-lyon.fr
ScSo	**ScSo*** http://ed483.univ-lyon2.fr Sec. : Véronique GUICHARD INSA : J.Y. TOUSSAINT Tél : 04.78.69.72.76 veronique.cervantes@univ-lyon2.fr	**M. Christian MONTES** Université Lyon 2 86 Rue Pasteur 69 365 Lyon CEDEX 07 christian.montes@univ-lyon2.fr

*ScSo : Histoire, Géographie, Aménagement, Urbanisme, Archéologie, Science politique, Sociologie, Anthropologie

Lubricant starvation in elastohydrodynamic large-size spinning contacts

Abstract

This thesis is dedicated to the study of large-size spinning contacts located at the interface between the roller-end and the flange in rolling-element bearings. The main goal of the study is to evaluate the influence of lubricant starvation on the film thickness distribution of the contact and analyze how spinning might affect this mechanism. Due to its importance in the reliability and performance of the bearing, the focus is set of the local minimum film thickness found at the low velocity region of the contact area. To tackle this problem, a dual numerical-experimental approach is proposed.

The film thickness distribution of spinning contacts is investigated numerically by means of a finite element model previously validated by two dedicated test rigs: Jerotrib and Tribogyr. The simulation of different operating, kinematic, geometric and lubrication conditions enables to write an analytic expression for predicting the aforementioned critical film thickness. At the same time, novel techniques to experimentally induce and control starvation in the contact are implemented into both test rigs and their results are contrasted with those of the simulation. It is demonstrated that the effects of spinning and starvation add up, so that the film thickness distribution of the spinning contact remains asymmetric but tends to a more Hertzian, and therefore thinner, distribution when limiting the oil supply upstream of the contact's inlet.

Sous-alimentation des contacts pivotants elastohydrodynamiques de grande taille

Résumé

Cette thèse est dédiée à l'étude des contacts pivotants de grandes dimensions situés à l'interface entre l'extrémité du rouleau et le collet de la bague des roulement. L'objectif principal de l'étude est d'évaluer l'influence de la sous-alimentation sur la distribution d'épaisseur de film du contact et d'analyser comment le pivotement pourrait affecter ce mécanisme. En raison de son importance dans la fiabilité et la performance du roulement, l'accent est mis sur l'épaisseur de film minimale locale située dans la région de faible vitesse de la zone de contact. Pour résoudre ce problème, une double approche numérique-expérimentale est proposée.

La distribution de l'épaisseur de film des contacts pivotants est étudiée numériquement à l'aide d'un modèle d'éléments finis préalablement validé par deux bancs d'essai dédiés: Jerotrib et Tribogyr. La simulation de différentes conditions opératoires, cinématiques, géométriques et de lubrification permet d'écrire une expression analytique pour prédire l'épaisseur critique du film précédent. En même temps, de nouvelles techniques pour induire et contrôler expérimentalement la sous-alimentation au contact sont mises en œuvre dans les deux bancs d'essai et leurs résultats sont comparés à ceux de la simulation. Il est démontré que les effets du pivotement et de la sous-alimentation s'additionnent, de sorte que la distribution de l'épaisseur de film du contact pivotant reste asymétrique mais tend à une distribution plus hertzienne, et donc plus mince, lors de la limitation de l'alimentation en huile en amont de l'entrée du contact.

Contents

Nomenclature

a	[m]	Hertzian contact radius in the direction of flow
A_1, A_2, b_1, b_2, C_1, C_2	[varying]	Constants of the modified WLF model
b	[m]	Hertzian contact radius in the transversal direction of flow
B	[-]	Spin-to-roll ratio ($B = 2\Omega a/u_e$)
C_{pi}	[J/kg/K]	Heat capacity of solid i
C_{sp}	[-]	Film reduction coefficient due to spinning
C_{st}	[-]	Film reduction coefficient due to starvation
C_{el}	[-]	Film reduction coefficient due to ellipticity
c_l	[m·s^{-1}]	Velocity of sound at bubble point pressure
c_v	[m·s^{-1}]	Velocity of sound at wet point pressure
D	[-]	Curvature radii ratio ($D = R_x/R_y$)
E	[Pa]	Young modulus
E'	[Pa]	Equivalent Young modulus
F	[-]	Pressure term in modified WLF equation
G	[-]	Dimensionless material parameter ($G = \alpha^* E'$)
h	[m]	Gap film thickness
h_0	[m]	Rigid body displacement at the contact center
h_c	[m]	Film thickness at the geometrical center of the contact
$h_{c,ff}$	[m]	Fully flooded film thickness at the geometrical center of the contact
$h_{c,m}$	[m]	Central film thickness at the contact outlet
h_f	[m]	Fluid film thickness
h_m	[m]	Minimum film thickness
$h_{m,-}$	[m]	Critical minimum film thickness ($Y > 0$)
$h_{m,+}$	[m]	Local minimum film thickness at $Y < 0$
h_{max}	[m]	Maximum film thickness in the contact area
h_{oil}	[m]	Equivalent film thickness of the oil layer supplied at the contact inlet
H	[-]	Dimensionless gap film thickness ($H = hR_x/a^2$)
H_{oil}	[-]	Dimensionless film thickness of the oil layer supplied ($H_{oil} = h_{oil}R_x/a^2$)
I	[-]	Light intensity
I_n	[-]	Light intensity of reflected beam n
k	[-]	Ellipticity ratio ($k = b/a$)
k_i	[W/mK]	Thermal conductivity of solid i
K_0	[-]	Bulk modulus at environment conditions
K_0'	[-]	Pressure-dependency rate of the bulk modulus
K_{00}	[-]	Bulk modulus at T = 0 K
L	[-]	Dimensionless load parameter (Moes) ($L = G(2U)^{0.25}$)
M	[-]	Dimensionless material parameter (Moes) ($M = W(2U)^{-0.75}$)
m_i	[kg·s^{-1}]	Mass flow in the i-direction
n	[-]	Corrected refractive index
n_0	[-]	Refractive index at rest for the Lorentz-Lorenz correction
n_{mc}	[-]	Refractive index of the fluid
r	[m]	Distance from the contact center (only for point contacts)
p	[Pa]	Pressure
p_H	[Pa]	Hertzian pressure
R	[-]	Film thickness reduction ($R = h/h_{c,ff}$)
r_c	[-]	Relative oil film thickness ($r_c = h_{oil}/(\bar{\rho}_c h_{c,ff})$
R_D	[m]	Disc track radius
R_{ij}	[m]	Radius of curvature of solid i in the j-direction
R_x	[m]	Curvature radius along the x-axis
R_y	[m]	Curvature radius along the y-axis

SRR	[-]	Slide-to-roll ratio
S_P	[m²]	Hertzian contact area
T	[°C]	Temperature
T_0	[°C]	Environment temperature
T_g	[°C]	Glass transition temperature at a given pressure
$T_{g,0}$	[°C]	Glass transition temperature at ambient pressure
p	[Pa]	Pressure
P_{sat}	[Pa]	Bubble point pressure
P_{vm}	[Pa]	Wet point pressure
U	[-]	Dimensionless velocity ($U = \mu_0 u_e/(E' R_x)$)
$\overline{U}_i$	[m/s]	Velocity vector of solid i
$U_{i,j}$	[m/s]	Amplitude of the velocity of solid I in the j-direction
$U_{i,j,0}$	[m/s]	Amplitude of the velocity of solid I in the j-direction at the contact center
$\vec{u}_b$, $\vec{u}_t$	[m·s^{-1}]	Velocity field of the bottom (b) and top (t) surfaces of the solid
$u_{e,j,0}$	[m·s^{-1}]	Entrainment velocity in the j-direction at the contact center
$u_{f,ij}$	[m·s^{-1}]	Velocity field of the lubricant in the i-direction
$u_{i,j}$	[m·s^{-1}]	Velocity of solid i in the j-direction
$u_{i,j,0}$	[m·s^{-1}]	Velocity of solid i in the j-direction at the contact center
w	[N]	Load
W	[-]	Dimensionless load ($W = w/(E' R_x^2)$)
x	[m]	Coordinate in the direction of flow
X	[-]	Dimensionless coordinate in the direction of flow ($X = x/a$)
X_C, Y_C	[m]	Coordinates of the contact in Tribogyr's main frame
X_D, Y_D	[m]	Coordinates of the disc in Tribogyr's main frame
X_P, Y_P	[m]	Tribogyr main frame
X_m	[-]	Critical position of the air-oil meniscus
y	[m]	Coordinate perpendicular to the direction of flow
Y	[-]	Dimensionless coordinate perpendicular to the direction of flow ($Y = y/a$)

α^*	[Pa^{-1}]	Pressure-viscosity coefficient
β_k	[K^{-1}]	Bulk modulus-temperature coefficient
δ	[-]	Elastic deformation of the solids in contact
δ_{ij}	[m]	Film thickness of the oil layer attached to solid j, exiting or entering the contact (i = 1 or 2, respectively)
δ_{mc}	[m]	Distance delay
Δ	[-]	Lubricant rupture ratio
θ	[-]	Fraction film content
λ	[°]	Spin rotation angle
λ_{mc}	[m]	Wavelength of the monochromatic light filter
μ	[Pa·s]	Viscosity
μ_0	[Pa·s]	Viscosity at environment conditions
μ_g	[Pa·s]	Viscosity at the glass transition temperature
ν	[-]	Poisson ration
ξ	[°]	Phase shift of the incident light beam
ρ	[kg·m^{-3}]	Density
ρ_c	[kg/m³]	Density at the contact center
ρ_i	[kg/m³]	Density of solid i
ρ_0	[kg·m^{-3}]	Density at environment conditions
ρ_f	[kg·m^{-3}]	Density of the fluid lubricant
ρ_l	[kg·m^{-3}]	Density at bubble point pressure
ρ_v	[kg·m^{-3}]	Density at wet point pressure

τ_{ij}	[Pa]	Shear stress in the ij-plane
χ	[-]	Lubricant mass ratio in the equivalent gap fluid
ω	[rad·s^{-1}]	Rotational velocity of solid i
Ω_i	[rad·s^{-1}]	Spin rotational velocity component of solid i

Subscript	**Description**
ff	Fully flooded lubrication conditions
st	Starved lubrication conditions
sp	Spinning
ns	No spinning

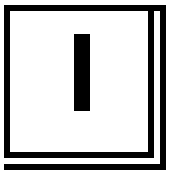

General introduction

The aim of this chapter is to introduce the present thesis, the industrial motivation behind it, as well as the scientific background leading to it. Special emphasis is put into describing the roller-end/flange contact in detail and explaining the different mechanisms and aspects reported to have an impact on its behavior (e.g. spinning kinematics). An outline with the structure of the present work is given at the end of the chapter.

1.1. Foreword: rolling-element bearings and industrial motivation

Rolling-element bearings are mechanical components that are conceived with two goals in mind: (a) to support and guide rotating or oscillating machine components (i.e. shafts, axis or wheels); and (b) to transmit the movement and loads between them with minimal friction. Reduced friction levels constitutes one of the main assets associated to bearings. Indeed, rolling elements are introduced as a mean to induce rolling friction, which is generally 2 to 3 orders of magnitude smaller than classical sliding friction. As a result of it, smaller energy losses due to friction are generated. Rolling-element bearings can come in different sizes and shapes depending on the application they are integrated. They can be used in common devices, like printers or day-to-day transportation, as well as in more complex systems, such as heavy industrial machinery, wind turbines, planes or spacecrafts.

For bearing manufacturers, understanding how bearings will behave when faced to specific operating conditions is vital. The design of these components not only has to comply with up-to-date standards and regulations, but they also have to keep up with the high levels of quality, performance and reliability that are demanded from them. The growing environmental awareness in the industry and their interest for more environmental compatible products has also motivated companies to look into those aspects, tightly related to the bearing's performance (e.g. reduction of the bearing's lubricant consumption or energy needs). Among the many contacts that can be found in rolling-element bearings, the roller-end/flange contact represents a crucial design point because of the high power losses and harsh operating conditions attributed to it. The contact is described by different multiphysical phenomena. Due to the high curvature radii of the region (of the order of tens of millimeters, if not more), the roller-end/flange contact is defined by a narrow gap between the sold bodies as well as a large size contact area that the lubricant can hardly access in acceptable amounts. Moreover, a complex kinematic field acts on it and temperature elevations in the area can lead to substantial power losses (i.e. efficiency reduction). The rheology of the lubricant is hence significantly affected and so the film thickness layer separating the surfaces in the contact undergoes shear-thinning. In this sense, the contact may be exposed to an insufficient film thickness during its operation. Thus, the surfaces may endure wear and damage and the bearing might ultimately fail.

At this point, one can highlight the importance of having a reliable numerical tool able to replicate the conditions of the contact and its immediate environment. In addition to it, adequate experiments are required to validate the modelling assumptions and hypothesis chosen. This also includes the characterization of the rheological behavior of the lubricant through rheometers and viscometers. This may appear to be a long or tedious process, but it offers meaningful advantages, aside from the validation of one approach by the other. The numerical tool might also render itself useful in allowing to study particular areas which would be difficult or impossible to access experimentally. Furthermore, one might be able to simulate operating conditions that would otherwise be difficult to perform with a test rig or require too much time investment or resources.

1.2. Structure of a rolling-element bearing

Figure 1.1 shows a diagram illustrating the different components of a ball bearing. The main structure of the bearing is formed by two coaxial rings with distinct diameters. The existing gap between both rings is filled with a given number rolling elements. The interface between these and the inner surfaces of the rings is flooded with either lubricanting oil or grease. A cage is generally added to guide the rolling elements and space them evenly, reducing direct contacts between them and so friction. A sealing mechanism such as shields or seals can also be introduced. Sealing keeps the lubricant inside the bearing and prevents any access of external contaminants into the interior, thus prolonging the bearing's service life.

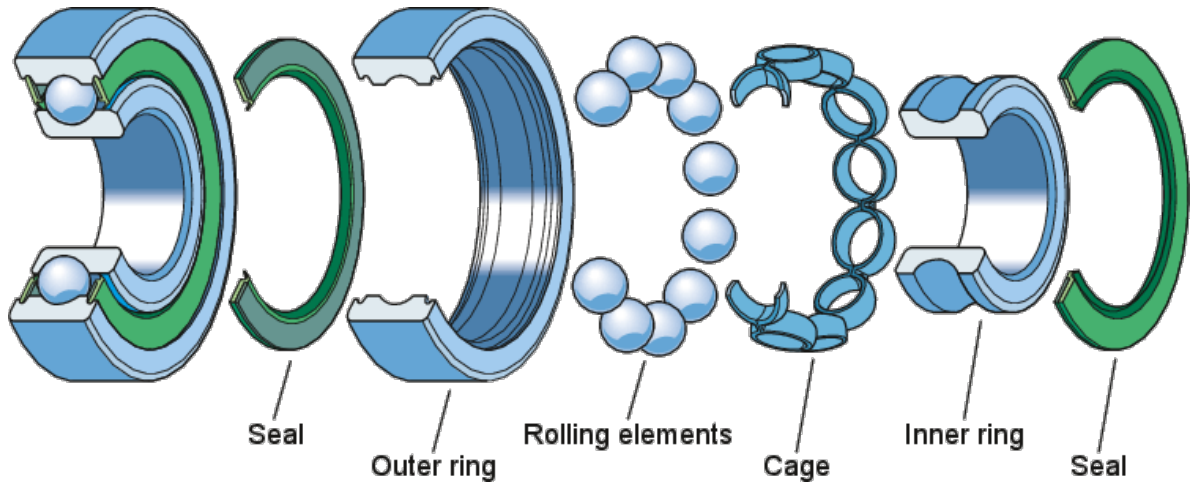

Figure 1.1. Components of a ball bearing (source: SKF Group).

As indicated above, the contact studied herein concerns the roller-end/flange contact (see Figure 1.2) as those found in roller bearings. Flanges are common elements in tapered, spherical and cylindrical roller bearings. They are usually located at the inner sides of both rings and mate with the end tips of the rolling elements. Flanges serve to keep the rolling elements contained within the rings. Additionally, they are important in transmitting the axial loads from the outer ring, where they are applied, to the inner ring. The size and the geometry

of the roller-end/flange contact is directly linked to the design of the roller bearing and the operating conditions it performs.

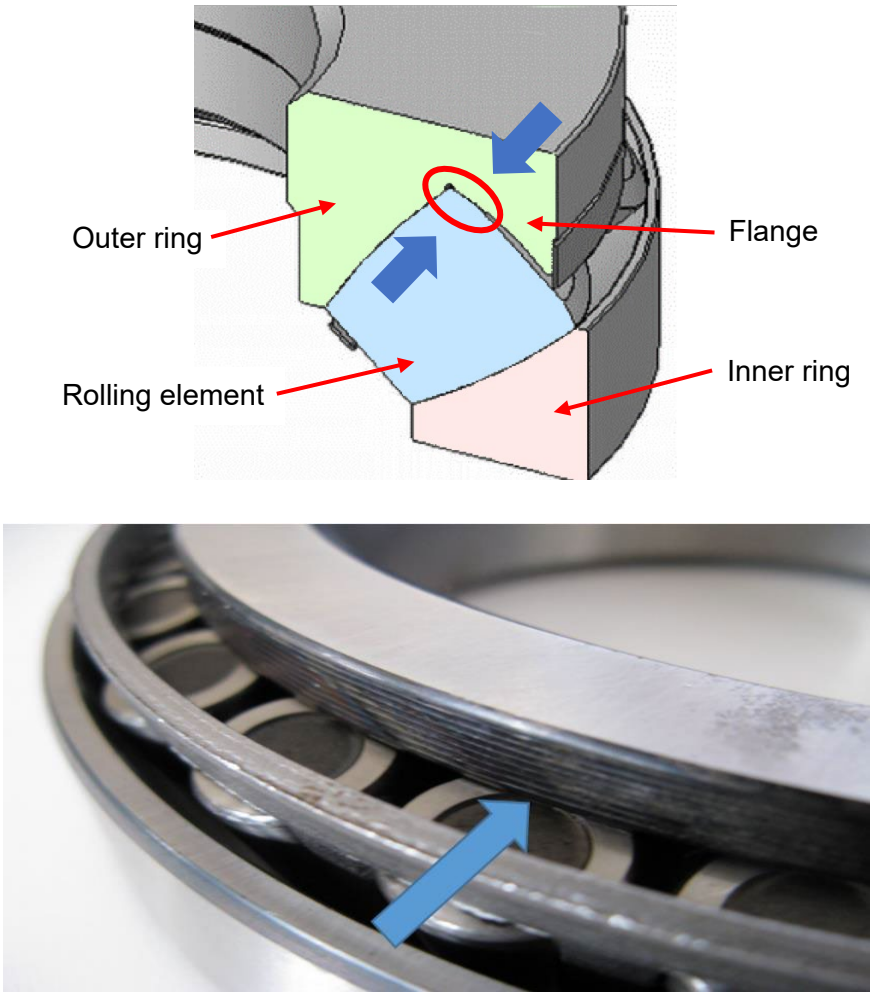

Figure 1.2. Upper row: location of the roller-end/flange contact (marked in a red ellipse) in a tapered bearing. The blue arrows indicate the load exerted by the two elements in contact. Lower row: industrial roller bearing (from [1]), with a blue arrow pointing to the location of the roller-end/flange contact.

1.3. The elastohydrodynamic lubrication regime

Consider the contact between the roller-end and the flange, with a film of lubricant separating both surfaces. The oil film is subjected to a vertical load and its flow follows a sliding-rolling movement. The contact is said to operate in the elastohydrodynamic lubrication (EHL) regime when (a) the load is sufficiently high to deform the solids elastically similar orders of magnitude as the film thickness of lubricant entrapped (in the range of 0.1 to 1 μm), and (b) when the contact pressure is high enough to generate a substantial increase of the lubricant viscosity [2] [3].

The film thickness initially develops upstream of the contact zone from the Couette flow generated by the movement of the solids, which drags the lubricant between their surfaces.

As the lubricant arrives at the contact inlet, the deformation undergone by both bodies creates a pressure gradient and, in turn, a pressure dependent Poiseuille flow pushes the lubricant outside the contact. At the same time, the high pressures increase the viscosity of the fluid almost exponentially due to the piezoviscous effect, thus reducing its ability to flow. Thus, the amount of lubricant ejected is significantly reduced, allowing the formation of a constant film. On the other hand, the steep decrease of the pressure field at the contact outlet, accompanied by an equal reduction of the lubricant viscosity, results in a much more important Poiseuille flow. In order to balance its effects and ensure the continuity of the flow, the flow's mean velocity has to rise. This is accomplished by the formation of a constriction at the same location, whose direct consequence is observed in the creation of a pressure spike upstream of it.

1.4. The roller-end/flange contact

Despite its importance, the literature on the roller-end/flange contact is quite limited. As a result of it, over the past years, several dedicated studies have been conducted at the Laboratory of Mechanical Contacts and Structures (LaMCoS). In this context, in 2008 Habchi [4] first developed a finite element model to simulate circular contacts operating under non-Newtonian and isothermal conditions. At the same time, Dormois [5] extended the numerical model to account for the particular kinematics of the roller-end/flange contact and evaluated its influence on friction forces. A dual experimental-numerical methodology was adopted. A dedicated test rig for studying large-size contacts, Tribogyr [6], was built in collaboration with the SKF Group for this occasion. In the years to come, Doki-Thonon and Wheeler extended the work on the roller-end/flange contact following a similar strategy. In 2012, Doki-Thonon [7] focused his study on the thermal effects and power dissipation endured by the contact, as well as on the film thickness measurement implementation on Tribogyr. Lastly, in 2016, Wheeler [1] analyzed the impact of the roller geometry on the performance of the contact. With every work, both the test rig and the computational model were adapted to the specific operating conditions of the study. Regardless of the progress made, some research aspects of the roller-end/flange contact are still left to be covered. The following sections give a brief description of the general knowledge available on this type of contact, as well as the conclusions extracted in the most recent studies.

1.4.1. Contact kinematics: spinning and film thickness

The distinctive kinematics of the roller-end/flange contact is the result of combining rolling, sliding, spinning and skewing motions. In rolling-element bearings, as is the case of the present study, spinning and skewing may be induced by the particular tilting of the rolling elements with respect to the flange of the inner ring. Figure 1.3 (left) schematically represents a spinning contact between a spherical-end specimen (solid 1) and a plane (solid 2), with Ω_1 and Ω_2 their respective rotation velocities. Their rotation axis are marked in blue, for solid 1, and in red, for solid 2. The contact area between both elements is shown in yellow. Figure 1.3 (right) shows the kinematic field of the contact area relative to each solid's surface. Spinning introduces additional rotational components into the velocity field. Taking into account Figure 1.3, the spinning conditions would be affected by tilting the roller around the x-axis. Skewing, on the other hand, would result from tilting the roller around the y-axis. Skewing may originate due to friction forces between the mating surfaces, which may in turn depend on the speed, load and

lubrication conditions of the contact system, as well as the clearance between the rolling elements and the cage [8] [9] [10]. Generally, skewing entails the displacement of the contact area onto the flange, thus affecting the relative orientation between the velocity fields of the roller and the flange.

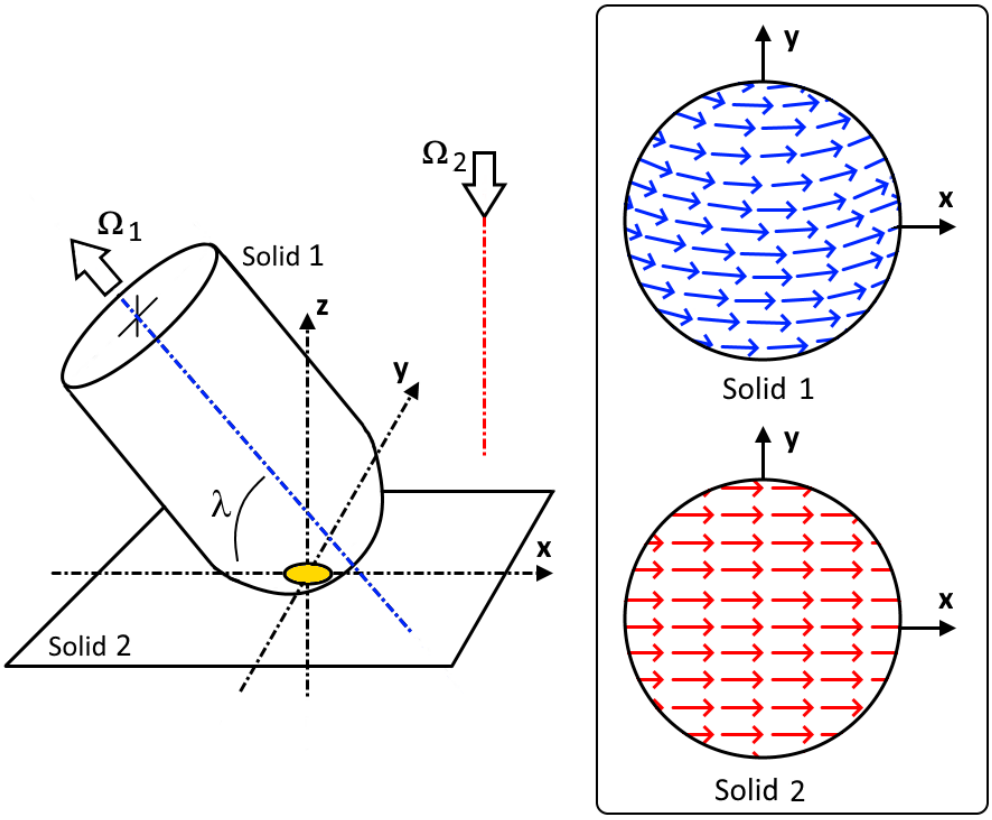

Figure 1.3. Left: schematic representation of a spinning contact between a spherical-end specimen (solid 2) and a plane (solid 1). The contact area is marked in yellow. Right: velocity profile at the contact area on the surface of solid 1 and 2.

The two different rotations endured by the rolling element can be represented with the angle λ for the spinning motion and κ for the skewing motion.

The spinning component of the kinematic field entails important variations in terms of amplitude and direction in its components. These variations in speed result in an asymmetric displacement field, which translate also in the loss of symmetry of the film thickness profile. The local variations of film thickness due to spin were studied in 1991 by Dowson *et al.* [11] for the case of isothermal elliptical contacts under spin and rolling. Their findings were confirmed years later by the works of Yang and Cui [12] and Zou *et al.* [13]. Dowson *et al.* [11] also observed that spin had little effect on the contact pressure field in either shape or magnitude. In their paper from 1993 [14] they pointed out how the pressure profile is flattened by elastohydrodynamic and piezoviscous effects when high loads where applied. Figure 1.4 illustrates the variation of the pressure and film thickness distributions for different spin values, as exposed in [13]. Colin *et al.* [15] obtained similar conclusions to the previous studies when

the contact was operated under starved lubrication conditions. This contrasted with the findings from Liu *et al.* [16], who demonstrated pressure variations in the contact area due to skewing.

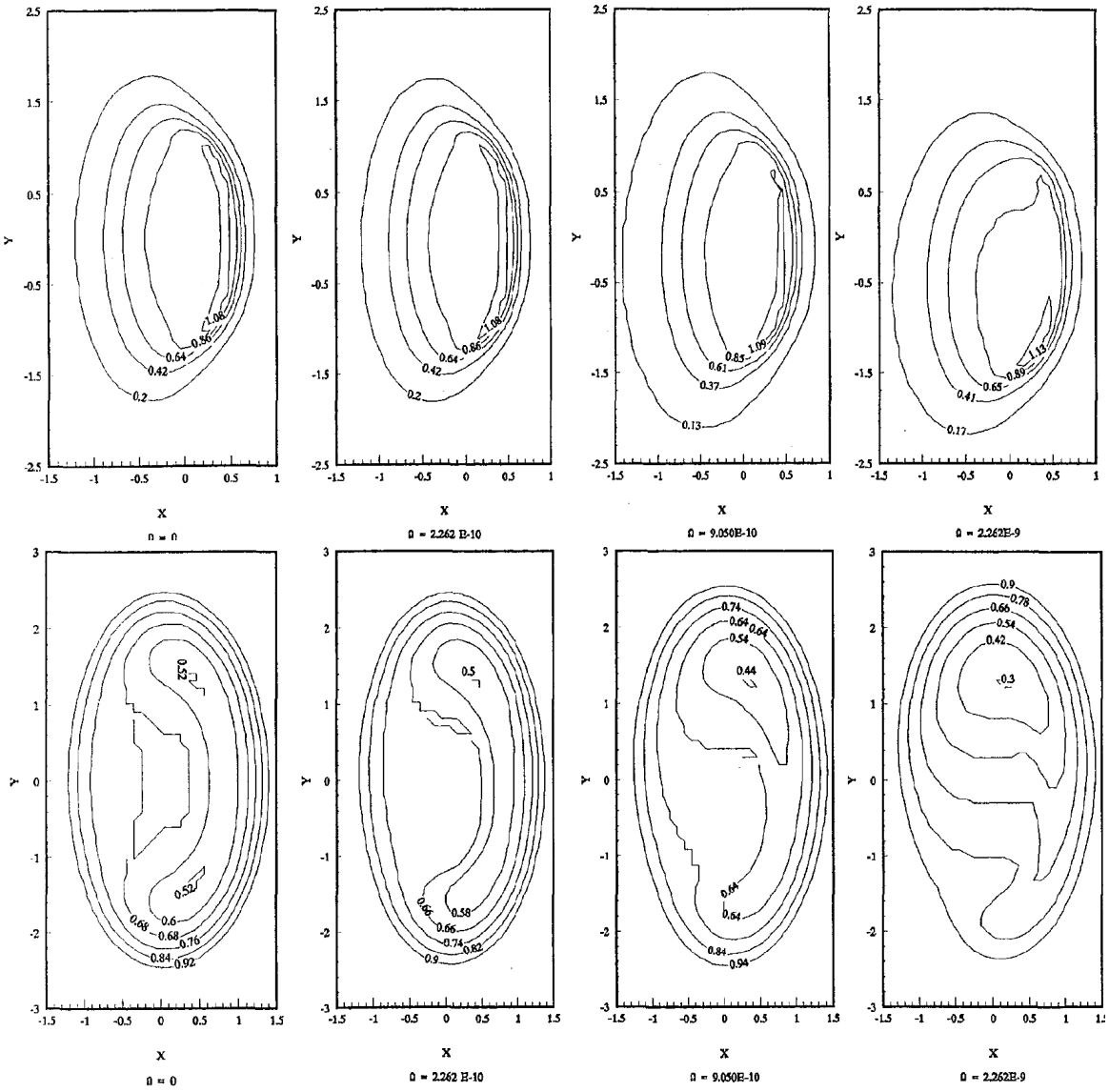

Figure 1.4. Contour plots of pressure (top) and film thickness (bottom) for different spin values, from [13] (spin increases from left to right).

Some analytical expressions for determining the film thickness in isothermal elliptical contacts with spin can be found in the literature. Taniguchi *et al.* [17] developed in 1997 a formula for predicting the minimum film thickness in those contact, based on a reduction factor. In this case, the new prediction was constructed on the Hamrock and Dowson formula [18] [19]. Similarly, Zou *et al.* [13] derived in 1999 approximated expressions for the geometrical center of the contact and the minimum film thickness. These were regressed solely from the computational results of their model.

1.4.2. Friction and shear stresses

The study of friction in spinning contacts is tightly linked to the evaluation of shear stresses and variations of temperature. The effects of spinning on the friction level have been observed both numerically [20] [21] and experimentally [22] [23] [22] by several authors. In both circumstances, the results reveal a clear reduction of friction with spin, regardless of the pressure, temperature or speed conditions. However, the initial intent of the investigations was not to understand the mechanics behind the phenomenon, but rather to develop empirical predictive models to estimate the power losses induced by spinning [20] [24] [25].

The general shape of the friction profiles with the slide-to-roll ratio (SRR) can be observed in the set of curves of Figure 1.5 [26]. They correspond to the numerical results of a Ree-Eyring rheological model. The curves are traced for isothermal conditions and for different λ values, ranging between 1° and 90°. The friction values are determined at the contact center. When there is no spinning motion (i.e. λ = 90°), the longitudinal friction coefficient is seen to rise rapidly with small SRR values. Then, a plateau-like region follows, caused by the limitation of the viscosity, induced by the shear stress. Lastly, a slight decrease is experienced because of thermal effects; these were quantified by Tevaarwerk in [24]. By increasing spinning (reducing λ), the slope of the curves decreases for kinematic conditions close to pure rolling and the friction values are overall smaller. In the case of the transverse friction coefficient, an absolute maximum is achieved for SRR = 0 and no spin. When increasing spinning (reducing λ), the initial peak becomes thicker and eventually turns into a plateau, where the friction coefficient becomes independent of the rolling-sliding conditions. Regardless of it, the transverse friction coefficient is two orders of magnitude smaller than the longitudinal values. Experimental validation of these two sets of curves is given in [5].

The work from Dormois [5] managed to bring some light into the mechanism behind the reduction of friction with spinning. An isothermal finite element model allowed the author to observe the influence of the shear stress in the contact area. In the case of the longitudinal shear stress, the contact area is divided into two separate regions with opposite shear stress behavior, its maximum value being constant with spin. The velocity of the solids and the rolling-sliding conditions move the limit between both areas and change their relative size. On the other hand, while similar regions with opposite sign are shown for the transverse shear rate, its local maxima increases with spin and its average value is almost negligible. Overall, the high shear stress values decrease the lubricant viscosity. In addition, Dormois suggested that important local shear stresses may produce a temperature rise. This would also decrease the viscosity of the fluid and, in turn, friction. Later experiments conducted by Dormois on Tribogyr confirmed this temperature rise.

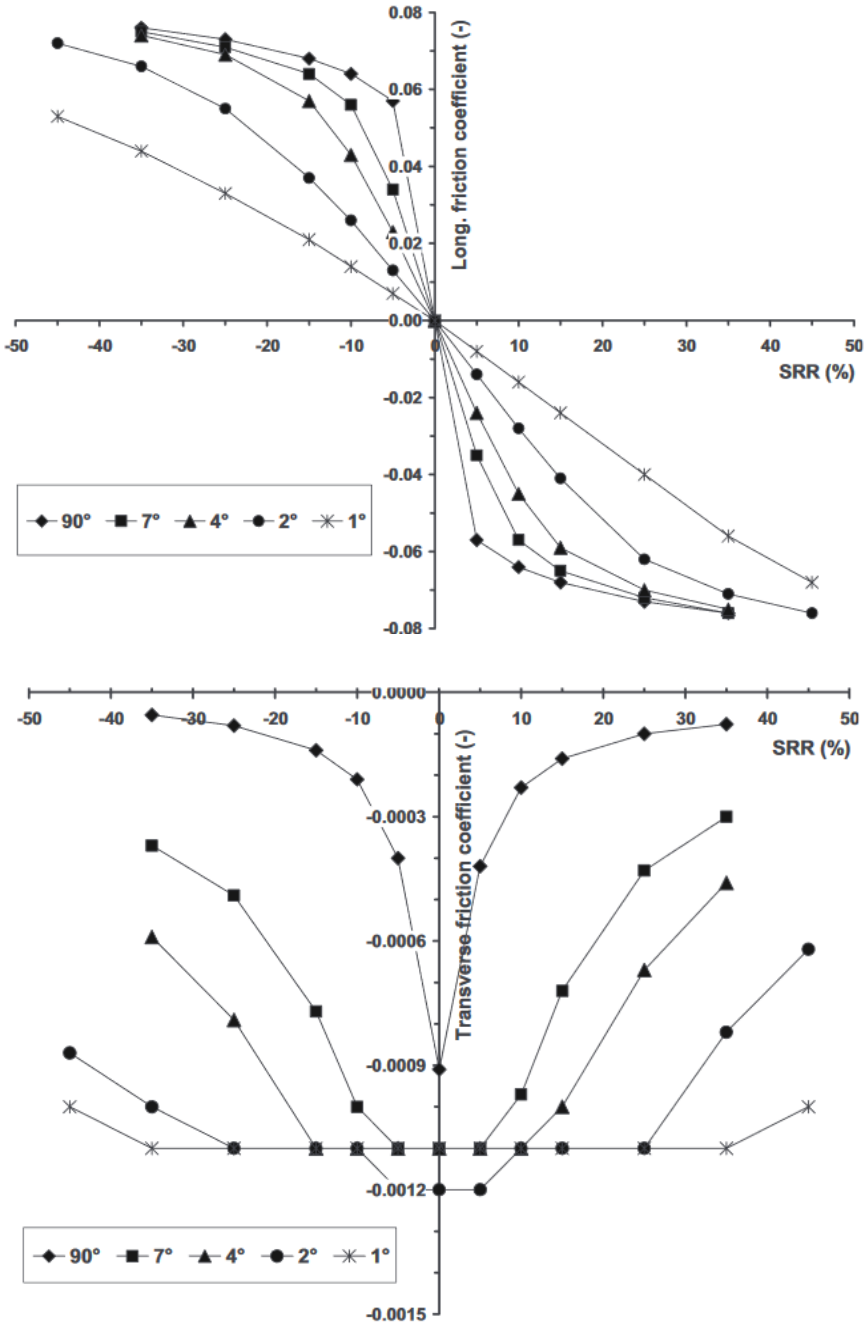

Figure 1.5. Longitudinal friction coefficient (up) and transverse friction coefficient (down), as a function of the slide-to-roll ratio and for different spin angles. Numerical results of a Ree-Eyring rheological model, from [26].

1.4.3. Thermal dissipation and non-Newtonian effects

Many isothermal Newtonian studies on spinning point out the necessity of applying thermal and accurate rheological conditions for a better prediction of the contact's behavior [26] [27] [28]. Ehret *et al.* [28] studied thermal effects in spinning elliptical contacts by approximating the temperature across the film with a parabolic function. Along the previously stated conclusions,

they noticed the increase of temperature with high entrainment speeds and Hertzian pressures. Moreover, the authors remarked that a Newtonian description of the fluid could lead to non-realistic temperature profiles and discrepancies regarding the local shear stress values. Jiang *et al.* [29] were among the first to include non-Newtonian effects into the thermal calculation of spinning contacts. Their numerical results revealed a temperature rise at the contact inlet and outlet, as well as an asymmetric temperature profile along the main direction. However, the approach followed for the thermal analysis strongly limited the evaluation of high spin cases. In addition, the authors argued that the application of non-Newtonian conditions might lead to lower temperature variations.

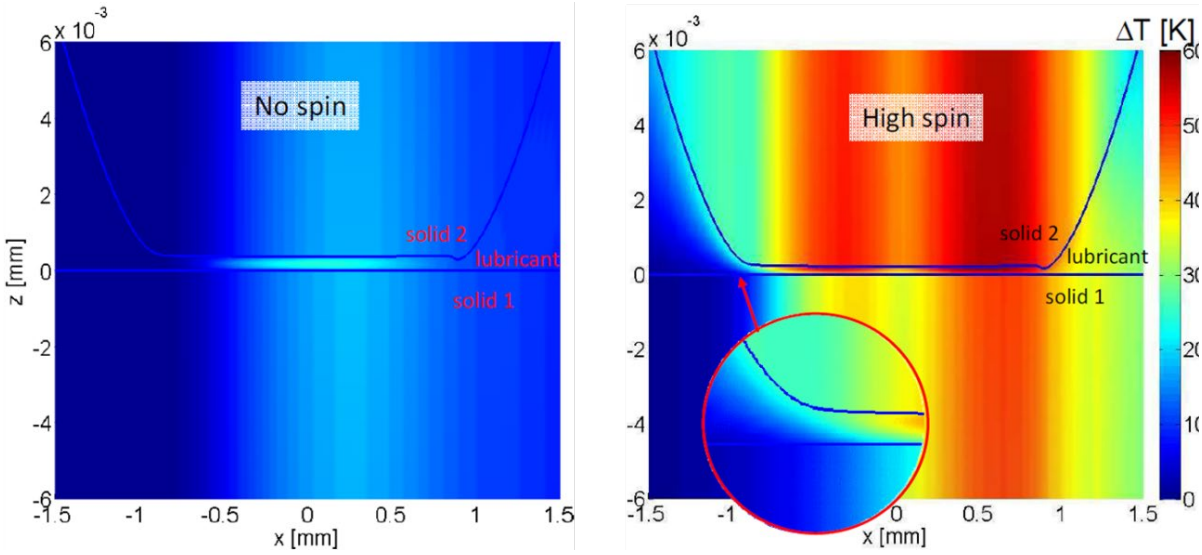

Figure 1.6. Temperature rise (colored area) and film thickness profiles (line) of the same contact with no spin (left) and with spin (right), from [7].

The deficiencies in the calculations performed by Dormois [5] (i.e. consideration of the thermal dissipation) were solved years later by Doki-Thonon [7], who evaluated the temperature rise in the contact area and its immediate vicinity based on an improved computational model. Because of the spinning motion, the heat inside the contact area could not be fully dissipated through the solids, which acted as an additional heat source. Figure 1.6 compares the different thermal behavior of two identical contacts without (left) and with (right) a spin component in its kinematic field. Figure 1.6 (right) shows that the top solid heats up the lubricant at the contact inlet through thermal conduction, as a result of shearing in the center region of the contact. In addition, at high spin, the heated flow exiting the contact is redirected towards the contact inlet. At this region, the lubricant decreases its viscosity by thermal thinning effects and so the overall film thickness in the contact area is also reduced. This phenomenon is seen in the temperature rise of the same contact and its surrounding area, presented in Figure 1.7. The rotating movement of the fluid heats up the lubricant about 25 K before it enters the contact area again.

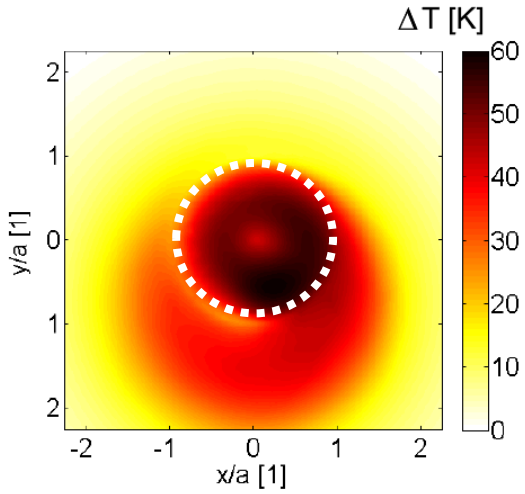

Figure 1.7. Temperature rise of a high spin contact and its surrounding at the lubricant/upper solid boundary, from [7]. The contact area is marked with a dotted circle.

1.4.4. Contact geometry: from circular to torus-on-plane

In the previous sections and cited references, the roller-end/flange contact is assumed to have a circular or elliptical geometry, the circular shape being a specific case of the latter one. However, the roller-end/flange contact can also appear in a highly asymmetrical "banana-shaped" form (see Figure 1.8). This particular geometry results from the individual geometries of the solids in contact as well as the elastohydrodynamic deformations endured by them. For this contact case, Zhang *et al.* [30] delimited the geometry of the roller to either a sphere or a torus portion, whereas that of the flange to a concave spherical or conical surface. Many studies concerning the torus-on-plane contact assume an approximated elliptical shape, and so neglect the effects of the real geometry. Such is the case of the experimental works conducted by Gadallah and Dalmaz [31] and Colin *et al.* [15]. Although the authors manage to recognize the effects of the spin motion, some discrepancies eventually arise when fitting their results to analytical models aimed towards elliptical geometries. In fact, the literature review on circular and elliptical (both slender and wide) contacts is quite extensive and covers a wide range of operating and lubrication conditions, both numerically and experimentally. On the other hand, the references on the torus-on-plane contact are limited.

Wheeler [1] provided additional insights on the torus-on-plane contact regarding its behavior with pressure, film thickness and friction. He also analyzed the validity of approximating its geometry to that of an equivalent slender elliptical contact. He pointed out that this approximation was accurate for most of the cases studied. Nonetheless, with low spin angles (i.e. high spinning motion) the behavior of the inlet streamline differed. Indeed, for the equivalent elliptical model the streamline remained always enclosed within the contact area, but in the toroidal contact the streamline exited and reentered the area. Thus, additional effects, such as diphasic flows or starvation at the inlet, could alter the results expected, in addition to the presence of two active and consecutive contact areas.

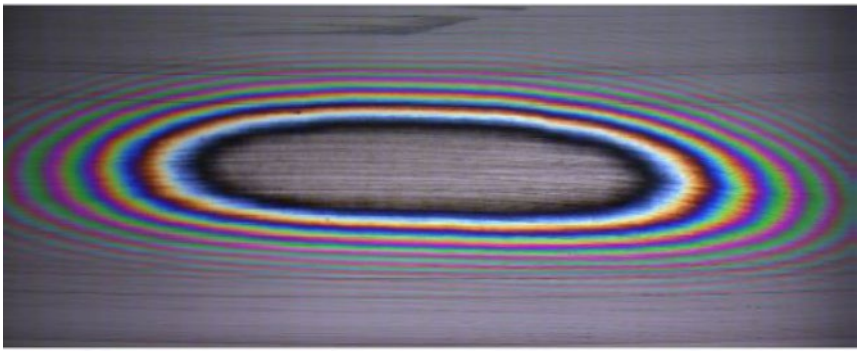

Figure 1.8. Interferogram of a banana-shaped contact created by a toroidal-end specimen and a disc, from [1].

1.4.5. Starvation in spinning contacts

The effects of starvation in the roller-end/flange contact are far from being fully understood. Aside from the work dedicated to it by Colin *et al.* [15], no further research on this topic was able to be found. Colin *et al.* [15] focused on the performance of the contact under typical bearing operating conditions and deduced optimum geometrical and oil supply values for adequate performance levels. They also concluded that friction forces and moments are highly dependent on the inlet oil amount, the bearing speed and the load. One must mention that, prior to it, starvation had been studied extensively as an independent phenomenon for conventional isothermal and Newtonian contacts [32] [33] [34] [35] [36].

The earliest studies on starvation can be traced back to the late 1960s and early 1970s. Back then, there was evidence that specific operating conditions, notably high entrainment speeds and dynamic viscosities, could significantly inhibit the film formation and load-carrying capacity of contacts. Nevertheless, and contrary to what was really observed, the contact inlet was always assumed to be fully flooded. The reader is referred to the experiments of Crook [37], Lauder [38] and Boness [39] for a full in-detail explanation of these early starved results, as well as the numerical solutions of Cheng and Sternlicht [40] and Dowson and Whitaker [41]. Overall, the reduced film thicknesses measurements contradicted the analytical predictions [42]. These differences were associated to the presence of an oil-air meniscus at the contact inlet, whose position in the classical theory is at an infinite distance from the contact. In 1966, Orcutt and Cheng [43] were probably the first to introduce the position of the inlet meniscus as an input condition to study starved line contacts. Thus, a new research direction was opened.

In subsequent years, the specific mechanisms behind starvation and its effects were unraveled. By limiting the lubricant supply, the behavior of the contact can approach that of a dry contact. The air-oil meniscus then comes closer to the Hertzian contact area. With it, the film thickness and friction forces decrease, while traction forces and temperature levels in the region increase. Eventually, the new conditions may differ significantly from the original fully flooded state. Works like those conducted by Wedeven *et al.* [33], Chevalier *et al.* [44], Damiens *et al.* [45] and Svoboda *et al.* [46] introduce numerical and experimental tools to better describe and understand this phenomenon. More on them is described in future chapters.

Another key aspect of starvation many authors were concerned about was the flow patterns followed by the lubricant as it streamed through the contact. Kingsbury [47] suggested the lubricant could either flow in the direction of rolling or move transversally to it, subjected to the pressure gradient of the Hertzian pressure field. As a result of the pressure distribution, oil is depleted from the rolling track by the transverse flow, diminishing the film thickness of the profile. However, he also argued that in the case of roller bearings, where the lubrication conditions should be kept in the long term, the oil expelled transversally had to be balanced by the reflow of the lubricant back into the inlet. This would achieve a starved equilibrium state. In 1976, Pemberton and Cameron [48] experimentally observed the direction of these flows around the contact and related the aforementioned equilibrium to the formation and position of the inlet meniscus. Moreover, the authors also remarked that a spin motion would assist the inlet replenishment process by periodically bringing the oil left from the race side bands or the roller surface. At the same time, they pointed out that the film thickness would fluctuate if starved conditions were in place. Chevalier *et al.* [49] noticed that defects at the contact inlet were not replenished for severely starved conditions. They concluded that, under these conditions, the lubricant in the inlet region behaves asymptotically as a rigid body and hardly any lateral flows occurred. Wedeven *et al.* [33] explained that the oil replenishment was carried out by the excess lubricant accumulated at the sides of the track through surface tension. This idea was confirmed experimentally by Chiu [50]. Cann *et al.* [51] also assumed the effects of surface tension at the vicinity of the contact and quantified the degree of starvation through a non-dimensional parameter including the volume of oil, its viscosity, the contact radius and the entrainment velocity. Following this premise, Nogi *et al.* [52] and Nogi [53] [54] provided a broad insight on the reflow process in circular and elliptical contacts. In their studies, the inlet distance was modelled as a function of the initial film thickness, the capillary number and the ellipticity ratio, and could be applied in conjunction with the classical EHD formulation.

1.5. Outline of the thesis

Although the studies conducted at LaMCoS by Dormois [5], Doki-Thonon [7] and Wheeler [1] on the roller-end/flange contact revealed promising conclusions, the authors assumed fully flooded lubrication conditions. This assumption does not reflect the actual conditions of the contact in roller bearings, especially of large dimensions. Indeed, in a complete bearing, the lubrication conditions of each contact determines the oil supply available for the subsequent one. This implies that the roller-end/flange contact may operate under starved condition. This idea was pointed out by Gadallah and Dalmaz [31], who also highlighted the limited size of the inlet region and its influence on the pressure build-up. The research presented in this thesis builds up on the above works and aims to obtain a better understanding on the influence of starvation in large-size spinning contacts. A dual numerical-experimental approach is implemented for this purpose.

Chapter 1 introduces the industrial motivation behind the study and gives a broad overview of the scientific background that has led to the present work. It also introduces the subject of starvation and spinning motion, which are the two main keystones of the project.

Chapter 2 defines the experimental tools developed and employed. This includes the test rigs and materials used, but also the techniques followed to extract and analyze the information obtained from them.

Chapter 3 defines the numerical tools that have been adapted in this work. This includes the initial finite element model adopted in previous works [4] [5] [7] [1], as well as the modifications implemented to adapt the model to the new operating conditions of the current study. A validation based on experimental film thickness measurements is provided at the end.

Chapter 4 is dedicated to the study of starvation in large-size spinning contacts. The study focuses on describing and quantifying the influence of the lubricant supply upstream of the contact and the kinematic conditions on the film thickness distribution in the contact region. Interferograms of various spinning contacts collected on Tribogyr are analyzed to contrast the numerical results. The study is initially conducted on circular geometries and is later extended to elliptical ones, both wide and slender.

Finally, a general conclusion for the study is drawn and perspectives for future works focusing on the roller-end/flange contact and its specific operating conditions are proposed.

II Experimental modelling of EHD contacts

The main purpose of this chapter is to present the experimental tools and techniques necessary to induce, control and ultimately measure starvation in EHD point contacts. The chapter includes a brief background on the different experimental approaches used throughout time and the limitations found to accurately relate film thickness measurements to a specific starved lubrication state.

2.1. Introduction

When starvation in point contact geometries was initially investigated in 1971 by Wedeven *et al.* [32] [33], the position of the air-oil meniscus located upstream of the contact region was taken as an indicator of the degree of starvation: the closer the lubricant boundary approached the Hertzian contact region, the thinner the film thickness was expected to be found throughout said area. The experiments conducted by Wedeven *et al.* consisted in flooding a ball thrust bearing and measuring its corresponding film thickness after successively removing, cleaning and reassembling its elements several times, until the lubricant was almost removed from all surfaces. These tests proved to be successful and derived in a predictive semi-empirical formula of the film thickness with the lubricant boundary location.

In 1974, Chiu [50] investigated the control of starvation in terms of the operating conditions of the contact by means of a basic ball-on-disc tribometer, by both (a) entraining the test ball with high entrainment speeds and (b) employing high dynamic viscosity lubricants to prevent the oil from flowing back into the rolling track on time. The position of the meniscus was expressed as a function of the entrainment velocity, which was then related to the contact film thickness. When tracing the film thickness with respect to the product of the rolling velocity and the dynamic viscosity, he observed the film thickness to rise monotonically with these two parameters as per the classical lubrication theory for fully flooded contacts [55]. However, the film thickness suddenly collapsed above a certain critical product value (see Figure 2.1), which he attributed to the combined effect of several physical factors (e.g. surface tension, pressure-viscosity index and contact radius). This behavior was reproduced in 1981 by Coy and Zaretsky [56], when they performed film thickness measurements on a 20-mm inner diameter ball bearing with four different lubricants and three test temperatures. They compared their results with the theoretical predictions made by various authors [57] [58] [59] [18] as well as the starvation and inlet shear heating behaviors addressed by Chiu [50] and Cheng [60], respectively. In 1984, Gadallah and Dalmaz [31] also stated similar remarks for the case of elliptical-contact geometries.

Kingsbury [61] studied in 1985 the performance of instrument ball bearings working under lubrication conditions much severe than those of his predecessors. He accomplished that by

introducing small volumes of a solution of lubricant with different concentrations in hexane, and further restricting the supply by evaporating the volume of solvent. Thus, he witnessed nanometer-thin films effectively sustained over time in the absence of a sufficient amount of lubricant at the out-of-contact track, which he coined with the term of parched lubrication. However, it was also noted that the inlet meniscus was no longer measurable. By taking into account the theory of Singleterry [62], Kingsbury argued that no inflow back to the Hertzian area existed during successive ball overrollings.

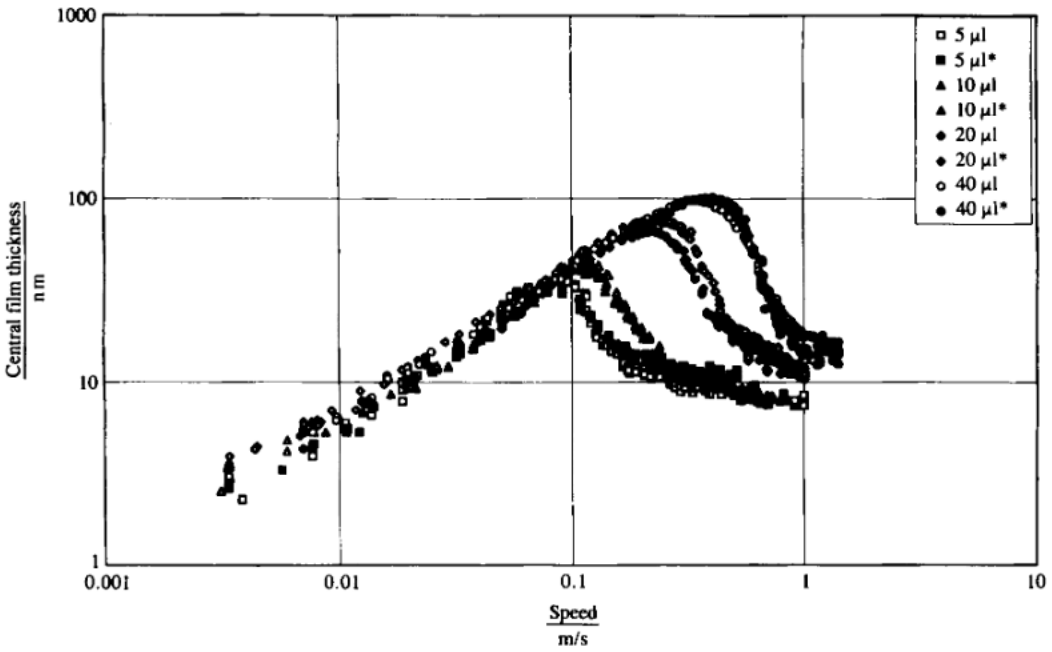

Figure 2.1. Experimental central film thickness variation with entrainment speed for different lubricant supply quantities (extracted from [63]). The experimental measures show similar trends to those previously observed by Chiu [50].

In 1992, Guangteng *et al.* [64] also examined the effects of rolling speed and test time on film thickness in a ball-on-disc test rig equipped with a silica spacer layer. To starve the contact to levels similar to those observed by Wedeven *et al.* [32] [33] and Chiu [50], they applied very small quantities of lubricant on the test ball surface via a micropipette, and sometimes limited even further said amount by wiping it off with a paper tissue. In addition, they conducted the same tests by recreating the starving method of Kingsbury [61]. Likewise, in 1996 Guangteng and Spikes [63] proposed a modification of Chiu's starvation model [50] to include the behavior of the restricted lubricant supply and the different associated phenomena studied in recent years experimentally. Part of their experimental film thickness measurements, shown in Figure 2.1 as a function of the entrainment speed, reveals similar trends as those observed by Chiu [50].

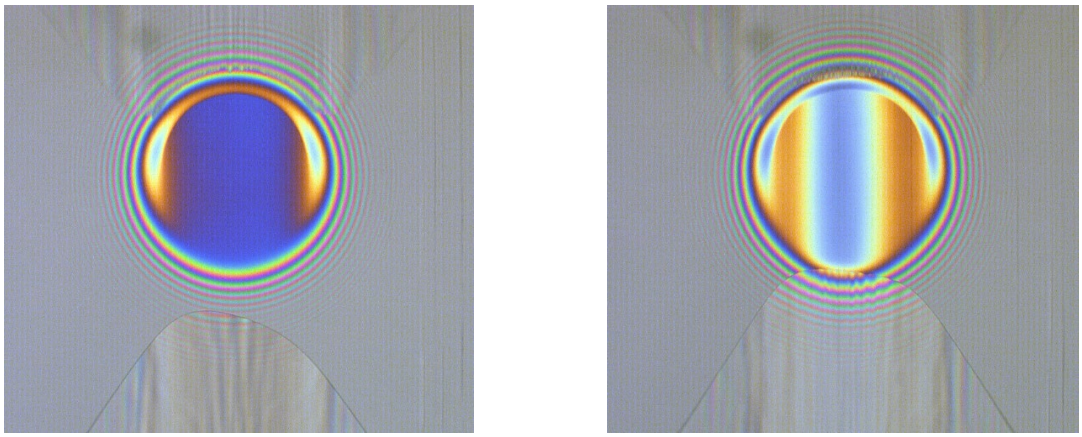

(a) Mild starvation (b) Severe starvation

Figure 2.2. Location of the air-oil meniscus in a mildly and severely starved circular contact. Interferograms obtained with the Jerotrib test rig (see Section 2.2.1) for a fixed entrainment speed and normal load and variable oil supply.

Up to this point, the previously detailed experiences allow to extract some conclusions. Firstly, the location of the air-oil meniscus in not a reliable criterion for predicting the film thickness in the entire range of starvation degrees: from fully flooded to semi-starved, down to severely starved or parched. This is because the inlet meniscus tends to overlap to the edge of the Hertzian area with a limited lubricant supply and becomes unable to be measured (see Figure 2.2). Secondly, varying the entrainment velocity of the rolling elements is not a flexible method to achieve starvation either, as the user is forced to apply velocities that strictly fall above the critical one in order to observe a decrease of the contact film thickness (see Figure 2.1). This means that different degrees of starvation cannot be studied for a given fixed entrainment speed or even in contacts rolling at low entrainment speeds. Moreover, this effect strongly relies on the use of a high-viscosity lubricant. Finally, restricting the amount of lubricant in the system, either through the application of a micropipette or by diluting the lubricant in hexane, proved to be accurate and highly reproducible methods in terms of the resulting film thickness. However, at that time there were no techniques to quantify the exact amount of lubricant supplied to the contact.

In this line, attempts to base experimental starvation measures on the amount of lubricant delivered did not formally start until the 2010s with the work of van der Vegte and Venner [65], who tackled the feasibility of ink-jet drop on demand (DOD) technology to control starved EHL contacts under realistic load conditions. The main aim of their work was to accurately compensate the volume of lubricant expelled from the track through different operating parameters (e.g. droplet frequency). Two years later, van der Kruk *et al.* [66] successfully managed to replicate the behavior of the film thickness predicted by Chevalier *et al.* [44] using the same type of technology. They did so by feeding a dry point contact with variable droplet supply frequencies until reaching flooded conditions, where no film thickness variations were observed. The amount of lubricant found upstream of the contact inlet was estimated from the track length, the drop volume, the entrainment velocity and the contact width. These two studies revealed the versatility of DOD technology in lubrication. Indeed, lubricant can be dispensed at very low volumes (down to a few picoliters!) and therefore contacts can be effectively controlled at high degrees of starvation. However, at the same time DOD technology

presents some important limitations to take into account. On the one hand, the dynamic viscosity plays an important role in delimiting the validity of a lubricant to a certain nozzle geometry. In fact, not every lubricant is compatible with DOD [67]. Generally, high-viscous lubricants will often tend to clog the nozzle; likewise, a lubricant that has not been previously filtered and/or contains small particles can lead to similar adverse results. At the same time, the temperature of the fluid can ease the flow of lubricant at the outlet of the nozzle, but at the expense of affecting the volume dispensed [68].

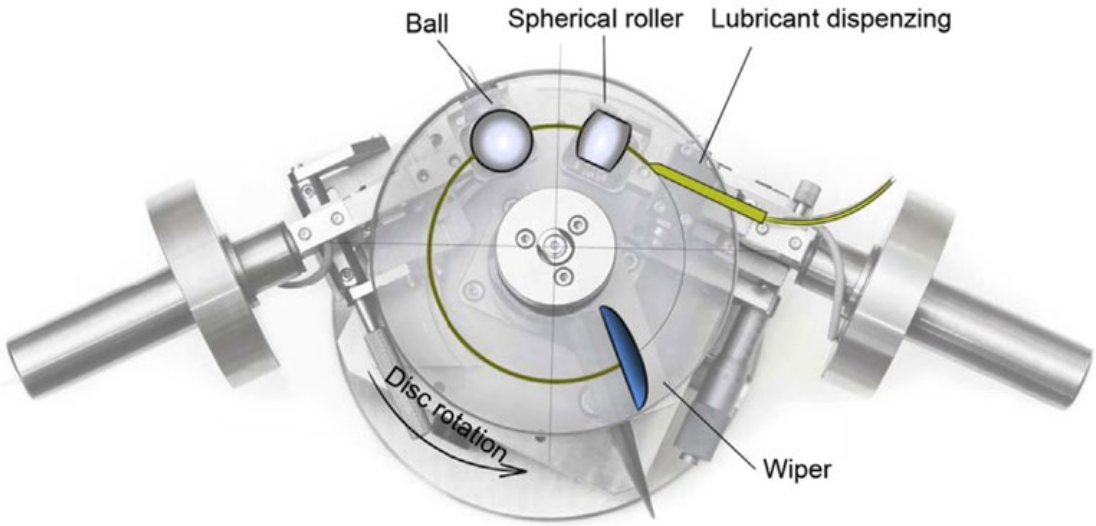

Figure 2.3. Overview of a modified test rig for starved contacts (extracted from [46]).

A few years before the conclusions extracted by van der Kruk *et al.* [66], Svoboda *et al.* [46] and Kostal *et al.* [69] [70] conducted an extensive research aiming to experimentally verify the same analytical model for starved point contacts established by Chevalier and co-workers [44] by following a different approach than the one described above. They mounted their solution on a classic ball-on-disc test rig. They still used DOD technology to feed the test ball with an adjustable lubricant supply, but they also introduced a roller in front of the test ball and a wiper at its outlet, which was used to scrape off the existing lubricant and limit the influence of the lubrication conditions of the ball on the roller (see Figure 2.3). The addition of a roller presented several advantages: (a) it allowed the formation of a uniform (in space) and stationary (in time) film of lubricant feeding the test ball, and (b) it simplified the estimation of the amount of lubricant at the ball contact inlet. Upon successfully meeting their objectives, Svoboda *et al.* applied their modified experimental setup to evaluate the influence of the contact ellipticity on starvation.

Based on the previous set of experimental solutions, this chapter presents a similar approach to that of Svoboda *et al.* [46] in order to control starvation and measure the film thickness profile of starved circular contacts. Opposite to the base solution, the approach finally implemented is simpler in shape and form, as it omits the DOD technology and the wiper and only keeps the additional roller element. The starved conditions of the ball-disc contact are still controlled through the roller-disc contact found upstream of it. The control of the degree of starvation in

the ball-disc contact is ensured by (a) limiting the volume of lubricant upstream of the roller-disc contact over time and (b) maintaining the loads and speeds on both rolling elements constant. In spite of the simplifications made, the results, shown in a future chapter, reveal a good reproducibility and accuracy of the measures to different operating conditions.

2.2. Experimental apparatus

2.2.1. Jerotrib test rig

Jerotib (see Figure 2.4) was initially conceived as a classical ball-on-disc tribometer to evaluate the rheological and physical properties (rheology, film thickness and friction levels) of fully flooded EHL point contacts under different operating conditions. Examples of the various experiments carried out can be found in the works of Molimard *et al.* [71] [72] and Chaomleffel *et al.* [73] and, more recently, in those of Ndiaye *et al.* [74] and Cusseau *et al.* [75].

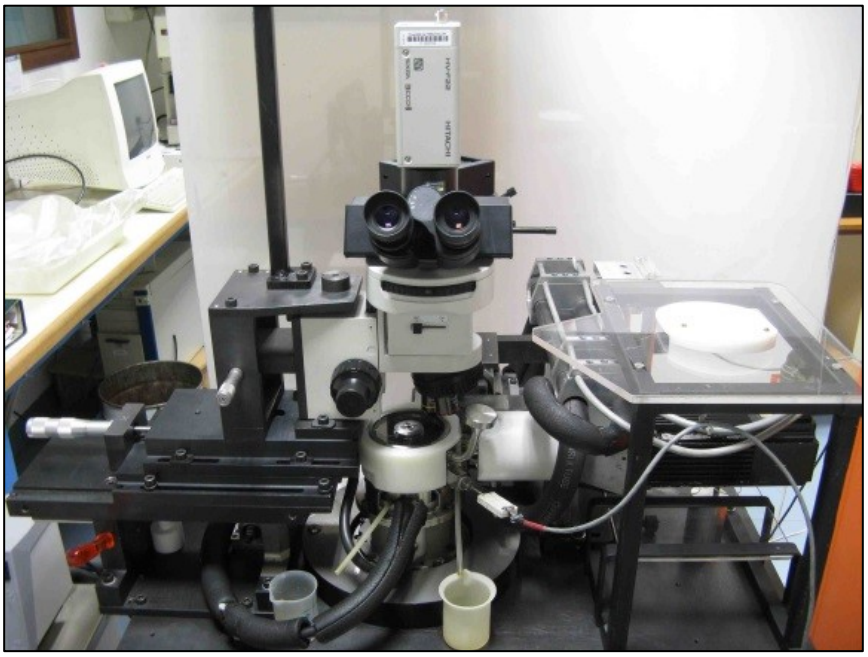

Figure 2.4. Jerotrib test rig.

The core elements of the test rig consist of a disc and a convex specimen. Depending on the application, the nature of these can vary. Typically, the transparent disc is made out of glass or sapphire for film thickness measurements (the sapphire disc being used for high load tests), but it can also be made out of steel or tungsten carbide if other properties are measured, such as friction. The discs employed are generally 80 mm in diameter. However, as it will be indicated in future sections, their dimensions will be enlarged to better fit new elements into the new setup. Moreover, the transparent discs can be coated with a thin semi-reflective chromium layer to improve the film thickness measurements; a silica spacer layer can also be added to further extend the range of measurements. Similarly, the convex sample can be made out of steel or tungsten carbide. Regardless of the material, the curvature radius of the sample

in the entrainment direction R_x is fixed at 12.7 mm and its surface is mirror polished; for the case of steel, the precision achieved is R_{RMS} ≤ 5 nm while for the glass disc R_{RMS} ≤ 3 nm. In the context of the present study, only BK7 glass discs and bearing steel specimens will be considered. Their mechanical properties are summarized in Table 2.1.

Glass disc properties	
Parameter [unit]	**Value**
E_t [Pa]	$82 \cdot 10^9$
ν_t [-]	0.206
ρ_t [kg/m^3]	2510
k_t [W/m/K]	1.114
C_{pt} [J/kg/K]	858

Steel test ball properties	
Parameter [unit]	**Value**
E_b [Pa]	$210 \cdot 10^9$
ν_b [-]	0.30
ρ_b [kg/m^3]	7850
k_b [W/m/K]	50
C_{pb} [J/kg/K]	470

Table 2.1. Mechanical properties of the glass disc and the steel test ball.

Two brushless motors allow to independently drive the rotation of the disc and the test ball between a few millimeters per second and 10 m/s. They are both equipped with optical encoders to assure an accurate control of the sliding conditions. In addition, the test ball can be loaded up to 400 N, so that contact pressures between 0.2 and 3 GPa can be attained, according the nature of the contacting materials.

To lubricate the test ball, oil is filtered and later encapsulated in a thermostatic enclosure; the spindles of both motors are likewise thermally isolated from the environment. With each rotation, the bottom of the test ball dips into the oil reservoir and drags the lubricant up to the contact area, thus ensuring flooded conditions. The temperature of the lubricant can be adjusted with a precision of ± 0.1°C by means of an external thermal control system and a platinum resistance probe located under the ball, opposite to the contact with the disc.

2.2.2. Tribogyr test rig

Tribogyr (from the words TRIBOlogy and GYRation) is a unique test rig built at LaMCoS with the goal of investigating large-size spinning contacts from an experimental standpoint at a 1:1 scale. The test rig, depicted in Figure 2.5, was adapted by Dormois *et al.* [26] [6], Doki-Thonon *et al.* [76] and Wheeler *et al.* [77] to study the influence of spinning on the coefficient of friction, the thermal dissipation and the geometrical shape of the contact, respectively, amongst other parameters. In their research, the contact was always assumed to be flooded. In this thesis, similarly to Jerotrib, the test rig will be again adapted to cover starved lubrication conditions.

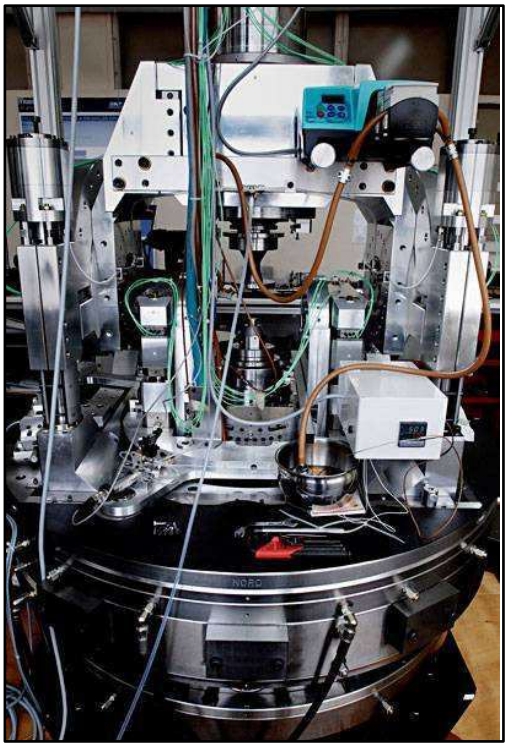

Figure 2.5. Tribogyr test rig.

Tribogyr is 3 m in height and 1.5 m in width and length. It is comprised of two independent assemblies, an upper and a lower one, supporting two separate spindles. Said spindles are used to set in rotation a glass or steel disc, held by the upper assembly, and a pin with a specific end geometry, held by the lower assembly. The rotation velocities achieved can go up to 22000 rpm. The mechanical properties of the disc and the pin are summarized in Table 2.2. Both assemblies are connected to the main frame by means of hybrid bearings, integrating each a hydrostatic thrust bearing and a circular hydrostatic bearing. These elements allow the free rotation of the two assemblies between them and around the perpendicular axis to the base. A vertical load up to 3000 N can be applied on the contact through two pneumatic actuators moving the lower assembly.

Glass disc properties	
Parameter [unit]	**Value**
E_t [Pa]	$72 \cdot 10^9$
ν_t [-]	0.23
ρ_t [kg/m^3]	2500
k_t [W/m/K]	0.937
C_{pt} [J/kg/K]	880

Steel specimen properties	
Parameter [unit]	**Value**
E_b [Pa]	$210 \cdot 10^9$
ν_b [-]	0.30
ρ_b [kg/m^3]	7850
k_b [W/m/K]	50
C_{pb} [J/kg/K]	470

Table 2.2. Mechanical properties of the glass disc and the steel specimen.

A series of sensors are installed throughout the test rig for measuring certain performance parameters.

- Eight tri-axial piezoelectric force sensors are located at the interface between the two assemblies and the hybrid bearings. They are responsible for measuring, on each specimen, the friction forces in the contact plane and the normal load applied along the vertical axis of the test rig.

- Two force sensors attached to the test rig's main frame allow to measure the torques generated on each specimen, perpendicular to the contact plane and centered in the main frame.

- A thermocouple placed inside the pipe supplying the lubricant to the contact measures the temperature of the lubricant at the contact inlet, while a second thermocouple placed onto the disc surface measures the temperature of the lubricant at the contact outlet.

Tribogyr spinning kinematics

The diagram in Figure 2.6 illustrates a schematic representation of the contact between a disc and a spherical-end specimen in Tribogyr from its top view (left) as well as a side view of the spherical-end specimen (right). The contact area is marked by the red-colored region. The center point of the disc is indicated by the coordinates (X_D, Y_D), (X_C, Y_C) is the center point of the contact and R_D the track radius. The spherical-end specimen may be tilted by an angle λ around the x-axis with respect to the z-axis. By doing so, the contact center (X_C, Y_C) and the rotation pole of the spherical-end specimen (X_P, Y_P) cease to be the same. It is by tilting the spherical-end specimen that the spinning conditions in the contact are adjusted. In the following lines, the kinematic fields of the disc and the spherical-end specimen are described.

Using the coordinate system $(\bar{x}, \bar{y}, \bar{z})$ of the spherical-end specimen (see Figure 2.6), the velocity at a point (x, y) on the disc is written as:

$$\bar{U}_1(x,y) = \omega_1 \begin{bmatrix} Y_D - Y_C - y \\ -X_D + X_C + x \end{bmatrix}_{(\bar{x},\bar{y},\bar{z})} \tag{2.1}$$

Similarly, the velocity field of the spherical end specimen at the same coordinate system is expressed as:

$$\bar{U}_2(x,y) = \omega_2 \cos(\lambda) \begin{bmatrix} Y_P - Y_C - y \\ -X_P + X_C + x \end{bmatrix}_{(\bar{x},\bar{y},\bar{z})} \tag{2.2}$$

where ω is the rotation velocity, and the subscripts 1 and 2 denote the disc or the specimen, respectively. Both velocity fields defined in Eq. (2.1) and (2.2) can be put in the general form:

$$\bar{U}_i(x,y) = \begin{bmatrix} U_{i,x} \\ U_{i,y} \end{bmatrix} = \begin{bmatrix} U_{i,x,0} \\ U_{i,y,0} \end{bmatrix} + \Omega_i \begin{bmatrix} -y \\ x \end{bmatrix} \tag{2.3}$$

with subscript i equal to 1 or 2, indicating the element considered. The velocity field can be divided into two independent components. On the one hand, a constant term defining the lineal velocity at the contact center in the x and y-directions, $U_{i,x,0}$ and $U_{i,y,0}$, respectively. A second term driven by the spin rotational velocity Ω describes the spinning kinematics of the contact and is dependent on the location of the point studied.

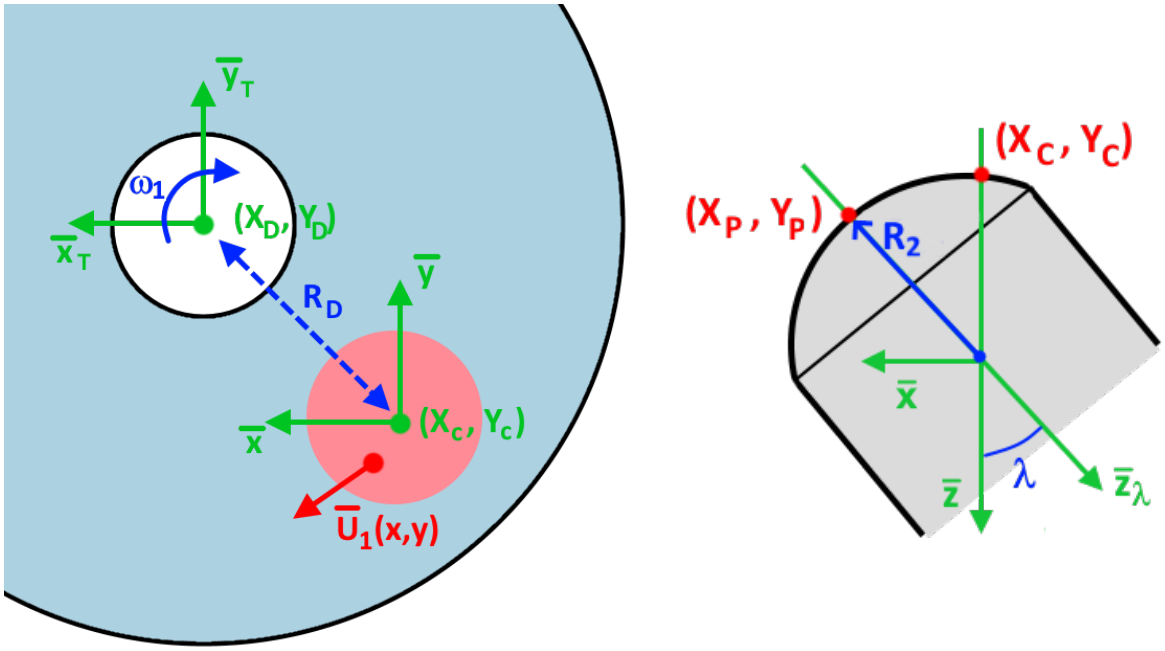

Figure 2.6. Left: top view of a contact between a disc and a spherical end specimen. Right: detail of the spherical-end specimen head. $\bar{z}_\lambda$ is the axis of rotation of the specimen, R_2 is its curvature radius and λ the spin angle.

Ultimately, the velocity tensor of the disc can be defined as:

$$U_{1,x,0} = \omega_1\left(R_D + R_2\sin(\lambda)\right) \quad (2.4a)$$

$$U_{1,y,0} = 0 \quad (2.4b)$$

$$\Omega_1 = \omega_1 \quad (2.4c)$$

and the velocity tensor of the spherical-end specimen as:

$$U_{2,x,0} = \omega_2 R_2 \sin(\lambda) \quad (2.5a)$$

$$U_{2,y,0} = 0 \quad (2.5b)$$

$$\Omega_2 = \omega_2 \cos(\lambda) \quad (2.5c)$$

where R_2 is the curvature radius of the spherical-end specimen. A more detailed description of the kinematic model, as well as an extension of it to include skewing motion, was performed by Doki-Thonon in [7].

2.3. Optical interferometry principles

White light interferometry is an optical image analysis technique for measuring film thickness in EHD contacts that is built on the analysis of interference fringes originated from a unique light source. When compared to alternative methods used in the field, it stands currently as the most reliable one with an ultimate precision below 0.2 nm [71]. A methodology, now known as differential colorimetric interferometry (DCI), was simultaneously devised in 1999 by Hartl *et al.* [78] and Molimard *et al.* [71], and was validated in the next years by Hartl *et al.* [79] [80] for different lubrication regimes. This methodology bases film thickness measurements on chromatic interferograms recorded in the RGB (Red, Green, Blue) color space.

In order to understand the basic principles behind interferometry, one can tackle the optical problem from the perspective of a monochromatic light beam, with a near-normal incidence on the disc surface. The reader is directed to Figure 2.7, illustrating the transmission of a monochromatic light beam across a transparent glass disc and reflected against the surface of a steel test ball. The different intensities are noted as I_i.

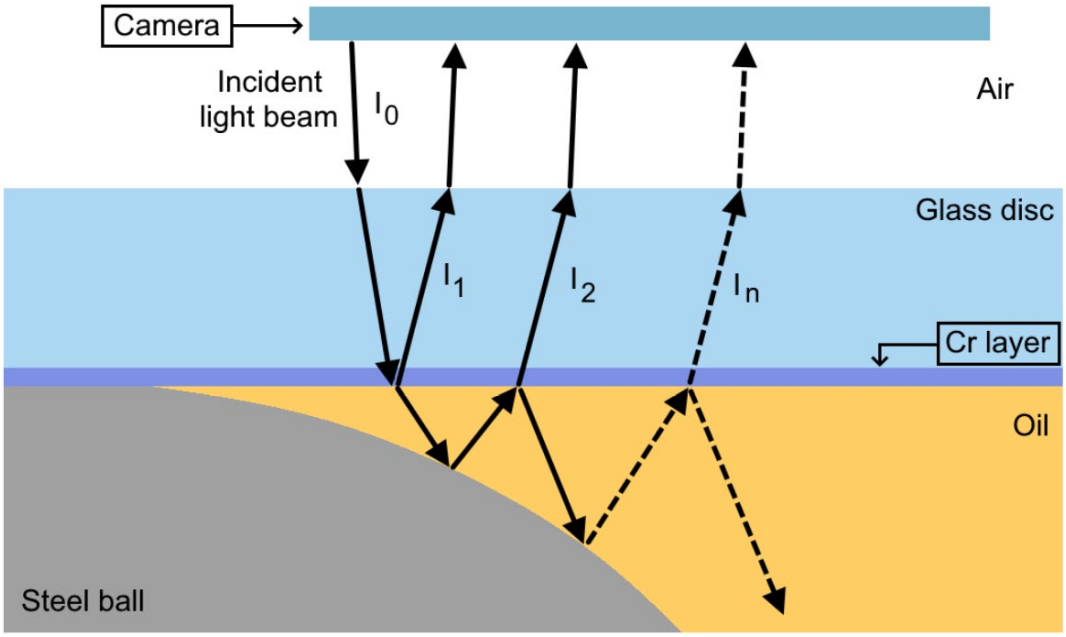

Figure 2.7. Principle of monochromatic interferometry: interference fringes created from a monochromatic light source.

When two waves with intensities I_1 and I_2 pertaining to the same wave train with wavelength λ_{mc} are reflected, they may interact and interfere with each other. These interferences can either be constructive in nature, if the waves are in phase, or destructive, if they are out of phase. Interactions occur whenever a path difference δ_{mc} between the two waves exists. In this case, the resulting intensity of the beam is expressed as:

$$I = I_1 + I_2 + 2\sqrt{I_1 I_2}\cos\left(\frac{2\pi\delta_{mc}}{\lambda_{mc}}\right) \tag{2.6}$$

where the subscript $_{mc}$ stands for monochromatic. Intensities of the transmitted light beams above the order of 2 (I_3 up to I_n) are omitted from the previous calculation. Indeed, one can prove that the contribution of these waves to the total intensity I is negligible, due to the strong intensity attenuation by the Cr layer.

In turn, the path difference δ_{mc} is related to the local film thickness h between the glass disc and the steel ball as well as the refractive index of the lubricant n_{mc}, so that $\delta_{mc} = 2n_{mc}h$. In addition, the light beam undergoes a phase shift ξ when it is reflected against the polished surface of the steel ball. Thus, Eq. (2.6) can be rewritten as:

$$I = I_1 + I_2 + 2\sqrt{I_1 I_2}\cos\left(2\pi\left(\frac{2n_{mc}h}{\lambda_{mc}} + \xi\right)\right) \tag{2.7}$$

Even though the interferences can be easily defined through Eq. (2.7), the periodicity of the function does not allow to find a direct correspondence between the path difference δ_{mc} and the color of the fringes. This limitation invalidates the use of monochromatic interferometry for film thickness measurements. As indicated above, Hartl *et al.* [78] and Molimard *et al.* [71] overcame this issue in 1999 by using a white light source instead. However, the white light beam spectrum is more complex in nature and depends on several environmental and physical factors. Therefore, the procedure suggested by Molimard *et al.* in [71] and illustrated in Figure 2.8 considers comparing the intensity curves extracted from the RGB triplet in a dynamic contact to the experimental calibration curves traced from a static contact.

In the context of the present study, images of the dynamic and static contacts are captured by means of Hitachi HV-F22 3CCD high-resolution camera (1360x1024 pixels). The color in them is decomposed in RGB frames. From the interferogram of the static contact, an initial set of curves relating the intensities of the RGB triplet and their distance from the center of the contact, expressed in pixels, can be obtained. The amplitude of these curves is dependent on the contrast $C = (I_{max} - I_{min})/(I_{max} + I_{min})$. To improve the accuracy of the calibration curves and hence include the range of colors visualized in the dynamic contact, one has to maximize the contrast value. To do so, the use of a chrome-layered disc and the selection of the appropriate camera setup options become crucial. The transcription of the previous relationship in terms of the film thickness is achieved through the analytical expression of Johnson [81], which only accounts for circular contact geometries:

$$h(r) = \frac{r^2}{2R_x} - \frac{a^2}{R_x} + \frac{1}{\pi R_x}\left[(2a^2 - r^2)\arcsin\left(\frac{a}{r}\right) + r^2\left(\frac{a}{r}\right)\sqrt{1 - \left(\frac{a}{r}\right)^2}\right] \text{ for } r \geq a \tag{2.8}$$

with r the distance to the center of the contact, a the Hertzian contact radius and R_x the curvature radius in the x-direction.

The connection established between the light intensities and the film thickness in the static contact applies univocally for the dynamic contact for the range of 0 to 800 nm. Beyond this interval, the contrast drops significantly due to the interference of high-order beams and so the uncertainty of the curves strongly rises.

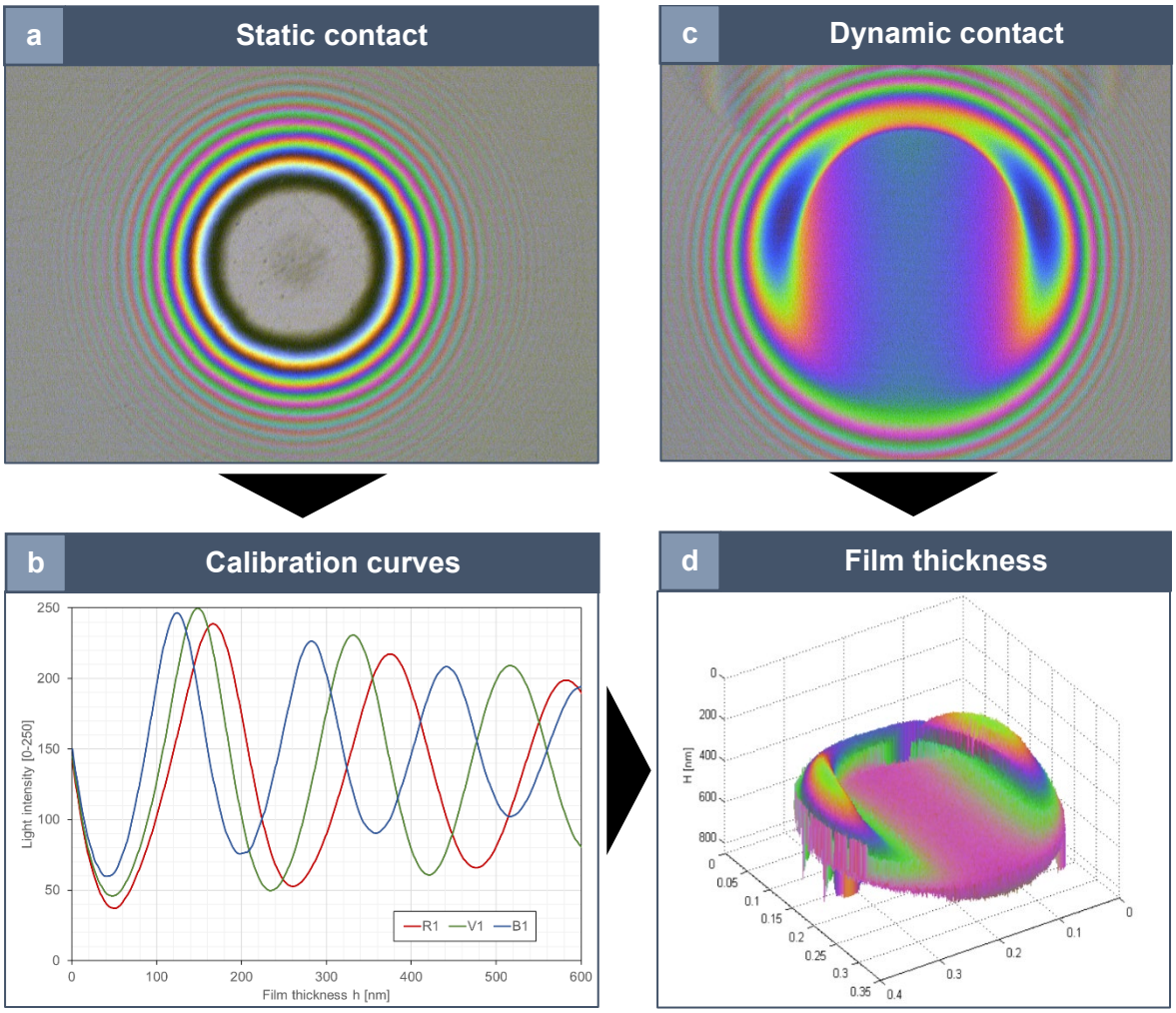

Figure 2.8. Experimental workflow for evaluating the film thickness profile of a contact through differential white light colorimetric interferometry, as described in [71].

However, because the calibration curves are obtained with the lubricant at ambient pressure, whenever measurements are made inside a dynamic contact where the pressure is high, a Lorentz-Lorenz correction [82] has to be applied. Indeed, the density of the lubricant is dependent on the pressure value, therefore its refractive index changes and so does the resulting optical path length from the reflected light beam. To obtain the real film thickness h at a given pressure p, the following adjustment is made, valid at constant temperature:

$$h(p) = \frac{n_0}{n(p)} h_0 \tag{2.9}$$

with n_0 the refractive index of the lubricant at ambient pressure, $n(p)$ the pressure-corrected refractive index and h_0 the apparent film thickness (without correction). The value of n can be determined from:

$$\frac{1}{\rho(p)} \cdot \frac{n^2(p) - 1}{n^2(p) + 2} = \frac{1}{\rho_0} \cdot \frac{n_0^2 - 1}{n_0^2 + 2} \tag{2.10}$$

where $\rho(p)$ is the density of the lubricant at pressure p and ρ_0 the density at ambient pressure. In turn, the value of $\rho(p)$ can be estimated by the appropriate pressure-dependency model from the literature.

Adaptation to elliptical-contact geometries

The previous procedure only allows to obtain calibration curves for circular contact geometries, as the height expression in Eq. (2.8) does not consider alternative contact shapes, such as elliptical ones. To obtain calibration curves that actually fit these kind of geometries, Wheeler *et al.* [83] developed a methodology based on the demodulation work of Badulescu *et al.* [84]. The new approach relates the height variation in a monochromatic interferogram to the RGB triplet from a chromatic picture of the same static contact.

The monochromatic interferogram is obtained with a narrow band-pass filter (632.8 ± 2 nm, full-width half-maximum = 10 ± 2 nm). However, because the phase shift ξ of the incident light beam is now unknown, the value of the film thickness height at the first intensity minimum, and therefore the gap shape at its vicinity, cannot be predicted. To determine this value, a given number of analysis lines perpendicular to the contact boundary are plotted in the monochromatic interferogram. For each analysis line, the position of the first light intensity minimum is identified, the position of the contact boundary being established by a detection algorithm. It is then assumed that for small regions along the analysis lines, Johnson's equation [81] (Eq. (2.8)) can be applied locally. Moreover, the height at the contact boundary is known to be zero and fringes are accepted to increase in height a value of $\lambda_{mc}/2n_{mc}$ with respect to the previous one. Thus, the film thickness at the first fringe can be evaluated with a Newton-Raphson algorithm that minimizes the difference between the analytical result of Johnson's formula and the gap height at the different light intensity minima. Finally, the film thickness in the region between fringes is defined by a cubic polynomial interpolation.

The calculation procedure described in this section is integrated in a software application created with Matlab®.

2.4. Modified test rig for lubricant starvation

2.4.1. Modified structure

As indicated above, the main concept behind the modifications introduced in order to induce, control and measure starvation in point contacts are based on the experimental work carried out by Svoboda and co-workers [46]. Figure 2.9 presents the group of elements constituting the new experimental setup applied to Jerotrib. The orange-colored area represents the circular contact formed by the test ball; the blue-colored area represents the elliptical contact formed by the roller. The yellow discontinuous line indicates the location of the lubricant racetrack, with the yellow circle being the region where the lubrication conditions of the roller are controlled. A white arrow shows the sense of rotation of the glass disc, and thus the lubricant flow.

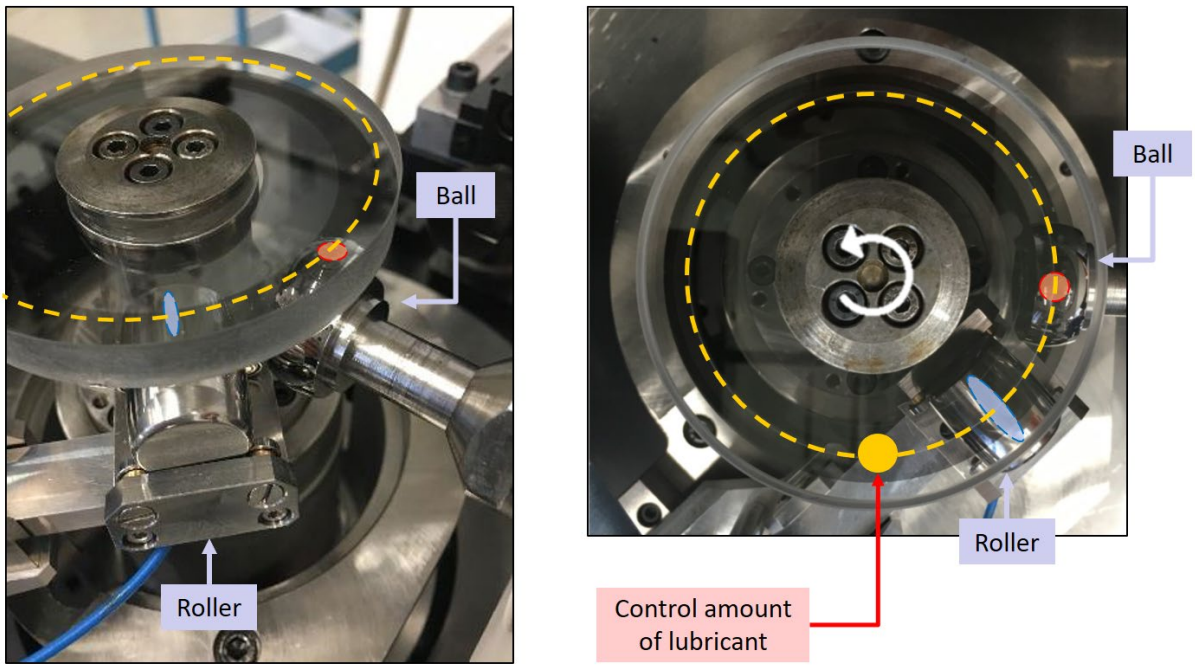

Figure 2.9. Overview of the modifications implemented into Jerotrib.

The core element of the proposed solution is a roller with specific geometric characteristics, which is responsible for generating a quasi-uniform lubricant film that is fed into the ball-disc contact. The main mechanical properties of the rollers used in this thesis are listed in Tab. 2.2. The roller is placed on a carrier at the end of a lever that can be mounted and dismounted from the original test rig. In the carrier, it is supported by four small bearings placed symmetrically (two on each side of the roller), allowing its rotation. The roller can be charged independently with a load of up to 30 N by compressing a spring located at the opposite end of the lever; the desired compression is achieved through a screw at the same lever end. The roller is directly entrained by the rotation of the disc, with its entrainment velocity estimated from its track radius. On the other hand, the test ball is still entrained by its dedicated motor.

Parameter [unit]	Roller 1	Roller 2
$D\ (= R_x/R_y)$ [-]	0.123	0.040
R_x [m]	0.010	0.011
E [MPa]	210	210
υ [-]	0.3	0.3
ρ [kg/m^3]	7850	7850
k [W/m/K]	50	50
C [J/kg/K]	470	470

Table 2.2. Mechanical properties of the rollers.

A load sensor attached underneath of the lever controls the load applied by the user, with the measurements of the load being displayed on a computer screen along with other control

parameters of the setup (e.g. speed, SRR or torque). The minimum load required to assure the rolling of the roller is found around 14 N; below this value, the roller only slides on the disc. This situation is to be avoided, as it can result in damages on the chrome layer of the disc and on the roller's surface, in addition to undesirably inducing severe starvation on the test ball due to a severe film thickness reduction. The critical load value corresponds to the minimum load required by the roller to overcome the friction forces produced between its lateral surfaces and the internal side walls of the carrier. The value of this resistive load is not fixed, it depends on the viscosity of the lubricant employed and the entrainment velocity of the rolling element among other influential factors.

As seen in Figure 2.9, the position of the roller with respect of the test ball is set at an angle of 45° with the center of the disc. Considering the location of the racetrack to be generally found at a radius of around 45 mm to said center, the distance of the roller to the test ball is close enough to prevent significant lubricant side leakages to occur. Thus, it provides a continuous and nearly uniform flow of lubricant into the circular contact. In addition to it, aligning the racetrack of the roller to that of the test ball is crucial to ensure that both contacts are described by the same entrainment speed. The alignment of the two racetracks will also become useful when determining the amount of lubricant supplied to the test ball, as will be seen in Sec. 2.4.4. However, contrary to the test ball, the velocity of the roller is entrained and controlled directly through the movement of the disc. This entails that the disc and the roller will always have the same speed, which implies an equal distribution of lubricant between both rotating surfaces.

2.4.2. Experimental procedure

Because two contacts are now in place (instead of only one in the original configuration) and only one camera is available to capture each of their interferograms, the existing experimental procedure has to be adapted to register variations in the lubrication conditions in both contacts whenever any changes occur. As shown in Figure 2.10, the aim is to have a pair of interferograms relating the lubrication conditions in the roller-disk contact to those found in the test ball-disk contact at any given time, assuming both states are stationary; the importance of this is revealed in a later section. The measurements indicated below each contact in Figure 2.10 refer to the mean film thickness values obtained from a series of interferograms. $\mathrm{h_c}$ is the film thickness at the contact center, $\mathrm{h_m}$ the minimum film thickness in the contact area (generally associated to the side lobes) and $\mathrm{h_{c,m}}$ the minimum film thickness along the central line in the entrainment direction. The experimental procedure implemented is summarized in the following points.

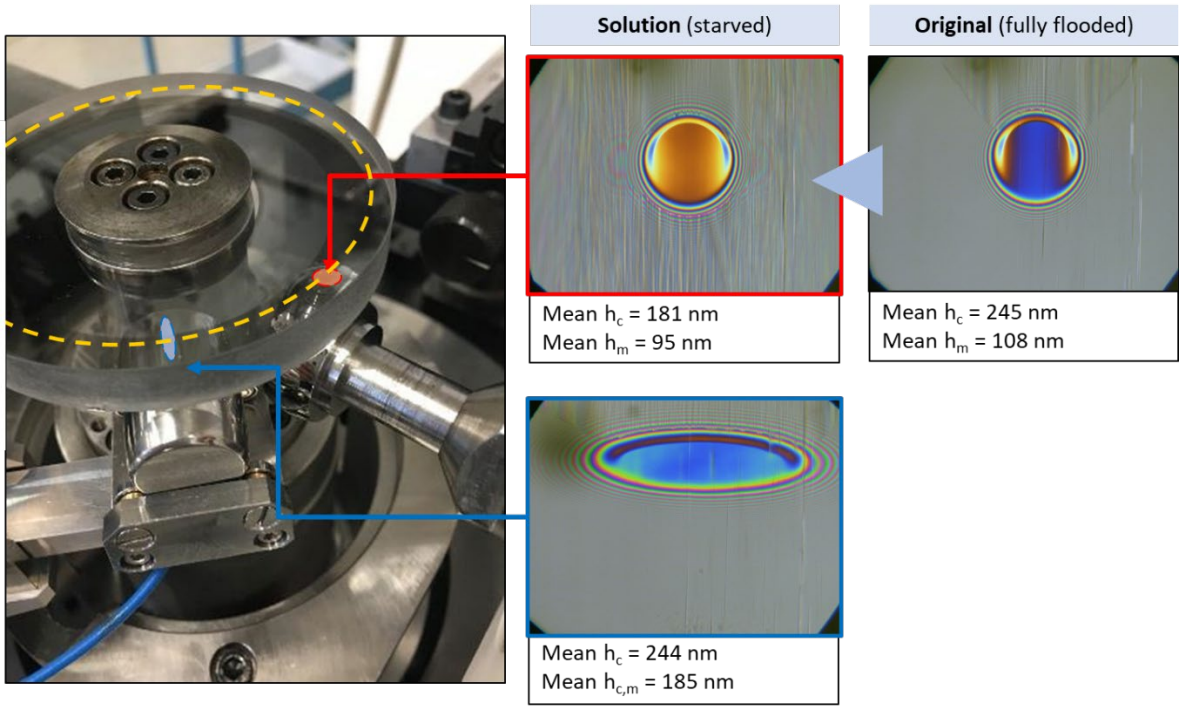

Figure 2.10. Starvation process of a circular contact by a roller in Jerotrib.

Step 1: Before the start of the experience, and after configuring the appropriate camera setup options, a sufficient amount of lubricant is smeared on the lower surface of the disc in order to assure fully flooded conditions in the circular contact.

Step 2: The high-definition camera is placed over the ball-disc contact region.

Step 3: A dynamic contact is performed with the test ball in the absence of the roller at the predefined operating conditions (entrainment speed and load), revealing the color and shape of the circular contact in its fully flooded state.

Step 4: A series of pictures of the dynamic ball-disc contact are taken with the camera.

Step 5: With the high-definition camera still in its original location, the roller, located in front of the test ball, is loaded and its dynamic contact is obtained. The roller, depending on its geometry (curvature radii) and normal load, will starve the ball-disc contact to a certain degree, which will be noticeable in the change of color of its area.

Step 6: Once the dynamic circular contact becomes stable, a series of pictures of the now starved contact are taken with the camera.

Step 7: The location of the camera is shifted to the region where the elliptical contact is found. The camera is rotated 45° to adjust to the new viewpoint of this contact.

Step 8: A series of pictures of the dynamic elliptical contact are taken with the camera.

Step 9: The camera is repositioned again to the region where the ball-disc contact is found and is rotated to its original orientation.

Step 10: A series of pictures of the dynamic circular contact are taken again in order to verify that no variations in the film thickness profile have taken place between the displacements of the camera.

Step 11: The amount of lubricant in front of the roller is adjusted. Starvation can be (a) increased by manually scrapping off lubricant from the surface of the disc with a small wiper or (b) reduced by adding more lubricant via a syringe onto the lower surface of the disc. Variations in the color in the circular contact should be noticeable at this moment.

Step 12: Steps 6 to 11 are repeated. The experiment is carried out until the circular contact (or the elliptical contact) displays a grey to black coloration; this is indicative that the measuring technique (i.e. white light interferometry) has reached its limit and the film thicknesses cannot be further measured past that color. Control over this parameter is lost and there is risk of damaging the disk or the rolling elements due to the lack of lubricant.

2.4.3. Selection of the roller

Not all rollers are appropriate for ensuring a uniform starvation throughout the entire contact region of the test ball. In general, the selection of a suitable roller is carried out by two criteria:

a) **Uniformity of the outlet.** In order to starve the ball-disc contact uniformly, the lubricant supply fed into it must be equally uniform. The quality of the lubricant supply, defined by a constant film thickness along the transversal direction of the flow, is dependent on the outlet of the elliptical contact generated by the roller. Ideally, this film thickness is constant in the case of a line contact. Therefore, the film thickness profile generated by the roller (elliptical in shape) should approximate the one of a line. The research conducted by Nijenbanning *et al.* [85] compares the central and minimum film thickness of elliptical contacts with different ellipticities against their corresponding equivalent line contact, estimated with their maximum Hertzian pressure and half-width (see Figure 2.11). The ellipticity of the contacts is described in terms of the ratio of reduced radii of curvature D. The study of Nijenbanning *et al.* [85] concludes that elements with a ratio D equal or below the value of 0.15 are expected to behave akin to a line contact carrying the same load and having the same width. Above said value, the deviation between real and approximated film thickness grows, especially in the case of the minimum film thickness. Under the latter circumstances, the outlet of the roller would be irregular, meaning different portions of the circular contact would be fed distinctively. As a result, the film thickness profile of the ball-disc contact would be defined by various degrees of starvation.

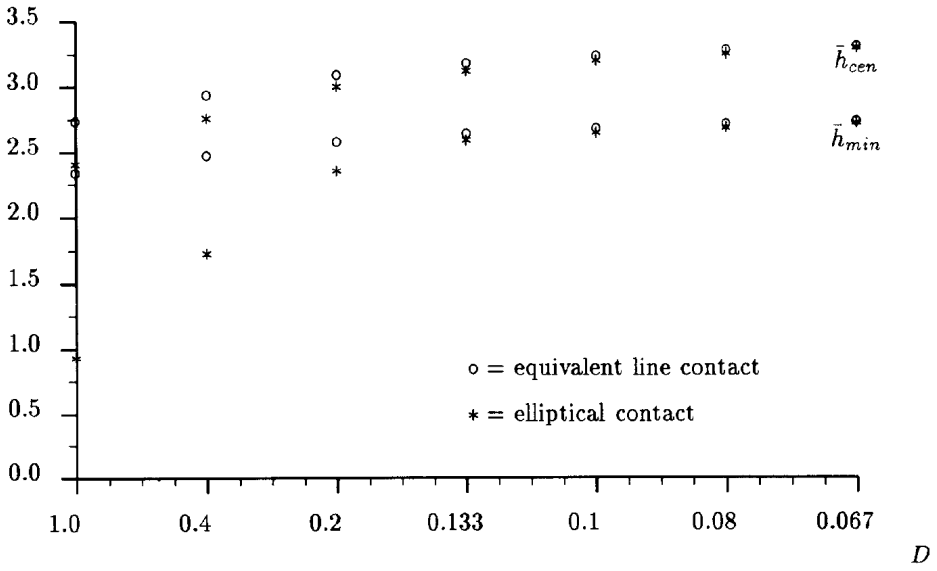

Figure 2.11. Variation of film thickness for different elliptical contacts with varying D ratio and their equivalent line contacts [85].

b) **<u>Contact size</u>.** The elliptical-contact geometry produced by the roller should be large enough, in the transverse direction to the main flow, to cover the entire contact area of the test ball (see Figure 2.12). This is expressed by the ratio between the half-widths of the elliptical contact $b_{elliptical}$ and the circular contact $a_{circular}$, both measured in the same transverse direction. This ratio is specified with the letter N ($N = b_{elliptical}/a_{circular}$).

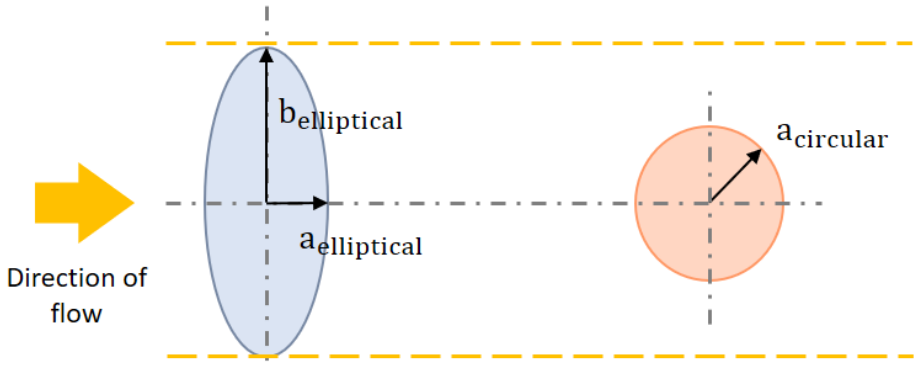

Figure 2.12. Size relationship between an elliptical and a circular contact.

When the ratio is below the value of 1, only the center region of the ball-disc contact will be starved (assuming it is perfectly aligned with respect to the center of the roller), while the side lobes will remain flooded. For $N \geq 2$ the entire circular contact will be starved equally if the criterion stated above applies. In addition, the greater the value of N, the easier it will be to positon the test ball with respect to the roller, as the outlet of the roller will have a larger racetrack width coverage. To illustrate this, Figure 2.13 shows the film thickness profiles of different elliptical contacts, along the transverse direction of the flow.

The profiles are plotted along a line that crosses the contact center. The D = 1 curve represents the size of the circular contact to be starved.

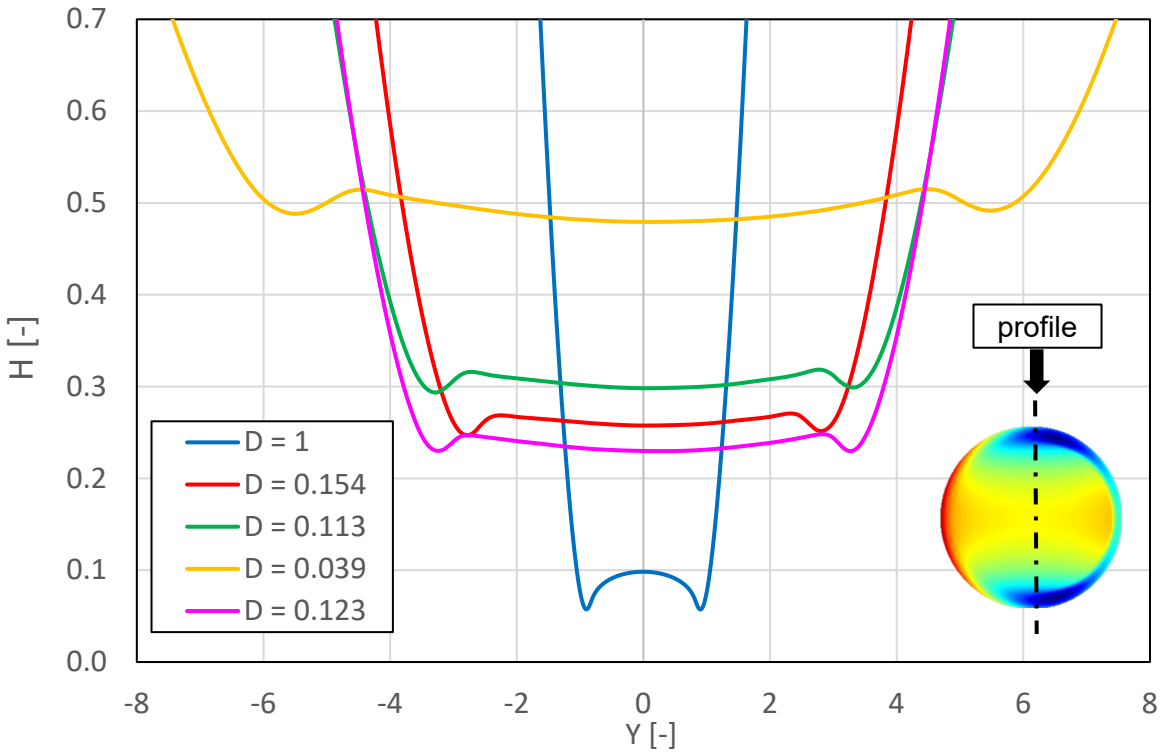

Figure 2.13. Dimensionless film thickness profiles in the transverse direction of the flow, for different elliptical contacts. The case D = 1 corresponds to the circular contact to be starved.

Regardless of the selection of a roller wide enough to starve the entire width of the ball-disc contact equally, the lubrication conditions of the latter highly depend on the geometry and the behavior of the air-oil meniscus found upstream of the roller-disc contact. Indeed, the shape of the meniscus resembles a parabola (e.g. Figure 2.2). This implies that the region of the roller-disc contact closer to the meniscus' peak will be more starved than the regions in the proximity of the peak. These conditions are then reflected at the outlet of the ellipse and create a layer of oil with variable film thickness that feeds into the test ball. Consequently, the ball-disc contact also presents an uneven starvation. The wider the ellipse, the wider the parabolic shape of the roller-disc inlet meniscus, which means that the differences in the degree of starvation are less pronounced.

The location of the roller's meniscus plays an important role too. Ideally, the position of this meniscus is centered at the centerline of the ellipse, following the direction of the main flow. However, this is not always the case. As highlighted in the experimental research from Maruyama and Saitoh [86], the position of the meniscus is greatly influenced by the centrifugal forces created during the rotation of the disc. Centrifugal forces would cause the meniscus to move sideways to the outer region of the racetrack. Because of it, the lubrication conditions of the roller-disc contact might change: the film thickness in the contact would decrease along the direction in which the displacement of the meniscus takes place. The same behavior is

hence reproduced in the ball-disc contact. One might then observe that the symmetry of the film thickness profile in the ball-disc contact is lost in a similar manner than with spinning (although with different mechanics involved). At the same time, Maruyama and Saitoh also remarked the effect of the lubricant's viscosity and the entrainment velocity on centrifugal forces. These are emphasized if low-viscosity lubricants or high entrainment speeds are in place. As a result of it, the lubricant reservoirs found sideways of the contact area lose their symmetry, with the one found at the outer side of the contact splitting from the main oil reservoir and moving away from the racetrack. As pointed out by Liang *et al.* [87] [88], the reflow of the lubricant back into the track is then diminished and the film thickness in this region is reduced asymmetrically.

Upon conducting experiments with the selected rollers, chosen based on the above criteria, two important limitations arise. These concern the range of film thickness measured. The following paragraphs describe these issues in more detail:

a) **Mild starvation.** Ideally, a whole range of degrees of starvation, from fully flooded down to fully starved, should be achieved by applying the roller and restricting its lubricant supply. However, it has been observed through tests carried out with Jerotrib that even complying with the above design criteria might result in an incomplete range of film thickness measurements, ranging from a flooded condition down to a given semi-starved one. Depending on the operating conditions of the test ball and the roller, this could account for up to 20% of the total measurable data. Indeed, how much a roller will be able to starve the test ball will depend on the film thickness value it will generate: the thicker the film thickness, the larger the scope. Assuming that the influence of the load on the film thickness generation is low with respect to that of the entrainment speed and that the latter is fixed by the movement of the disc, greater film thicknesses should be achieved by varying the ellipticity ratio of the roller, without compromising the previous statements. Given a fixed entrainment speed and load, rollers with a lower D ratio, i.e. producing wider elliptical contacts, satisfy this idea. Generally, under fully flooded and starved conditions, the roller should entrain a central film thickness greater or equal to that of the test ball, such that:

$$h_{c1} \geq h_{c2} \cdot \frac{\rho_{c2}}{\rho_{c1}} \tag{2.11}$$

where h_{ci} is the central film thickness of the contact and ρ_{ci} the density at the same location. Subscript i identifies the rolling element (1 for the roller and 2 for the test ball). This expression will be used in the next section to estimate the amount of lubricant upstream of the ball-disk contact.

b) **Severe starvation.** A similar limitation is observed on the opposite side of the measuring range. When applying white light interferometry with a disc equipped with a chromium layer, the minimum film thickness that can be measured is found to be around 50-70 nm, in the best cases. Below this value, the contact area displays a dark grey/black color, which renders the measuring technique as no longer viable. Depending on the operating conditions of the test ball, a comparable rate of up to 20% of the total measurable information is lost. This issue can be overcome by using a glass disc with a silica spacer layer. As seen in the experiments conducted in [64] and [63], this method would allow to

measure thinner film thickness profiles (down to a few nanometers) than with the classical approach.

2.4.4. Estimation of the lubricant supplied h_{oil}

In order to compare the experimental film thickness measurements to the results obtained through the computational model developed or other analytical models from the literature, such as the one from Chevalier *et al.* [44], one has to be able to accurately know the exact amount of oil supplied to the starved contact. This value is typically expressed in terms of an equivalent film thickness h_{oil}, which combines the amount of lubricant carried by the disc as well as the quantity that is replenished to the contact inlet from its outlet by the rolling element itself. However, the value of h_{oil} cannot be measured experimentally through conventional methods because the two oil quantities indicated above are found outside the contact region. For this reason, white light interferometry is no longer applicable in these locations. Other techniques, such as fluorescence [89], can be applied instead. Nevertheless, the resulting setup would not be compatible with the current arrangement of elements in the modified test rig proposed and would overcomplicate the existing experimental procedure (multiple measures for a single contact in a given lubrication state and numerous equipment changes required). Thus, one can take advantage of the oil distribution in the roller to estimate the amount of lubricant available at the inlet of the ball-disc contact. To do so, consider the diagram in Figure 2.14 illustrating a side view of the new experimental setup.

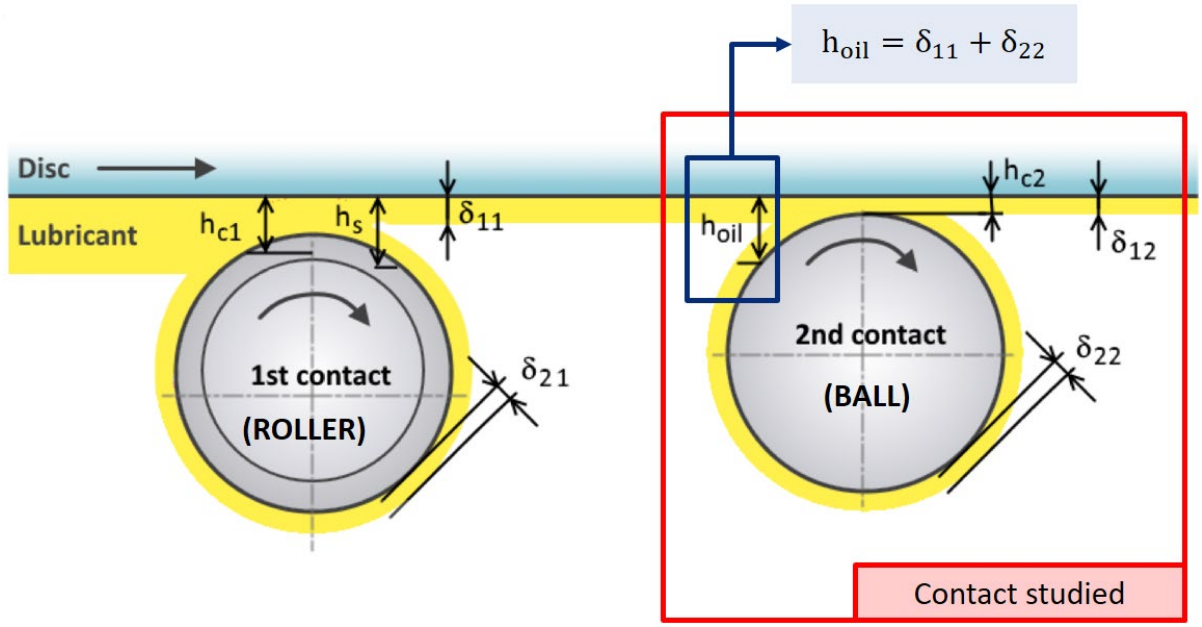

Figure 2.14. Schematic representation of the roller-ball-disc system (side view).

As explained above, the amount of lubricant supplied to the test ball can be defined as a uniform layer of lubricant of thickness h_{oil}. The flow conservation at the inlet region of the test ball in terms of film thickness is described as:

$$h_{oil} = \delta_{11} + \delta_{22} \tag{2.12}$$

where δ_{11} is the amount of lubricant carried by the disc from the outlet of the roller contact and δ_{22} the amount of lubricant replenished by the test ball from its outlet. At the same time, each oil quantity can be expressed as a function of the central film thickness of the rolling element responsible to carry said quantity.

$$\delta_{ii} = \Delta \cdot h_{ci} \cdot \frac{\rho_{ci}}{\rho_0} \tag{2.13}$$

with subscript i identifying the rolling element (1 being the roller and 2 the test ball). The compressibility effects of the lubricant have been taken into account by including the ratio between the density of the lubricant at the contact center ρ_c and that at ambient pressure ρ_0. Δ is the lubricant rupture ratio at a lubricated contact outlet defined by Bruyère *et al*. [90], which depends on the SRR:

$$\Delta = \frac{1}{2} + \frac{SRR \cdot \left(1 + \sqrt{1 - \left(\frac{SRR}{2}\right)^2}\right)}{-SRR^2 + 8 \cdot \left(1 + \sqrt{1 - \left(\frac{SRR}{2}\right)^2}\right)} \tag{2.14}$$

If one assumes that the velocity of the disc and the rolling elements is the same (i.e. SRR = 0 in each rolling element-disc contact), then the lubricant rupture ratio Δ is reduced to a value of 0.5. In the case of the roller, a small residual friction may exist as a result of the entrainment of the roller by the disc, but its influence on the contact's film thickness is minimal. On the other hand, pure rolling conditions are ensured for the ball-disk contact by controlling the velocity of the elements in contact through separate motors. Consequently, Eq. (2.12) can be rewritten as:

$$h_{oil} = 0.5 \cdot \left(h_{c1} \cdot \frac{\rho_{c1}}{\rho_0} + h_{c2} \cdot \frac{\rho_{c2}}{\rho_0}\right) \tag{2.15}$$

A similar, and perhaps more intuitive formula, could be obtained by considering the minimum central film thickness at each contact's outlet instead of the central film thickness. However, the advantage in choosing the latter parameter is evident when estimating the density of the lubricant at these locations (approximation to the Hertzian pressure value). Furthermore, most of the film thickness measures in starved contacts are written in a dimensionless form using the central film thickness. Therefore, the notation employed throughout the study remains consistent. On the other hand, his expression, as well as the experimental analysis carried out in future chapters, omits the fact that the lubricant exiting the track can reenter it again. Although elliptical contacts might offer a resistance to this phenomenon, the ball-disk contact might still be susceptible to it, especially when spinning kinematics are applied.

Taking into consideration the above assumptions, and for any lubrication condition, one can also express the central film thickness of the test ball h_{c2} as a function of the amount of lubricant h_{oil} found upstream of the ball-disk contact, so that:

$$h_{c2} \leq h_{oil} \cdot \frac{\rho_0}{\rho_{c2}} \tag{2.16}$$

When combining expressions (2.12), (2.13) and (2.16), and likewise considering a slide-to-roll ratio equal to zero in both contact regions, one would obtain the inequality in Eq. (2.11), presented in the previous section. This expression conditions the minimum central film thickness in the roller-disc contact to ensure that starved conditions are applied to the test ball-disc contact.

2.5. Conclusion

In this chapter, several experimental tools were presented, in particular, a new experimental set up to induce, control and measure starvation in EHD point contacts, which has been applied to two existing test rigs: Jerotrib and Tribogyr.

The new set up utilizes a roller to introduce a uniform and wide-enough film layer of lubricant into the test (specimen-disc) contact. Some challenges arise in the process, such as the control of the air-oil meniscus found upstream of the contact inlet or the capacity to measure an entire range of film thicknesses (from fully flooded to fully starved), derived from a variable lubricant supply. Finally, it was shown that it is able to estimate the amount of lubricant supplied to the test ball with fair accuracy by evaluating the film thickness in the contact generated by the roller.

III Numerical modelling of EHD contacts

The aim of this chapter is to introduce the set of differential equations and rheological laws necessary to describe the behavior of EHD starved contacts. The numerical model presented is conceived as an extension to the full system approach introduced in previous works. Concepts from the biphasic fluid theory are applied to tackle the starved problem from a physical approach, whereby the lubricant and air volumes in the gap region are treated as an equivalent fluid with unique properties. The numerical model is ultimately validated with experimental measurements and is compared to other predictive models from the literature. .

3.1. Fully flooded EHD contact model

The numerical model described in this section is based on the full-system approach conceived by Habchi *et al.* [91] [92] and later adapted to the specific operating conditions in the work of Doki-Thonon *et al.* [76] and Wheeler *et al.* [93] [77]. The model is built on the generalized Reynolds equation and implements a series of additional expressions to characterize the behavior of the contacting solids, the gap height as well as the fluid entrapped between their surfaces. Isothermal and Newtonian lubrication conditions have been taken into account and the surfaces in contact are assumed to be smooth.

3.1.1. The generalized Reynolds equation

The Reynolds equation [94] allows to describe the pressure distribution within a fluid film. It can be derived from the full Navier-Stokes equations. In order to do so, several assumptions have to be considered regarding the nature of the fluid and the gap region. For instance, the fluid has to represent a continuous medium, with its flow being viscous, laminar and independent of time. This implies that both inertia and surface tension forces can be neglected with respect to viscous forces. On the other hand, the height of the gap should be much smaller compared to the dimensions in the other two directions of the contact. The simplified Navier-Stokes equations then read:

$$\frac{\partial \mathrm{p}}{\partial \mathrm{x}} = \frac{\partial}{\partial \mathrm{z}}\left(\mu \frac{\partial \mathrm{u_{f,x}}}{\partial \mathrm{z}}\right) \tag{3.1a}$$

$$\frac{\partial \mathrm{p}}{\partial \mathrm{y}} = \frac{\partial}{\partial \mathrm{z}}\left(\mu \frac{\partial \mathrm{u_{f,y}}}{\partial \mathrm{z}}\right) \tag{3.1b}$$

$$\frac{\partial \mathrm{p}}{\partial \mathrm{z}} = 0 \tag{3.1c}$$

where p is the pressure, μ is the viscosity of the fluid and $u_{f,i}$ is the velocity field of the lubricant in the i-direction.

By taking into account no-slip boundary conditions at the contact interface and integrating along the z-direction, the velocity profile of the fluid is obtained. Its components in the x and y-direction, $u_{f,x}$ and $u_{f,y}$, respectively, are written:

$$u_{f,x} = \frac{1}{2\mu}\frac{\partial p}{\partial x} z(z-h) + u_{x,h}\frac{z}{h} + u_{x,0}\left(1-\frac{z}{h}\right) \tag{3.2a}$$

$$u_{f,y} = \frac{1}{2\mu}\frac{\partial p}{\partial x} z(z-h) + u_{y,h}\frac{z}{h} + u_{y,0}\left(1-\frac{z}{h}\right) \tag{3.2b}$$

with h the gap height and $u_{i,h}$ and $u_{i,0}$ the velocity components in the i-direction at the heights $z = h$ and $z = 0$, respectively. Because of the no-slip condition, these two velocities are identified with the velocities fields of the top ($\vec{u}_t$) and bottom ($\vec{u}_b$) surfaces.

By applying the mass conservation equation for a compressible flow under steady-state condition:

$$\frac{\partial}{\partial x}\int_0^h \rho u_{f,x} dz + \frac{\partial}{\partial y}\int_0^h \rho u_{f,y} dz = 0 \tag{3.3}$$

with ρ the density of the fluid, and introducing the velocity field of the fluid found in Equation (3.2), one finally arrives at the Reynolds equation:

$$\frac{\partial}{\partial x}\left(\frac{\rho h^3}{12\mu}\frac{\partial p}{\partial x}\right) + \frac{\partial}{\partial y}\left(\frac{\rho h^3}{12\mu}\frac{\partial p}{\partial y}\right) - \frac{\partial}{\partial x}\left(u_{m,x}\rho h\right) - \frac{\partial}{\partial y}\left(u_{m,y}\rho h\right) = 0 \tag{3.4}$$

where $u_{m,j}$ is the mean velocity of the solid in the j-direction. The first two terms of the expression are known as the Poiseuille term and describe the flow driven by the pressure gradient, whereas the third term, or Couette term, defines the flow generated by the entrainment of the fluid through the walls of the solids in contact.

The film thickness h considered in (3.4) is computed assuming an approximated parabolic shape of the undeformed solids at the contact vicinity.

$$h(x,y) = h_0 + \frac{x^2}{2R_x} + \frac{y^2}{2R_y} + \delta(x,y) \tag{3.5}$$

where h_0 is a constant describing the rigid body displacement at the contact center and $\delta(x,y)$ the elastic deformation of the surfaces along the z-direction. R_x and R_y are the equivalent radii of curvature in the x and y-directions of the mating solids, determined following the equivalent geometry formulation [95]. Using the equivalent body theory, the value of the equivalent Young modulus E' and the equivalent Poisson ratio υ can also be evaluated from the original bodies' properties:

$$E' = \frac{E_b^2 E_t (1+\upsilon_t)^2 + E_t^2 E_b (1+\upsilon_b)^2}{\left(E_b(1+\upsilon_t) + E_t(1+\upsilon_b)\right)^2} \tag{3.6a}$$

$$\upsilon = \frac{E_b \upsilon_t (1+\upsilon_t) + E_t \upsilon_b (1+\upsilon_b)}{E_b(1+\upsilon_t) + E_t(1+\upsilon_b)} \tag{3.6b}$$

with subscripts t and b indicating the properties of the top and bottom solid, respectively. An equivalent solid is hence modelled. The equivalent solid is assumed to have uniform and isentropic properties and to deform elastically due to the pressure generated by hydrodynamic effects. The elastic deformation endured by the solid is described by the linear elasticity equation:

$$\mathrm{div}(C\nabla u_f) = 0 \tag{3.7}$$

with C the fourth-order elasticity tensor.

Additionally, the load balance equation (3.8) applies, which allows to determine the value of h_0 in Equation (3.5). The imposed normal load w equals the integral of the lubricant pressure in the contact area S.

$$w = \iint_S p(x,y)\,dx\,dy \tag{3.8}$$

3.1.2. Lubricant rheology

In order to use the model presented here, the physical behavior of the fluid handled has to be described. Two oils were employed in this work, which have been denoted as lubricant 1 and 2. Lubricant 2 is a low viscosity mineral base turbine oil previously used in the thesis from Doki-Thonon [7] and Wheeler [1]. Lubricant 1 is a synthetic polyol ester-based oil that is one order of magnitude more viscous than the former oil at ambient conditions. It was selected to account for the various challenges expected to be encountered during the conduction of the experimental tasks (e.g. control of the air-oil meniscus and stable film thickness distribution over time). The rheological characterization of lubricant 1 and 2 are well known thanks to a series of extensive studies performed at LaMCoS involving the use of rheometers and viscometers. This has allowed to model and fit with fair accuracy the pressure and temperature dependence of the fluid's density and viscosity into specific analytical expressions. The experimental data available considers multiple temperature values ($0 \leq T \leq 150$ °C) and a wide range of pressures ($0.1 \leq p \leq 800$ MPa). The properties for lubricant 1 and 2 are highlighted in Tables 3.1 and 3.2.

Lubricant density

The pressure and temperature dependence of the density is defined by the Murnaghan equation of state [96]:

$$\frac{V}{V_0} = \frac{\rho_0}{\rho_f} = \left(1 + \frac{K_0'}{K_0} p\right)^{-\frac{1}{K_0'}} \tag{3.9}$$

where V and ρ_f are the volume and the density of the lubricant at a given pressure p and temperature T. V_0, ρ_0 and K_0 are the volume, the density and the bulk modulus measured at environmental conditions ($p = p_0 = 0$ and $T = T_0$), with K_0' a constant representing the dependence of K_0 to pressure values close to p_0. In turn, the bulk modulus can be written as a function of the temperature:

$$K_0 = K_{00} e^{-\beta_K T} \tag{3.10}$$

with K_{00} the value of K_0 when $T = 0\,K$ and β_K the bulk modulus-temperature coefficient. Considering a reference temperature T_R at an ambient pressure p_0, at which the lubricant is characterized, the density variation with respect to ρ_0 is expressed as:

$$\frac{V_0}{V_R} = \frac{\rho_R}{\rho_0} = 1 + a_v(T_0 - T_R) \tag{3.11}$$

with a_v the volume-temperature constant and V_R the volume corresponding to the reference temperature T_R. The values of parameters K_0, K_0', K_{00}, β_K and a_v are specific to each fluid.

Lubricant viscosity

The pressure and temperature dependence of the viscosity is modeled by a modified Williams-Landel-Ferry (WLF) correlation as described by Bair *et al.* in [97]. The viscosity law reads:

$$\mu(p, T) = \mu_G \exp\left(\frac{-2.303 C_1 (T - T_g) F}{C_2 + (T - T_g) F}\right) \tag{3.12}$$

where

$$T_g(p) = T_{g0} + A_1 \ln(1 + A_2 p) \tag{3.13a}$$

$$F(p) = (1 + b_1 p)^{b_2} \tag{3.13b}$$

A_1, A_2, b_1, b_2, C_1 and C_2 are constants of the WLF law, specific to the fluid considered. μ is the viscosity at pressure p and temperature T, while μ_G is the viscosity at the glass transition temperature T_g and a given pressure p. T_{g0} is the glass transition temperature at ambient pressure and F is the relative thermal expansion of the free volume, defined at a given pressure p.

Parameter [unit]	Lubricant 1	Lubricant 2
a_v [K^{-1}]	$8.88 \cdot 10^{-4}$	$7.33 \cdot 10^{-4}$
β_k [K^{-1}]	$6.60 \cdot 10^{-3}$	$6.09 \cdot 10^{-3}$
K_{00} [Pa]	$1.08 \cdot 10^{10}$	$9.23 \cdot 10^{9}$
K_0' [-]	10.22	10.55
T_R [K]	298	298
ρ_R [kg/m^3]	973	872

Table 3.1. Parameters of the Murnaghan EOS for lubricants 1 and 2.

Parameter [unit]	Lubricant 1	Lubricant 2
A_1 [°C]	61.00	188.86
A_2 [Pa^{-1}]	$1.04 \cdot 10^{-9}$	$0.72 \cdot 10^{-9}$
b_1 [Pa^{-1}]	$5.96 \cdot 10^{-9}$	$8.20 \cdot 10^{-9}$
b_2 [-]	-0.60	-0.53
C_1 [-]	16.00	16.09
C_2 [°C]	29.80	17.38
$T_{g,0}$ [°C]	-83.40	-83.21
μ_G [Pa·s]	$1 \cdot 10^{12}$	$1 \cdot 10^{12}$

Table 3.2. Parameters of the modified Yasutomi-WLF correlation for lubricants 1 and 2.

3.2. Starvation modelling

The following sections tackle the definition of a new strategy to model lubricant starvation. After a brief introduction on the approaches commonly employed in the literature, their formulation and the issues related to their use, some guidelines are given to describe the fluids in the gap region (i.e. air and oil) as an equivalent fluid, following the biphasic fluid theory. In addition, it will be explained how the properties of this equivalent fluid can be altered to consider different degrees of starvation at the contact inlet.

3.2.1 Classical approaches

The classical Reynolds equation described above does not take into consideration variations of the lubricant supply and its influence on the pressure generation. Contacts are so assumed to be fed by an infinite oil supply and hence operate under fully flooded conditions. However, this assumption does not always apply. Indeed, in a complete bearing, the lubrication conditions of a contact influences the oil supply of the subsequent contact; hence, it may operate under lubricant starvation. Gadallah and Dalmaz [31] proved that starvation could in fact become an essential mechanism governing the contact in specific mechanical systems; such is the case of the roller-end/flange contact. This may also be further enhanced by the operating conditions of the contact (e.g. high entrainment speeds [63]) or the use of a limited oil supply, associated to environmental friendly practices.

As indicated in previous chapters, the initial attempts to model starvation focused on the location of the inlet air-oil meniscus. Models like those defined by Wedeven *et al.* [32] [33] or Hamrock and Dowson [34] expressed the variation of the contact film thickness as a function of the meniscus position and a critical coordinate delimiting the transition between the fully flooded and starved regimes. Their solutions presented a similar form and were supported by experimental measurements. Similarly, Chiu [50] worked with a mathematical expression originally conceived by Kaptitza [98] to describe the evolution of the pressure profile with respect to the meniscus position, which satisfied the Reynolds equation. However, soon it was found that these models were limited under conditions of severe starvation. Under those circumstances, the meniscus tends to overlap with the Hertzian contact area and it becomes unable to be measured accurately.

An alternative criterion was then established around the amount of oil found upstream of the contact area and the definition of a fractional film content θ that altered the result of the Reynolds equation. This concept was first introduced by Jakobsson and Floberg [99] in the context of cavitation. They developed mass continuity conditions that would still apply on the meniscus. Olsson [100] extended these conditions to transient contacts. In 1974, Elrod and Adams [101] [102] set up the mathematical foundation to computationally model starved contacts in slider bearings. They distinguished between two distinctly lubricated subdomains (starved and full film) and ensured the mass conservation of the flow between them. The numerical formulation was later adopted and improved upon by Chevalier [103], who reported the first results for steady state circular EHD contacts [104] [44]. This scheme was used in the works from Wijnant [105] and Popovici [106]. The revised model from Chevalier [103] was extended in 2004 by Damiens *et al.* [45] to include the influence of the contact's ellipticity.

Classical formulation

In order to better understand the formulation developed by the latter classical models, Figure 3.1. schematically illustrates the contact region and its immediate environment and identifies the two subdomains considered above. Ω_1 represents the starved subdomain, occasionally wrongly referred to as cavitated, Ω_2 corresponds to the full film subdomain and $\delta\Omega$ is the boundary separating them.

In the starved subdomain Ω_1, the gap between the two solids is partially filled with lubricant. Separate layers of lubricant attach to each one of the mating surfaces and are kept apart from each other by a variable volume of air. The pressure throughout the subdomain is constant and equal to the ambient pressure. Inertia and surface tension forces are neglected. Thus, each lubricant film remains in a balance state and is entrained only by the movement of its corresponding surface, i.e. only the Couette component of the flow is concerned.

In the full film subdomain Ω_2, the gap is completely filled with lubricant, which is subjected to a positive pressure. In this region, the flow is governed by both Poiseuille and Couette components and satisfies the classical Reynolds equation in (3.4).

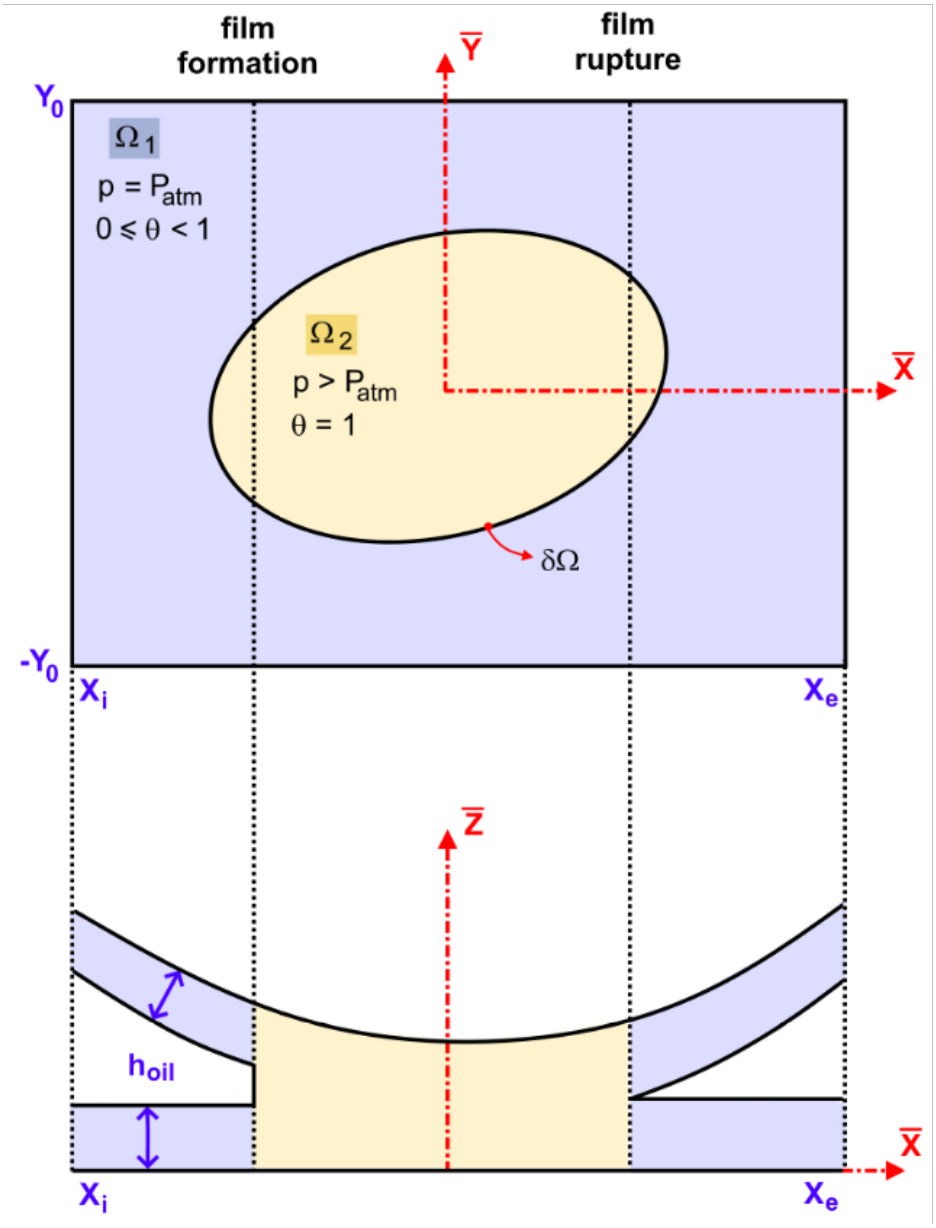

Figure 3.1. Schematic representation of the starved and full film subdomains (top view and cut view).

The location of the boundary $\delta\Omega$ is part of the solution of the starved problem, as it affects the pressure generation and film thickness build up in the contact region. Floberg [107] specified mass conserving and pressure continuity conditions along the free boundary. Therefore, at the film formation boundary:

$$\rho u_e \cos(\overrightarrow{e_x}, \vec{n})(1 - \theta^-) = \frac{\rho h^2}{12\eta}\frac{\partial p^+}{\partial n} \tag{3.14}$$

On the other hand, Reynolds (also known as Swift-Stieber [108] [109]) boundary conditions were included along mass conserving ones at the film rupture boundary:

$$\frac{\partial p^{-}}{\partial n} = 0 \tag{3.15a}$$

$$\theta^{+} = 1 \tag{3.15b}$$

Originally, Elrod and Adams envisioned θ as a means to reflect the compressibility effects of the fluid. Later, Chevalier [103] defined the same parameter as the local proportion of lubricant relative to the gap height, which represented a solution of the Reynolds equation alongside the pressure profile. The value of the fractional film content θ, as defined by Chevalier, was bound between 0 (dry contact) and 1 (fully flooded) and differed from the original model in that it could not exceed the value 1 inside the contact area.

The Reynolds equation can be rewritten to include the previous set of conditions. By doing so, the validity of the function is extended to the entire computation domain. The modified Reynolds equation then reads:

$$\frac{\partial}{\partial x}\left(\frac{\rho h^3}{12\mu}\frac{\partial p}{\partial x}\right) + \frac{\partial}{\partial y}\left(\frac{\rho h^3}{12\mu}\frac{\partial p}{\partial y}\right) - \frac{\partial(u_e \theta \rho h)}{\partial x} = 0 \tag{3.16}$$

with the complementary conditions:

$$(p - P_{cav})(\theta - 1) = 0 \tag{3.17a}$$

$$0 \leq \theta < 1 \tag{3.17b}$$

where P_{cav} is the cavitation pressure at the meniscus. This additional equation provides a unique solution to the lubrication problem. The oil supply of the contact, expressed as an equivalent film thickness h_{oil}, is defined as a boundary condition of the problem at the inlet boundary of the computation domain.

3.2.2 Development of a new approach for modelling starvation

Despite the widespread and successful adaptation of the Elrod-Adams algorithm to different industrial applications, the methodology lacks the physical foundation of a true biphasic approach. Indeed, the starved model derives from a local modification of the classical Reynolds equation, by which a fractional film content θ attenuates the effect of the Couette flow in thin films.

Bayada *et al.* [110] [111] extensively studied the formulation of the $\delta\Omega$ boundary problem and highlighted some aspects that could affect the quality of the computation and the results obtained from it, proving that the solution of the starved problem is not a trivial one. One of the issues evidenced was the fact that multiple pressure values would apply to a unique θ at the contact region. Furthermore, although the approach takes into account mass conservation at the boundary $\delta\Omega$, it was also observed that the evolution of θ and the pressure gradient at the full film domain boundary is discontinuous. Gu *et al.* [112] solved this point by defining a transition region at the interface of the two distinctly lubricated regions to smooth the jump; however, the mass conservation conditions would no longer apply. On the other hand, one can also note the formation of a subatmospheric depression area at the film rupture boundary, which can typically be neglected for high-pressure contacts such as those found in EHL. The

negative pressure values can be set to zero through the Reynolds boundary condition, together with the pressure gradient at the same interface. In the full-system computational model conceived by Habchi *et al.* [91] and introduced in the present chapter, this condition is included by means of a penalty term [113] in the Reynolds equation that equally complies with mass flow conservation and does not alter the positive pressure region. In practice, however, these subambient pressures are not fully removed from the results. Moreover, several authors have been able to observe and verify the existence of these cavitated regions experimentally [114] [115] [116].

As pointed out by Dowson and Taylor [114], the presence of cavitation at the contact outlet could affect the degree of starvation at its inlet region. Furthermore, if the cavitated area originated at the outlet is sufficiently large it could also affect the lubrication conditions of the subsequent element. Elrod and Adams [101] considered the integration of the Elrod algorithm for cavitation [102] into their model in the form of a θ-dependent switch function. However, by doing that the starved problem became highly nonlinear. Since then, multiple works have been dedicated to improve the convergence and stability issues derived from it; the reader may refer to the ones from Vijayaraghavan and Keith [117] and Fensanghary and Khonsari [118].

The coming subsections describe the formulation used to define how the lubricant and the equivalent fluid in the gap region behave for the range of pressures typically encountered in EHL, including subatmospheric pressure values. Following the biphasic fluid theory, the characterization of the gap density will ultimately serve to introduce starving conditions into the computation domain.

Lubricant pressure-density model

A common approach for modelling vaporous cavitation in lubricant films is through the description of the behavior of the lubricant at low pressure levels. The most significant of these models build on the idea of a homogeneous biphasic fluid with compressible character. One can highlight the models from Elrod [102], Shalin *et al.* [119], van Odyck and Venner [120], and Bayada and Chupin [121] [122]; a comparison between these models is performed in [121]. The different models mentioned agree in setting the densities of the vapor and the liquid phases to specific values, constant or variables according to a given density-pressure relation. However, they all differ on how the transition between the two phases is defined. Some models apply the step-like transition adopted in the Elrod algorithm [102] whereas others show a continuous density variation between phases, with this transition occurring between specific pressure values. Moreover, in the latter cases some discrepancies exist on the pressure value adopted at the cavitation boundary, with some references giving no indications on how to evaluate it. The compressible model from Bayada and Chupin [121] shows overall a good accordance with the cavitation models mentioned above and allows to describe the cavitation phenomenon from a physical perspective, which other approaches lack.

The lubricant is considered to be found in two distinct physical states: a pure liquid phase and a pure vapor phase, that exist below the wet point pressure $\mathrm{P_{vm}}$ and above the bubble point pressure $\mathrm{P_{sat}}$, respectively. Between these pressure values, a transition regime is identified in the form of a homogeneous mixture phase with fractions of lubricant in both vapor and liquid

phases. The model assumes an isentropic behavior of the lubricant, whereby no entropy is generated during phase changes of the fluid:

$$\frac{dp}{d\rho} = c_f^2 \tag{3.18}$$

with c_f the speed of sound in the fluid. Then, by integrating Equation (3.18) and applying the definition of the void fraction α (ratio of vapor volume over total volume) in each of the three phase regimes considered, the density-pressure law of the lubricant is calculated as a function of α:

$$\rho(\alpha) = \frac{p(\alpha)}{c_v^2} \quad \text{if } \alpha > 1 \tag{3.19a}$$

$$\rho(\alpha) = \left(\frac{\rho_l\left(\rho_v c_v^2(1-\alpha) + \rho_l c_l^2 \alpha\right)}{\rho_v c_v^2}\right) \exp\left(\frac{p(\alpha) - P_{sat}}{N}\right) \quad \text{if } 0 < \alpha < 1 \tag{3.19b}$$

$$\rho(\alpha) = \frac{p(\alpha) - P_{ml}}{c_l^2} + \rho_l \quad \text{if } \alpha < 0 \tag{3.19c}$$

where:

$$N = \frac{\rho_v c_v^2 \rho_l c_l^2 (\rho_v - \rho_l)}{\rho_v^2 c_v^2 - \rho_l^2 c_l^2} \tag{3.20}$$

The boundary pressures P_{vm} and P_{sat} are two of the integration constants determined by ensuring the continuity of the pressure in the lubricated domain:

$$P_{vm} = \rho_v c_v^2 \tag{3.21a}$$

$$P_{sat} = \rho_v c_v^2 - N \log\left(\frac{\rho_v^2 c_v^2}{\rho_l^2 c_l^2}\right) \tag{3.21b}$$

with ρ_v and ρ_l the density of the vapor and liquid phase at P_{vm} and P_{sat}, respectively, and c_v and c_l the speed of sound of the vapor and liquid phase. Although the liquid values c_l and ρ_l can be easily known, this is not the case of the vapor values c_v and ρ_v. Thus, one has to be careful with the selection of the adequate parameters as small variations in these may have an important effect on the bubble point pressure, as seen in Equation (3.21b). It is also important to note that pressures are expressed in absolute terms and not in relative ones, as most of the computational fully flooded models do.

The expressions in Equation (3.19) are adjusted to the present study's needs and are written in terms of the pressure instead of the void fraction α. Below the wet point pressure the density of the vapor phase is considered to be constant and equal to ρ_v. Above the bubble point pressure, the liquid fluid now complies with any density-pressure law, analytical or experimental, it best fits to; this includes the Murnaghan EOS introduced in this chapter. The density in this regime is noted as ρ_f. The mixture phase is described by a 3rd-degree polynomial function to guarantee that the transition between two successive phases is carried out in a smooth way (i.e., no abrupt change of slope). The coefficients of this function are calculated by ensuring the continuity of the density and its derivative with pressure at the wet

point and bubble point pressures. This second condition serves to trace a smooth transition between each phase.

$$\rho(p) = \rho_v \quad \text{if } p \le P_{vm} \tag{3.22a}$$
$$\rho(p) = A_r p^3 + B_r p^2 + C_r p + D_r \quad \text{if } P_{vm} < p < P_{sat} \tag{3.22b}$$
$$\rho(p) = \rho_f(p) \quad \text{if } p \ge P_{sat} \tag{3.22c}$$

with A_r, B_r, C_r and D_r the coefficients of the density function at the mixture regime, which are computed as:

$$A_r = \frac{2(\rho_l - \rho_v)}{(P_{vm} - P_{sat})^3} + \left.\frac{d\rho}{dp}\right|_{\rho=\rho_l} \cdot \frac{3}{(P_{vm} - P_{sat})^2} \tag{3.23a}$$
$$B_r = -1.5A_r(P_{sat} + P_{vm}) + \left.\frac{d\rho}{dp}\right|_{\rho=\rho_l} \cdot \frac{1}{(P_{sat} - P_{vm})} \tag{3.23b}$$
$$C_r = -3A_r P_{vm}^2 - 2B_r P_{vm} \tag{3.23c}$$
$$D_r = \rho_l - A_r P_{sat}^3 - B_r P_{sat}^2 - C_r P_{sat} \tag{3.23d}$$

Figure 3.2 illustrates the density variation with pressure of lubricant 2, following the behavior described in Equation (3.22). The density is expressed in its dimensionless form $\bar{\rho} = \rho/\rho_c$, with ρ_c the density at the contact center under fully flooded conditions.

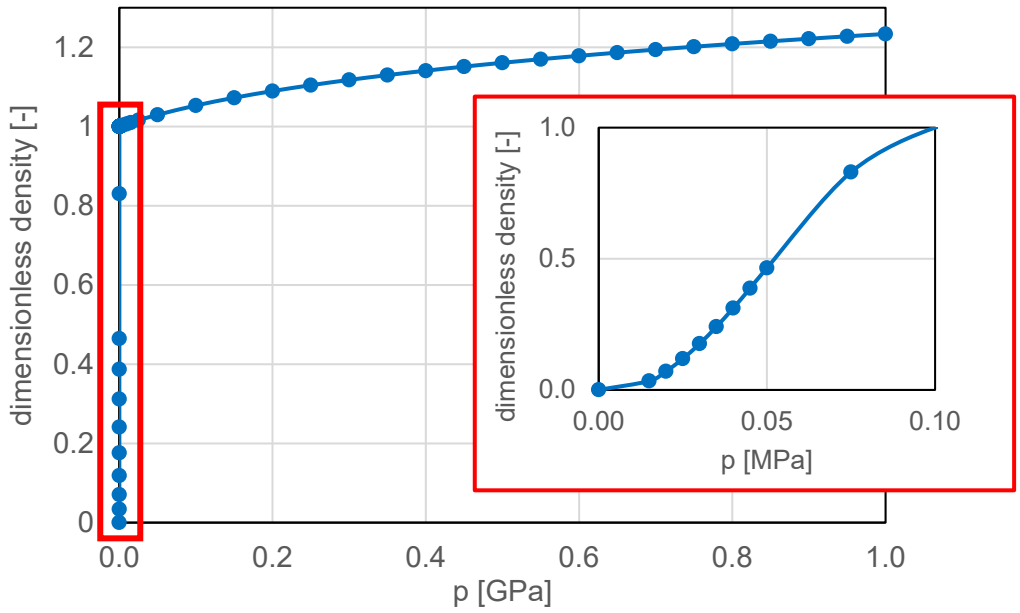

Figure 3.2. Dimensionless density $\bar{\rho}$ ($\bar{\rho} = \rho/\rho_c$) variation with pressure of lubricant 2. The zoomed area indicates the low-to-high pressure transition.

Lubricant pressure-viscosity model

According to the biphasic fluid theory, the behavior of the lubricant viscosity also varies with the physical state of the fluid. Similar to the pressure-density function detailed above, various analytical expressions describing the pressure-viscosity relationship between phases can be found in the literature (e.g., the McAdams [123] or the Kubota [124] models). Out of simplicity, the pressure-viscosity relation has been modelled replicating the structure of Equation (3.22). Thus, the viscosity in the mixture phase is described by a 3rd-degree polynomial function, with its coefficients calculated by ensuring the continuity of the function and its derivative with pressure at the wet point and bubble point pressures. Noting μ_v and μ_l the viscosity at the bubble point and wet point pressures, respectively, the full pressure-viscosity law reads:

$$\mu(p) = \mu_v \quad \text{if } p \leq P_{vm} \tag{3.24a}$$

$$\mu(p) = A_m p^3 + B_m p^2 + C_m p + D_m \quad \text{if } P_{vm} < p < P_{sat} \tag{3.24b}$$

$$\mu(p) = \mu_f(p) \quad \text{if } p \geq P_{sat} \tag{3.24c}$$

with A_m, B_m, C_m and D_m the coefficients of the viscosity function at the mixture regime, which are computed as:

$$A_m = \frac{2(\mu_l - \mu_v)}{(P_{vm} - P_{sat})^3} + \left.\frac{d\mu}{dp}\right|_{\mu=\mu_l} \cdot \frac{3}{(P_{vm} - P_{sat})^2} \tag{3.25a}$$

$$B_m = -1.5A_m(P_{sat} + P_{vm}) + \left.\frac{d\mu}{dp}\right|_{\mu=\mu_l} \cdot \frac{1}{(P_{sat} - P_{vm})} \tag{3.25b}$$

$$C_m = -3A_m P_{vm}^2 - 2B_m P_{vm} \tag{3.25c}$$

$$D_m = \rho_l - A_m P_{sat}^3 - B_m P_{sat}^2 - C_m P_{sat} \tag{3.25d}$$

The viscosity of the pure vapor state is assumed constant with pressure. The viscosity of the pure liquid state is denoted as $\mu_f(p)$ and follows, in the case of the present study, the modified WLF equation.

Gap pressure-density model

The gap density can be characterized following similar guidelines. To do so, the separate volumes of lubricant and air contained within the gap are identified as an equivalent and homogeneous compressible fluid, whose composition changes with pressure. P_{sat} defines the interface between the pure liquid and the mixture regimes of the gap and is so indicative of the location of the boundary $\delta\Omega$ (see Figure 3.1). Above the value of P_{sat}, the equivalent gap fluid is found only in its pure liquid phase, as it defines the contact region. The density in this domain follows the behavior of the preselected density-pressure law of the lubricant $\rho_f(p)$. Below the value of P_{vm}, the density of the equivalent fluid remains constant at a value of ρ_v. The transition between the densities ρ_v and ρ_l at the boundary pressures P_{vm} and P_{sat}, respectively, is no longer only dependent on the pressure field. For instance, if one takes into account Figure 3.1, the contact inlet has multiple gap densities associated to its ambient pressure. As the gap region closes into the contact area and the amount of lubricant found upstream of its inlet is considered constant, the volume of air in the region shrinks, thus increasing the density of the medium with its proximity to the contact. These conditions translate to:

$$\rho_g(p) = \rho_{g,v} \quad \text{if } p \leq P_{g,vm} \tag{3.26a}$$

$$\rho_g(p) = \rho_f(p)\frac{h_{oil}}{h(x,y)} + \rho_{g,v}\left(1 - \frac{h_{oil}}{h(x,y)}\right) \quad \text{if } P_{g,vm} < p < P_{g,sat} \tag{3.26b}$$

$$\rho_g(p) = \rho_f(p) \quad \text{if } p \geq P_{g,sat} \tag{3.26c}$$

with $h(x,y)$ the geometry of the gap and h_{oil} the equivalent film thickness layer of lubricant found upstream of the contact inlet. Subscript g refers to the gap.

Starvation mechanism

The lubrication conditions of the contact are defined by the value of the equivalent film thickness of lubricant h_{oil} specified at the boundary (X_i, Y). As indicated in Chapter II, this parameter combines the quantities of oil carried by the surfaces of the plane and the rotating element (see Figure 2.13), in terms of film thickness. Each lubrication condition (or degree of starvation) endured by the contact can be seen as the work of an equivalent fluid in the gap with a unique composition (lubricant to air relationship). Let χ be the composition of the equivalent fluid, representing its mass percentage of lubricant.

$$\chi(x,y) = \frac{h_{oil}}{h(x,y)} \tag{3.27}$$

with $h(x,y)$ the gap height at a given point (x,y). Similar to the fractional film content θ, the relation can be expressed as the ratio between the equivalent lubricant film thickness h_{oil} and the gap height h, its value being bound between 0 and 1. Under fully flooded conditions, the equivalent fluid in the gap is identified with the lubricant (χ = 1). Then, by diminishing the amount of oil (i.e. the value of h_{oil}), the original composition of the equivalent fluid in the gap changes ($0 \leq \chi < 1$).

The limit value of the composition of the equivalent fluid, χ_m, cannot be determined at the inlet boundary of the calculation domain (X_i, Y), as its value, dependent on h, would vary based on the inlet coordinate X_i chosen, given a constant oil supply h_{oil}. Furthermore, if χ is evaluated at a point far enough from the contact region, a reduction of h_{oil} (considering initial fully flooded conditions) might not entail variations in the degree of starvation of the contact, which might experience no change in its film thickness profile. Thus, the calculation of the lubricant mass content of the equivalent gap fluid is calculated at a reference point ($-X_m$,0), where X_m is the coordinate of the critical position of the air-oil meniscus, delimiting the behavior between fully flooded and starved conditions.

$$\chi_m = \frac{h_{oil}}{h(-X_m, 0)} \tag{3.28}$$

The value of X_m can be evaluated following the empirical expression from Hamrock and Dowson [34]:

$$X_m = 1 + 3.06\left(\left(\frac{R_x}{b}\right)^2 \frac{h_{c,ff}}{R_x}\right)^{0.58} \tag{3.29}$$

with b the contact radius in the transverse direction of the flow and $h_{c,ff}$ the film thickness at the geometrical center of the contact under fully flooded conditions.

The properties of the equivalent fluid in the gap are then determined. The velocity of the sound and the density in the pure vapor phase of the equivalent fluid, noted as $c_{g,v}$ and $\rho_{g,v}$, respectively, are calculated as a weighted average of the mass proportion of its components (oil and air) through χ_m.

$$c_{g,v} = c_{oil,v}\chi + c_{air,v}(1 - \chi_m) \quad (3.30a)$$

$$\rho_{g,v} = \rho_{oil,v}\chi + \rho_{air,v}(1 - \chi_m) \quad (3.30b)$$

As indicated previously in Equation (3.21), both parameters are employed in calculating the transition pressures P_{vm} and P_{sat}. When $\chi_m = 1$, both of these parameters will identify to those of the lubricant. The gap is thus filled with liquid lubricant and the contact operates under full film conditions. The values of P_{vm} and P_{sat} are so those encountered in the case of the lubricant. Conversely, if $\chi_m = 0$ the physical properties obtained will be those of the air and the contact is fully starved. Figure 3.3 shows the boundary pressure values as a function of the mass ratio χ_m for the case of lubricant 2.

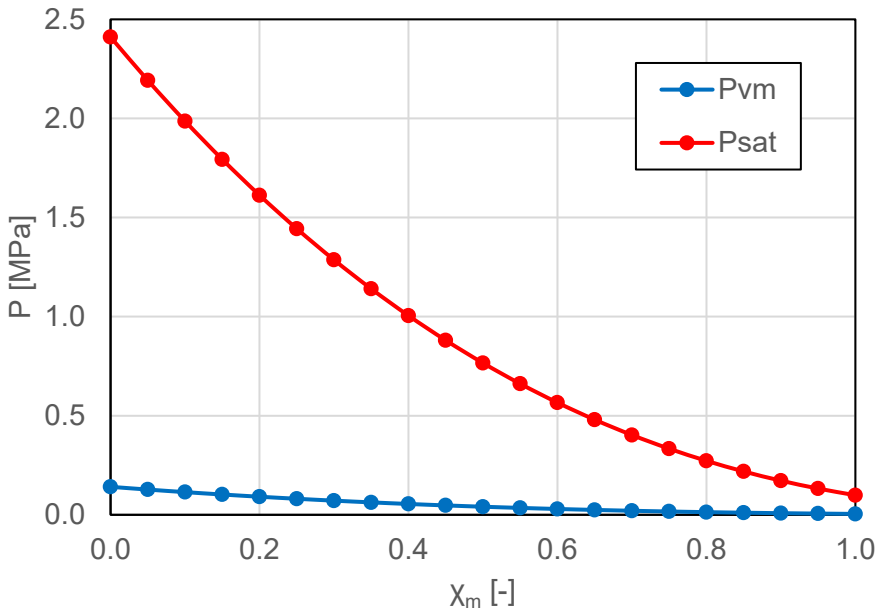

Figure 3.3. Variation of the wet point (P_{vm}) and bubble point (P_{sat}) pressures with the mass ratio χ_m for the case of lubricant 2.

By increasing the degree of starvation (i.e. reducing the lubricant mass proportion χ), the value of the bubble point pressure rises. Therefore, higher pressures will be required to build a fully lubricated film and the air-oil meniscus will be formed closer to the Hertzian contact area. The pressure and film thickness profiles of the contact will be affected. Figure 3.4 schematically illustrates how the gap density-pressure relation of lubricant 2 varies with the limit value of the lubricant mass ratio of the equivalent gap fluid. The density is expressed in its dimensionless

form $\bar{\rho} = \rho/\rho_c$, with ρ_c the density at the contact center under fully flooded conditions. It is relevant to note that the values in the x-axis only reveal a small fraction of the total range of pressures encountered inside the computation domain. With the rise of the degree of starvation, the difference between the wet point and bubble point pressures increases, expanding the mixture regime of the gap. As a result of it, the density from the vapor phase to the pure liquid phase changes at a much smoother pace.

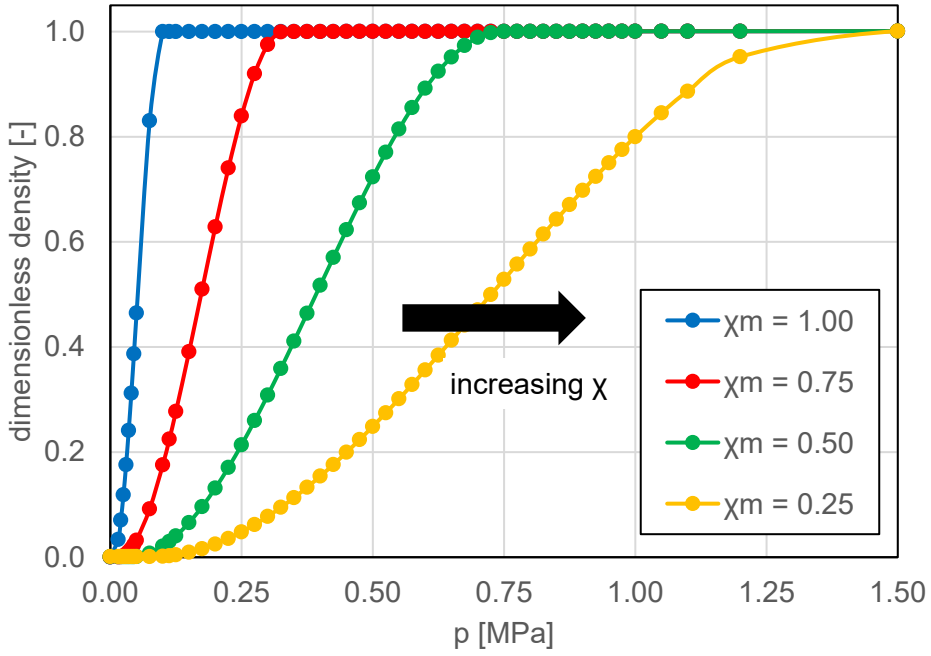

Figure 3.4. Gap density-pressure profiles considering lubricant 2 and various lubricant compositions χ_m (1, 0.75, 0.5 and 0.25). The density is expressed in its dimensionless form $\bar{\rho} = \rho/\rho_c$, with ρ_c the density at the contact center under fully flooded conditions. The arrow indicates the direction of decreasing lubricant mass proportion.

3.3. Numerical model

The set of equations introduced in the previous sections are solved on two distinct domains. These calculation domains are shown in Figure 3.5, together with the geometry of the numerical model.

The elastic deformations are solved on a cube representing the equivalent body of the contact system (grey area in Figure 3.5). Its dimensions are set to replicate a semi-infinite body, with a size 60a x 60b x 60a, a and b being the contact radii in the x and y-directions. These dimensions, much larger than those of the contact area, prevent any influence of the size of the elastic domain on the result from the Reynolds equation [4]. The lower surface of the cube is clamped, while the rest of the surfaces are left free. In the diagram in Figure 3.5, u, v and w are the elastic deformations of the solid in the x, y and z-directions, respectively. The pressure p generated by the contact applies on the upper surface of the equivalent solid. The

displacement $\delta(x,y)$ endured by the surface modifies the film thickness h in the Reynolds equation.

The Reynolds equation (with unknown p) is solved on a rectangular area (blue area in Figure 3.5) located on the upper surface of the equivalent solid. The Reynolds domain is much larger in size than the Hertzian contact area, marked in yellow color. Its dimensions are selected in such a way that they do not influence the results of the Reynolds equation. It is likewise adapted to the specific needs of the lubrication problem. In the present study, the size in the x-direction is set to $12a$ to account for the cavitation bubble size at the contact outlet and ensure the film thickness reformation at the edge of the computation domain. In the y-direction, the dimension is set to $6a$. In previous works, Habchi [4] set the size of the Reynolds domain to $6a$ in both directions (circular contacts with no spin), Doki-Thonon [7] specified it to $9a$ (circular contacts with severe spinning and skewing conditions) and Wheeler [1] chose $8a$ (elliptical contacts with milder spinning conditions). At the boundary of the Reynolds domain, the pressure is fixed at the ambient pressure value.

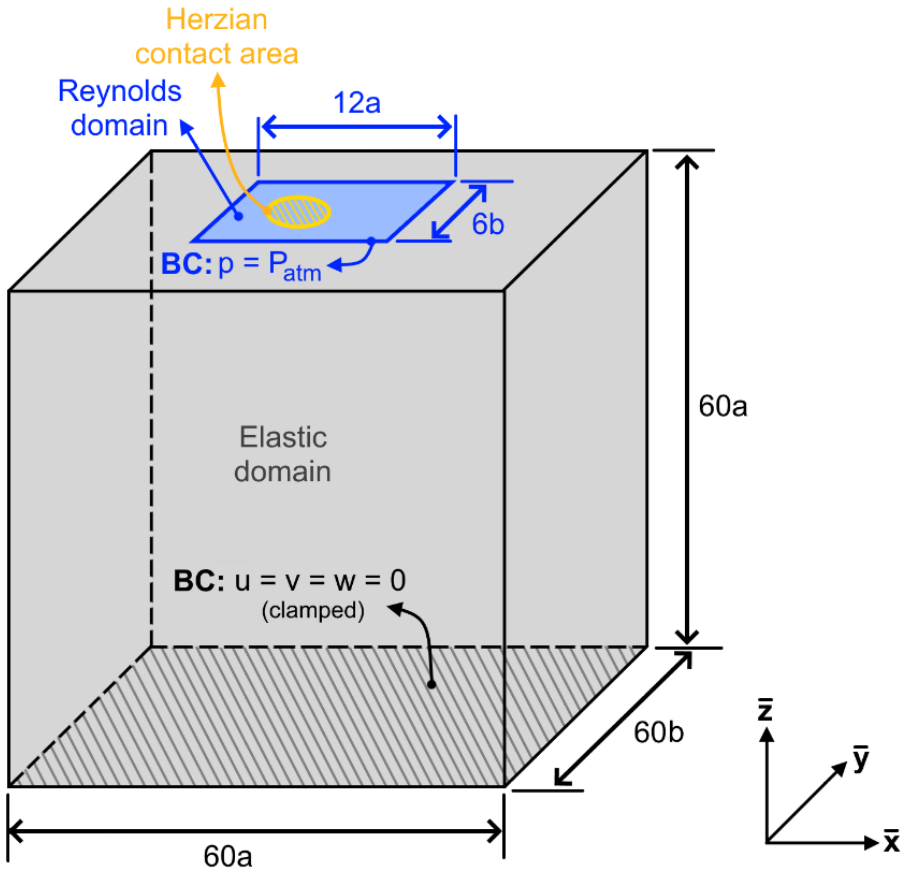

Figure 3.5. Computation domains of the numerical model.

The mesh size and distribution has been selected according to [4]. Special emphasis has been put into defining a fine mesh within the Hertzian contact area, where the pressure gradient is significant, in order to achieve a good accuracy. The mesh at the contact's inlet and outlet regions are left generally coarse. However, the size has been refined along the centerline of

the inlet along the main direction of the flow to better capture the variations in the position of the air-oil meniscus with starvation.

Numerical scheme

The set of equations are solved using a Finite Element full system approach, as developed by Habchi *et al.* in [91] [4]. Due to the complexity of the solution and the highly non-linear nature of the equations coupled, the computation of the problem is divided into successive steps tackling specific combinations of equations. In each step, initial conditions close to its final solution are given. Figure 3.6 illustrates the workflow of the numerical scheme.

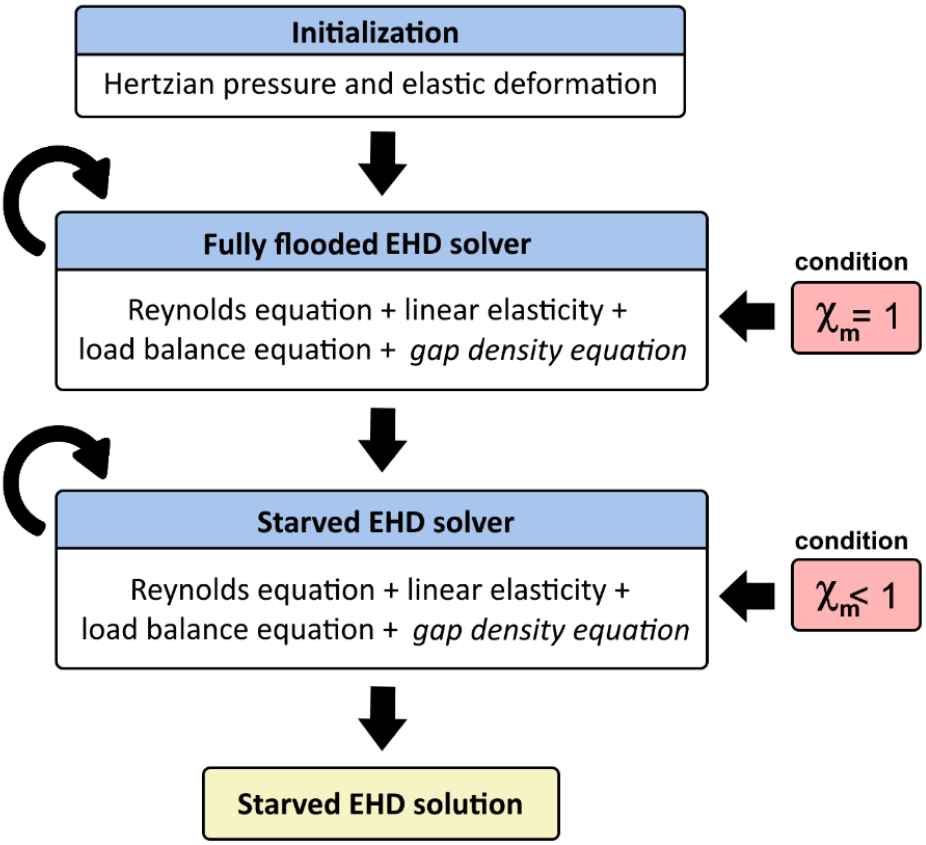

Figure 3.6. Workflow of the numerical scheme.

The procedure is initialized by a first step calculating the elastic deformation of the equivalent solid under a static Hertzian pressure. The solution of this step is then introduced as an input value to the next step: the initial elastic deformation for the linear elasticity equations and the Hertz pressure profile for the Reynolds equation. Both sets of equations are solved simultaneously together with the load balance equation, the rheology of the lubricant and the function defining the density of the equivalent fluid in the gap (Equation (3.26), which, in this case, corresponds to the behavior of the lubricant. The temperature is constant and the lubrication conditions are indicated as fully flooded by setting $\chi = 1$. Finally, the last step of the numerical scheme evaluates the EHD contact under starvation. In this case, the step considers

the value of h_{oil} introduced and determines the corresponding composition of the equivalent fluid in the gap (under starvation, $\chi \neq 1$). The same equations as those of the previous step are solved, with the behavior of the equivalent fluid in the gap being now different to that of the lubricant.

Each step is solved iteratively through a Newton-Raphson procedure until achieving the convergence of its local solution. The algorithm solves a total of 350500 degrees of freedom in the case of the fully flooded and starved steps and 120000 degrees of freedom during the initialization step.

3.4. Model validation

The validation of the present numerical model is made in terms of the film thickness profile of different contacts. It is carried out experimentally by means of the ball-on-disc tribometers Jerotrib and Tribogyr, introduced in the previous chapter, as well as film thickness predictions from analytical formulae found in the literature, concerning the central (h_c) and minimum (h_m) film thickness values. Although the previous versions of the model were already validated in past works for fully flooded conditions and a wide variety of contact configurations, because the present work alters the numerical scheme of the calculation, the validity of the fully flooded profiles is reevaluated.

Different conditions are thus examined. With Jerotrib, the film thickness profiles of non-spinning contacts are validated for oil supplies ranging from fully flooded to starved conditions. Tribogyr studies the same lubrication conditions on a much larger scale and in the presence of spin. For the fully flooded cases, only the test ball or the spherical-end specimen are used. In the case of starvation, a roller is placed in front of these elements and the oil supply in front of it is varied, as explained in Chapter II.

3.4.1. No-spin case

The following film thickness measurements have been obtained with Jerotrib by means of a transparent glass disk and a steel test ball. The results concern pure spinning kinematic conditions and no spinning and explore both fully flooded and starved lubrication conditions as well. As indicated in Chapter II, a roller is introduced to starve the ball-disk contact. The lubricant employed for these experiments is lubricant 1 (see Tables 3.1 and 3.2). The operating conditions of the test ball and the roller are summarized in Table 3.3. The normal load for both rolling elements is set to 30 N and their entrainment velocity is varied between 0.16 and 0.48 m/s, always under pure rolling conditions.

Parameter [Unit]	Test ball	Roller
u_e [m/s]	0.16 0.32 0.48	0.16 0.32 0.48
w [N]	30	30
R_x [mm]	12.7	10
R_y [mm]	12.7	81.4
p_H [GPa]	0.52	0.34
T [°C]	25	25
μ_0 [mPas]	148.0	148.0
α^* [GPa^{-1}]	21.2	21.2

Table 3.3. Operating conditions of the test ball and the roller.

Fully flooded conditions

The film thickness profiles obtained under fully flooded conditions are first examined. Figure 3.7 shows the experimental film thickness profiles along the y-axis for the three entrainment velocities specified above. They are compared to the corresponding film thickness profiles estimated with the present numerical model. Experimentally, a more than enough quantity of lubricant was applied to flood the test ball and no roller was employed to limit its oil supply. For each condition, a series of 5 interferograms were recorded and the average film thickness profiles were calculated. For illustration purposes, one of the interferograms registered for the u_e = 0.48 m/s case is shown, along with the coordinate system employed. A yellow arrow indicates the direction of the entrainment velocity. The Hertzian contact area is marked by a dotted circle.

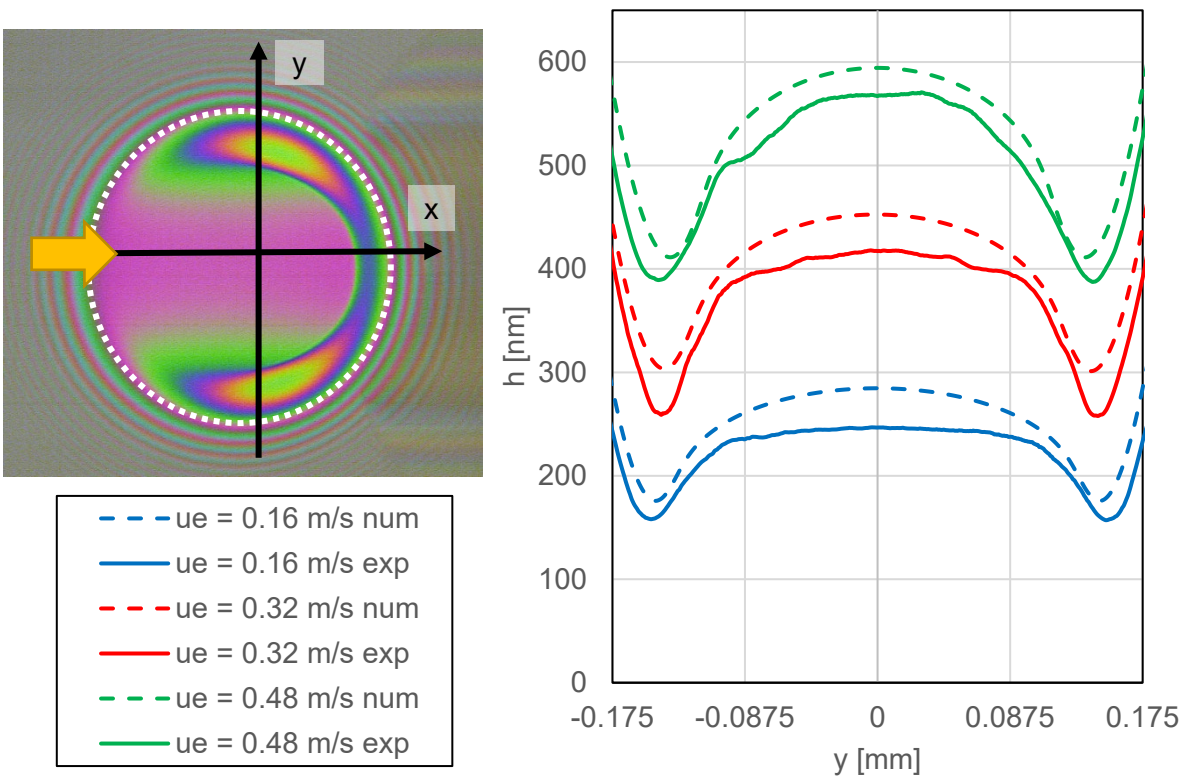

Figure 3.7. Film thickness along the y-axis for three entrainment speeds (0.16, 0.32 and 0.48 m/s). The interferogram (left) corresponds to the u_e = 0.48 m/s case. The direction of the entrainment velocity is represented by a yellow arrow. The Hertzian contact area is marked by a dotted circle.

The results were also compared to the numerical values for the same conditions from the model developed by Wheeler [1]. Said model constitutes the main base for the present numerical procedure and should compute similar results for fully flooded conditions, as the modifications implemented are meant to only affect the system when starved lubrication conditions are chosen. The model from Wheeler was verified experimentally and numerically for various ellipticital-shaped contacts and operating conditions. Table 3.4 gathers the central and minimum film thickness values determined with each of the three methods stated in this subsection.

u_e [m/s]	Current model		Wheeler model		Experimental	
	h_c [nm]	h_m [nm]	h_c [nm]	h_m [nm]	h_c [nm]	h_m [nm]
0.16	284	152	284	152	247	106
0.32	453	268	453	267	415	209
0.48	594	370	592	368	554	302

Table 3.4. Central and minimum film thicknesses under fully flooded conditions, obtained through different methods (current model, Wheeler model and experimental).

The results show overall a good correspondence between them. The comparison between the numerical and experimental values reveal an average relative deviation below 11% for h_c and 31% for h_m. The numerical model overpredicts the film thickness profiles, especially the minimum film thickness. However, when comparing the measures extracted from both numerical models, it can be noticed that the relative average difference lies, as expected, below 1% for the two film thicknesses considered. Whereas Wheeler employed a total length of 6 units along the direction of the flow, the current model applies a length of 14 units to account for the effects of cavitation at the contact outlet. One of the reasons behind the differences found between the numerical and experimental results could be traced back to the characterization of the lubricant viscosity. Although the WLF law was made to fit to the best possible extent the experimental viscosity values available, other models might be suggested to better approximate the pressure and temperature dependence, in particular, for the low pressure values.

Another aspect that has to be considered is the shape of the profiles along the y-axis. Figure 3.7 shows that the experimental profiles are much wider that their numerical counterpart and possess a flatter central region, which could also add to the higher differences in h_c.

Starved conditions

The previous three fully flooded contacts are now assessed with a variable lubricant supply. Experimentally, a roller is put in place to constraint the amount of oil fed into the contact, as depicted in Chapter II. A set of 5 interferograms for both the roller and the test ball are taken for each starved condition, in this case, to ensure that the lubrication conditions are stable in time. For each set of interferograms, the average central and minimum film thickness of the ball and the central film thickness of the roller are evaluated. The lubricant supply, expressed as of an equivalent film thickness h_{oil}, is estimated from the previous data as per Equation (2.15). Figure 3.8 shows the mean experimental film thickness profiles along the y-axis for a selected group of starved contacts for the operating conditions listed in Table 3.3 and the specific entrainment speed of 0.16 m/s. They are compared to corresponding numerical film thickness profiles obtained with the present numerical model. The y-coordinate is represented in the dimensionless form $Y = y/a$, where a is the contact radius. Likewise, the film thickness is shown in the dimensionless form $R = h/h_{c,ff}$, with $h_{c,ff}$ the central film thickness under fully flooded conditions. This allows to quantify the film thickness reduction due to starvation. The lubricant supply is also indicated in the dimensionless form $r_c = h_{oil}/h_{c,ff} \cdot \bar{\rho}_c$, where $\bar{\rho}_c = \rho_c/\rho_0$ is the dimensionless density at the contact's geometrical center. An interferogram of the corresponding r_c = 0.73 contact is shown in Figure 3.8, along with the coordinate system employed. A yellow arrow indicates the direction of the entrainment velocity. The Hertzian contact area is marked by a dotted circle. In the graph, a grey arrow indicates the direction of increasing degree of starvation.

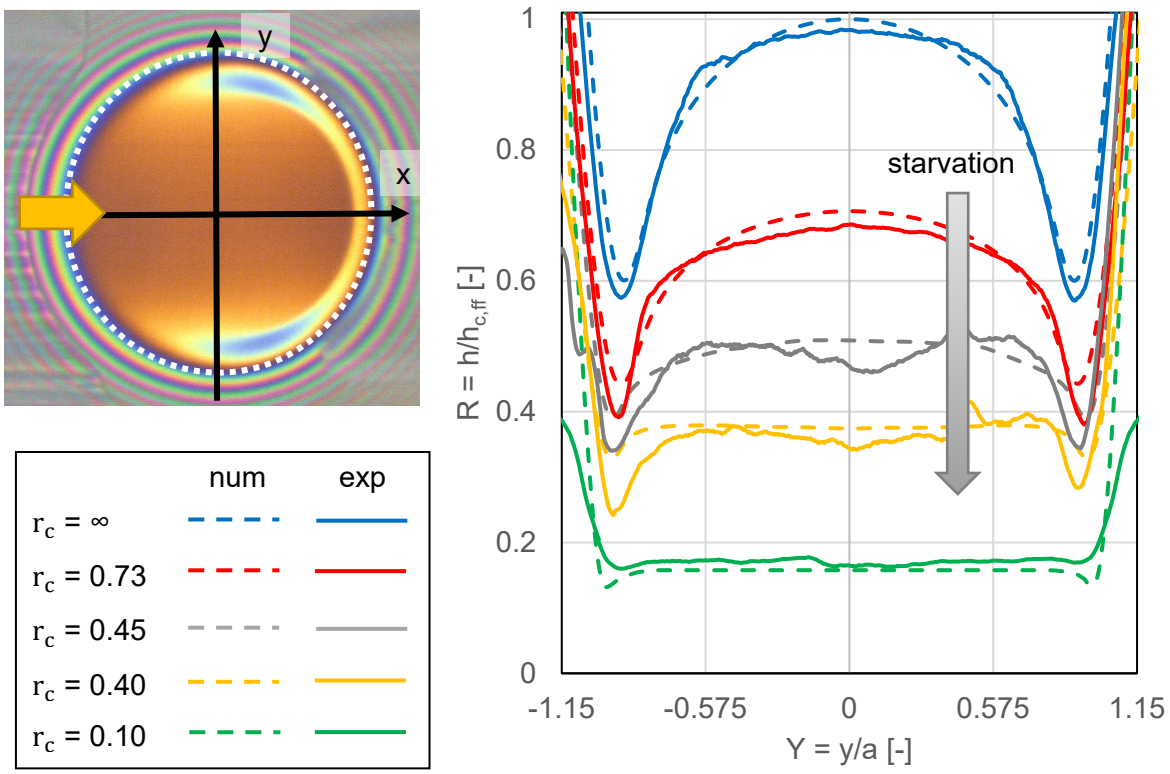

Figure 3.8. Film thickness along the y-axis for u_e = 0.16 m/s and multiple lubricant supplies r_c. The direction of the entrainment velocity is represented by a yellow arrow, while a grey arrow indicates the direction of increasing degree of starvation. The interferogram (left) corresponds to the r_c = 0.73 case. The Hertzian contact area is marked by a dotted circle.

The numerical and experimental results show qualitatively a good accordance. In this case, the average relative error for h_c is 5% and for h_m 17%. Likewise, deviations of the results reveal to be more significant at the side lobes than at the center region of the profile, which could be related, similar to the fully flooded cases discussed above, to the characterization of the lubricant viscosity for the low pressure values. Another source of error might come from how the oil distribution at the inlet region of the test ball is modelled. This modelling issue is discussed by Chevalier *et al.* in [104]. Indeed, the numerical model presented here defines a uniform oil supply at the contact inlet. The introduction of a roller in the test rig aims to replicate the conditions of the oil supply in the numerical model. At the same time, the oil distribution at the outlet of the roller-disc contact is dependent on the lubrication conditions at its inlet. In this case, the experimental observations reveal that the shape of the air-oil meniscus is not a straight line perpendicular to the main direction of the flow, but approximates a parabolic shape. These conditions are transmitted to the ball-disc contact and entail differences in the lubrication conditions within its contact region: the contact center and its side lobes will have different oil supplies, with the contact center achieving starved conditions sooner. Therefore, the lubrication conditions simulated might only be representative of a small portion of the entire contact area. A representation of this phenomenon is illustrated in Figure 3.9, which shows the interferograms of the ball-disk and roller-disk contacts. The shape of the inlet meniscus of the roller-disk contact is indicated by a red dashed line. It can be observed by the color that the

sidebands of the ball-disk contact are less starved than the central region of the contact; this might change with the degree of starvation.

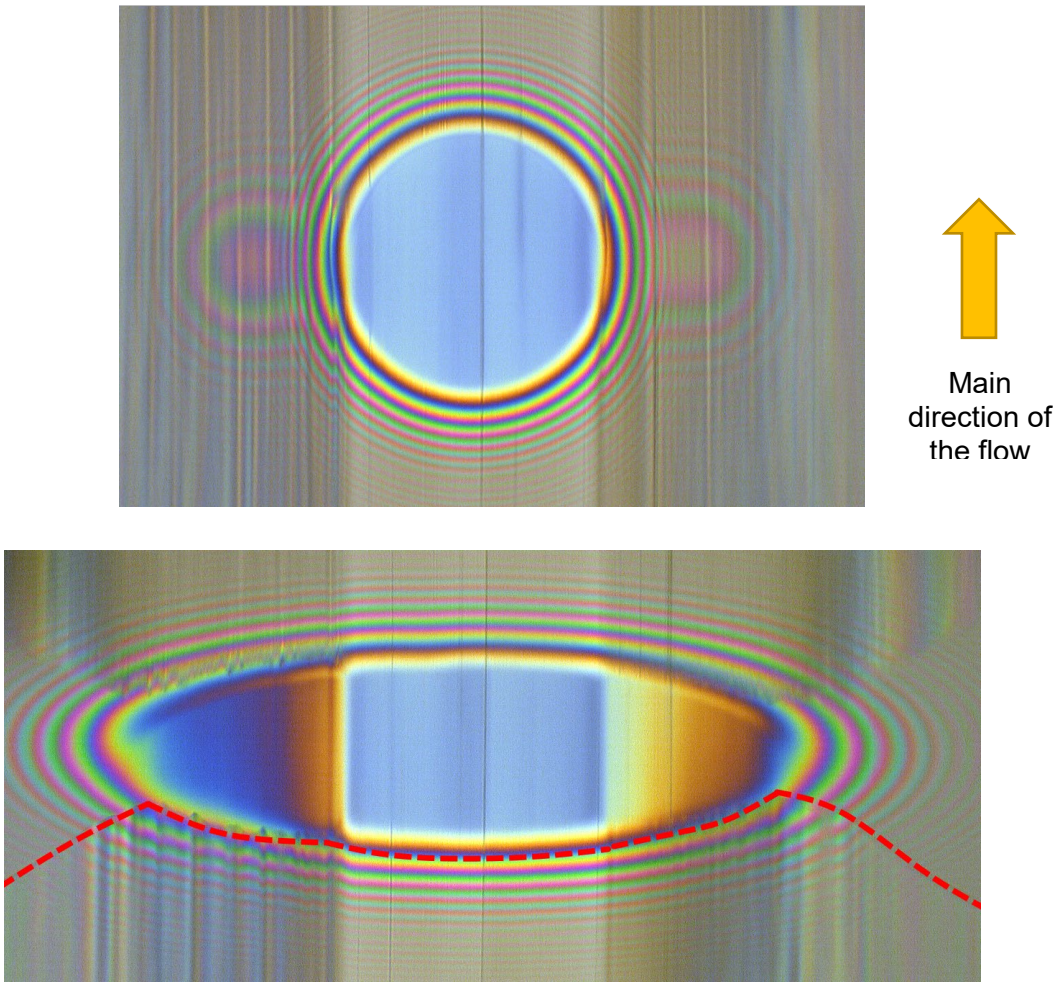

Figure 3.9. Ball-disk contact (up) and roller-disk contact (down) for u_e = 0.16 m/s, w = 30 N and r_c = 0.10. The shape of the inlet meniscus of the roller-disk contact is marked in red.

Figure 3.10 compares the central and minimum film thickness determined from (a) several prediction models from the literature (i.e. Chevalier [103], Wedeven [32] and Hamrock and Dowson [34]), (b) the present numerical model and (c) experimental measures from Jerotrib. These are referred in Figure 3.9 with the subscripts "$_{Chev}$", "$_{Wed}$", "$_{HD}$", "$_{Sim}$" and "$_{exp}$", respectively. The operating conditions are those listed in Table 3.3 and the entrainment speed on the test ball and the roller is 0.16 m/s. A grey arrow indicates the direction of increasing degrees of starvation.

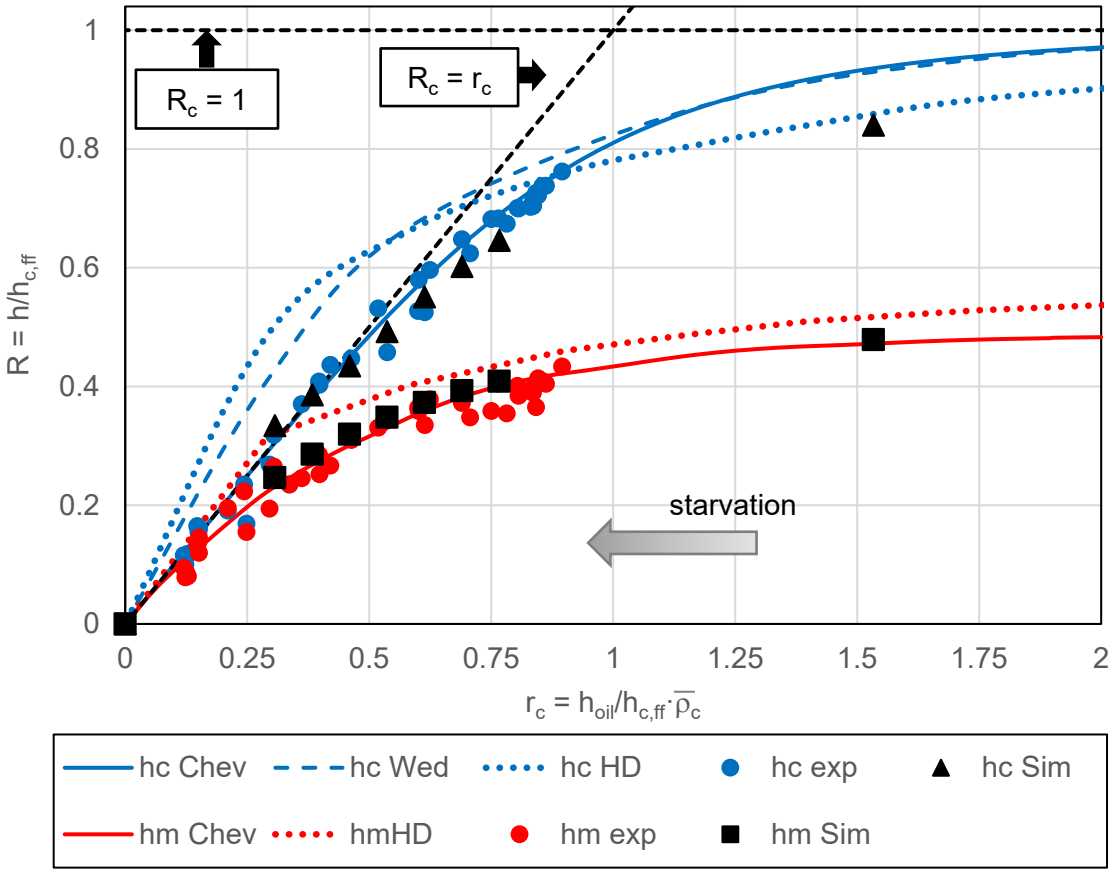

Figure 3.10. Variation of the central (h_c) and minimum (h_m) film thickness with the oil supply r_c (u_e = 0.16 m/s and w = 30 N), according to the present model ("$_{Sim}$"), experiments with Jerotrib ("$_{exp}$"), Chevalier ("$_{Chev}$") [103], Wedeven ("$_{Wed}$") [32] and Hamrock and Dowson ("$_{HD}$") [34].

The graph in Figure 3.10 plots the central and minimum film thickness of the contact against the equivalent film thickness of the oil supply h_{oil} it is subjected to. All parameters are expressed in their dimensionless form R and r_c using the central film thickness of the fully flooded contact as well as by taking into consideration the compressibility effects of the lubricant. Likewise, two asymptotes are traced: one for the condition $R = 1$ (the contact is fully flooded) and $R = r_c$, imposing a limit to the film thickness in the contact relative to the local oil supply. Any deviation of the curves or the individual points themselves along any of the axes might derive from the precision of the fully flooded h_c value, here used explicitly in the dimensioning of the data. In addition, one might also examine the validity of the predictive models from the literature. Chevalier *et al.* [44] argued that the Hamrock and Dowson model was not reliable for highly starved systems, as the value h_c tended to be higher than h_{oil} and so physically unrealistic. The model from Wedeven, although more accurate than the former one in the mildly starved domain, is constructed on similar criteria. Like the Hamrock and Dowson model, it establishes a critical position of the lubrication boundary to determine whether the contact is starved or not. One can observe in Figure 3.10 that the accuracy is also lost to a certain degree for the highly starved measures, which is understandable given the

difficulty for evaluating the exact position of the air-oil meniscus in those conditions experimentally.

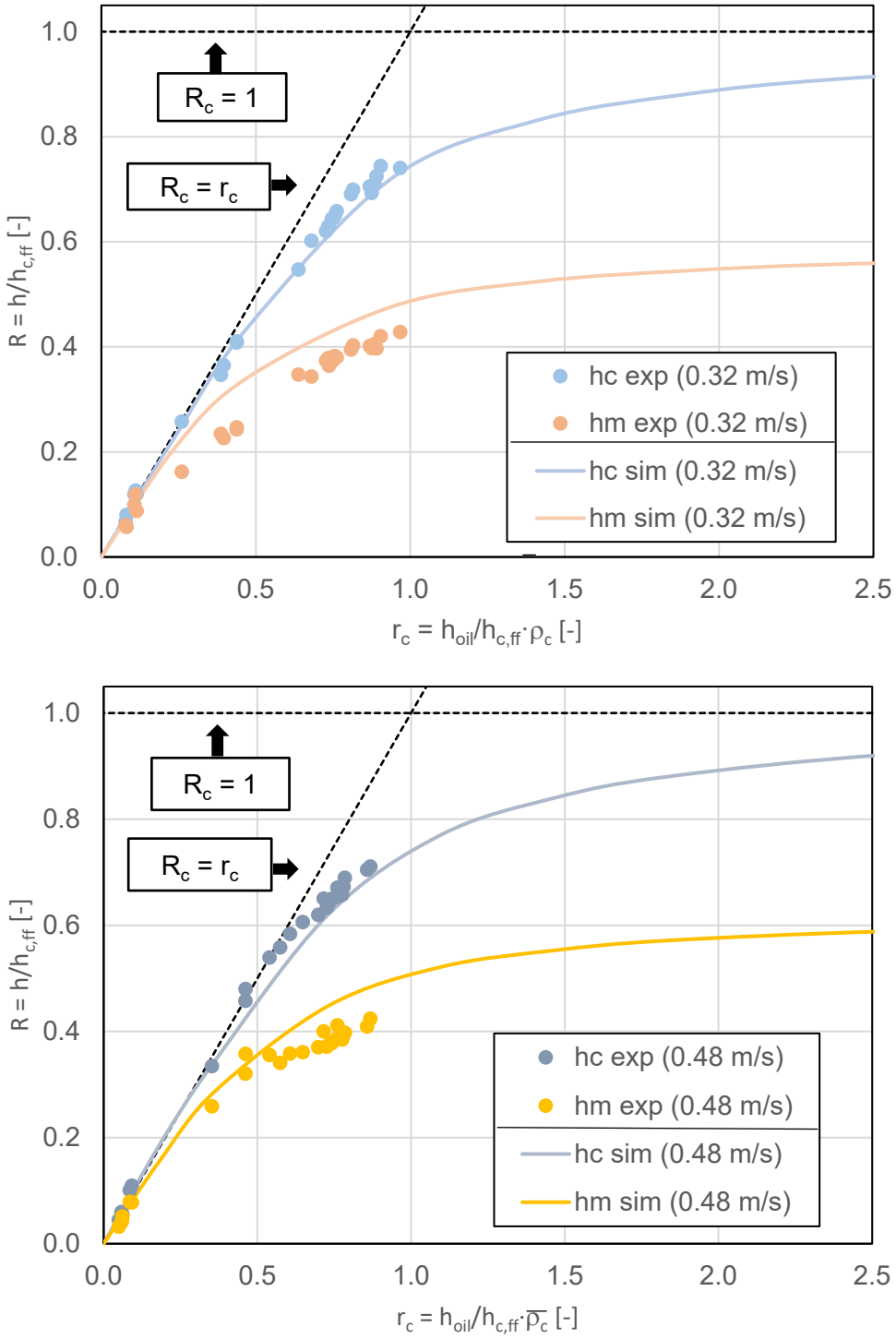

Figure 3.11. Variation of the central (h_c) and minimum (h_m) film thickness with the oil supply r_c (u_e = 0.32 and 0.48 m/s and w = 30 N), according to the present model ("$_{Sim}$") and experiments with Jerotrib ("$_{exp}$").

The validation of the computational model is completed by testing two additional entrainment speeds, specifically, u_e = 0.32 and 0.48 m/s. Figure 3.11 shows the R-r_c plots for the new operating conditions. The graphs display the results extracted from the present computational model (subscript "$_{Sim}$") and the experimental measurements obtained through Jerotrib (subscript "$_{exp}$"). In these cases, predictions from the previously mentioned models from the literature are omitted.

The numerical and experimental approaches reveal to be in good accordance for the two operating conditions shown. Quantitatively, some differences arise for the minimum film values in spite of the similar trends. For the operating conditions illustrated in Figure 3.10, and despite the efforts put into experimentally starving the ball-disc contact in a uniform manner, it becomes difficult to ensure a regular oil supply along the contact width with relatively high entrainment velocities. Indeed, the air-oil meniscus in front of the roller-disc contact gets easily affected by centrifugal effects, especially with high velocities or low lubricant viscosities. Thus, the meniscus is displaced sideways, distancing itself from the disc's center. As a result of it, the local minima found in this region will generally be more starved than the local minima at the opposite side lobe, closer to the disc's center. The variation in the position of the oil supply entrains so a loss of symmetry in the ball-disc contact's film thickness profile similar to the one observed under spinning conditions, although through a different mechanism.

3.4.2. Spin case

The set of results presented in this section serve to validate the numerical model when both spinning kinematics and starvation are combined. The experimental film thickness measurements have been obtained with Tribogyr. The new operating conditions of the contacts are summarized in Table 3.5. Lubricant 1 is still employed. The dimensions of the spherical-end specimen are greater than those of the previous test ball (R_x = R_y = 50 mm). Moreover, a roller with a new geometry is used to adapt to the new operating conditions of the ball-disk contact. The entrainment velocity of the system is 0.50 m/s and the normal load applied by the specimen is 400 N. A spinning angle λ = 9° is introduced. The spin rotational velocity of the specimen ω is 62.3 rad/s.

Parameter [Unit]	Specimen	Roller
u_e [m/s]	0.50	0.50
w [N]	400	250
R_x [mm]	50	11
R_y [mm]	50	269
p_H [GPa]	0.50	0.50
T [°C]	30	30
μ_0 [mPas]	148.0	148.0
α^* [GPa^{-1}]	21.2	21.2
λ [°]	9	n/a
ω [rad/s]	62.3	n/a

Table 3.5. Operating conditions of spherical-end specimen and the roller.

Figure 3.12 shows the experimental and numerical fully flooded film thickness profiles along the y-axis for the previously stated operating conditions, as well as a selection of film thickness profiles for some of the starved cases induced under the same conditions. The experimental procedure followed is similar to that applied with Jerotrib. In Figure 3.12, an interferogram of the fully flooded contact is depicted together with the coordinate system used and an arrow illustrating the direction of the entrainment velocity. The Hertzian contact area is marked by a dotted circle. In the graph, a grey arrow indicates the direction of increasing degree of starvation.

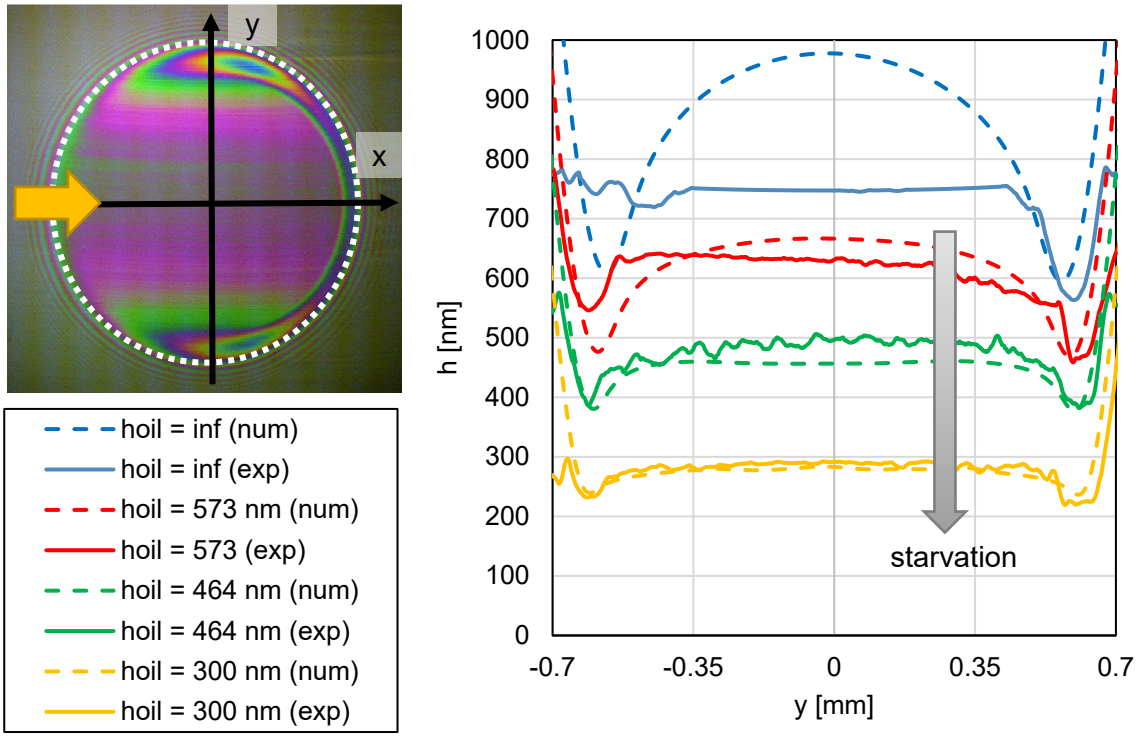

Figure 3.12. Film thickness along the y-axis for u_e = 0.50 m/s and w = 400 N. The direction of the entrainment velocity is represented by a yellow arrow. The interferogram (left) corresponds to the fully flooded case. The Hertzian contact area is marked by a dotted circle.

The numerical and experimental results show a good agreement between them. The high spin angle λ induces a very weak dissymmetry in the profiles, which can be observed in both set of curves. However, some significant discrepancies arise regarding the shape of the fully flooded profile. For this condition, the central region of the profile shows a flatter shape, thus inducing an important variation in the prediction of h_c with respect to the numerical solution. This deviation might be the result of the limitation of interferometry, as the analytical h_c value indicates that it should be well above the range of measurable values (0-800 nm). Concerning the starved curves, an error-inducing source is related to the estimation of the oil supply h_{oil}. Equation (2.15) assumes that the contacts operate under pure rolling conditions. Nevertheless, the contact area of the specimen-disk contact presents sliding because of the spinning motion. With no spinning, the trail corresponding to the pure rolling conditions is centered along the x-axis. With spinning, in the case of the specimen, this trail moves sideways and crosses the

point with the maximum film thickness in the contact. Thus, special care has to be made to measure the required film thicknesses in the roller-disk and specimen-disk contacts associated to the same lubricant trail.

3.5. Conclusion

In this chapter, the numerical tools necessary to simulate EHD starved contacts were detailed. The model developed here was based on the previous work from Doki-Thonon [7] and Wheeler [1] and was adapted by implementing concepts from the biphasic fluid theory to describe the mixture fluid entrapped in the gap region as an equivalent fluid with uniform properties. The model has been validated by comparing the film thickness profiles of contacts under both no-spinning and spinning conditions and fully flooded and starved lubrication conditions to experimental film thickness measurements, as well as prediction formulae from the literature. Variations with respect to the experimental data were found to be 5% for the central film thickness and 17% for the minimum film thickness. It was highlighted that these differences might rise either from the lack of accuracy in the pressure-viscosity law of the lubricant or from experimental artifacts.

Thanks to this initial validation, the computational model will be used with confidence in the next chapter to explore the influence of starved lubrication conditions on spinning EHD contacts.

IV Spin and starvation in EHD contacts

The aim of this chapter is to evaluate and quantify the influence of spinning and starvation in EHD contacts, in terms of their film thickness profile. After a first analysis of spinning in circular fully flooded contacts, the chapter focuses on the effects of starvation in contacts with the same geometry and kinematic conditions. For each of these two distinct lubrication conditions (fully flooded and starved), a predictive formula for determining the critical minimum film thickness in the contact area is written. These findings are contrasted by experimental film thickness measurements obtained from the two test rigs: Jerotrib and Tribogyr. Finally, the study is extended to elliptical-shaped contacts.

4.1. Foreword

As previously indicated, when two solids in contact separated by a layer of lubricant move, a specific film thickness profile is generated. The oil distribution and geometry of the profile depend on the operating conditions of the contact (i.e., speed profile, load, lubricant viscosity or temperature, amongst others). In the case of rolling/sliding contacts, the film thickness profile is generally symmetric along the main direction of the flow, with a maximum film thickness at the geometrical center of the contact and two local minima located at the sides, forming two lobes. This symmetry can, however, be lost due to spinning, centrifugal effects or non-uniform feeding conditions. Finally, in the EHD lubrication domain, the film thickness encountered within the contact area varies from about a few μm down to a few nanometers. This film thickness, though seemingly small, is enough to sustain the contact and effectively separate the two solids in movement over time.

Since decades, effort has been put into describing how lubricated contacts behave. Many authors have attempted to quantity how the representative film thicknesses in the contact region evolved with the geometrical and operating conditions. In general, the focus has been set on the central and the minimum film thicknesses, at the geometrical center of the contact and its side lobes, respectively. The predictive formulae developed are based on the lubrication conditions (fully flooded or starved), the kinematic conditions (non-spinning or spinning) and/or the geometry (circular or elliptic) of the contact. Assuming fully flooded and non-spinning conditions, one can highlight the expressions derived from the studies of Hamrock and Dowson [18] [19], Nijenbanning *et al.* [85] and Masjedi and Khonsari [125], for circular and wide elliptical contacts; Evans and Snidle [126], for circular contacts; and Chittenden *et al.* [127], for circular and elliptical contacts, both slender and wide. Wheeler *et al.* [128] review these analytical expressions and evaluate their accuracy by comparing the predicted film thickness of various contacts with different operating conditions with respect to the corresponding values calculated by means of a finite element model. Assuming again fully flooded conditions, the predictive

formulae accounting for spinning are limited. Zou *et al*. [13] build on the above Hamrock and Dowson [18] [19] solution by using numerical data from simulations of spinning point contacts, under isothermal and Newtonian conditions. Similarly, Taniguchi *et al.* [17] derived a formula for predicting the minimum film thickness of spinning wide elliptical contacts, based on a reduction factor.

One must note that in spinning contacts the prediction of the central film thickness is not as meaningful as the minimum film thickness. Indeed, the studies from Dormois [5] and Doki-Thonon [7] reveal that the central film thickness might change in value with spin, but the overall maximum film thickness in the contact area will remain relatively unchanged. Nevertheless, the prediction of the central film thickness through analytical formulae captures the change in the lubricant distribution endured at the central region of the contact due to spin.

In contrast with the above fully flooded models, a series of formulae were likewise developed to describe the evolution of the film thickness profile when the inlet of the contact is partially filled with lubricant. Overall, these predictive expressions focus on rolling and sliding conditions and omit any spinning movement of the solids in contact. In this sense, the reader may be referred to the models from Wedeven [32] and Hamrock and Dowson [34], based on the position of the inlet air-oil meniscus. More recently, Chevalier [103] moved away from the previous paradigm and based his predictions on the amount of oil found upstream of the contact area. At the same time, his model set up an asymptotic behavior of the film thickness, which proved to be fairly accurate for the highly starved cases. The model was initially conceived for circular-shaped contacts, but has been eventually extended to elliptical contacts years later by Damiens *et al.* [45].

There is still a set of operating conditions that has not been explored yet, as discussed in Chapter I, namely how the film thickness distribution will behave when the contact operates under spinning and starvation at the same time. This set of conditions are expected to be particularly critical regarding the minimum film thickness. Indeed, as has been evidenced in previous works [11] [26], spinning generates an asymmetric film thickness profile, decreasing one of the minima at the side lobes. On the other hand, starvation decreases the film thickness of the entire contact area. Although the combined effects of both spinning and starvation have not been documented yet, both conditions are common in mechanical systems such as the roller-end/flange contact in rolling element bearings. Furthermore, starvation may become a recurring phenomenon in lubricated mechanical systems due to eco-friendly practices, aiming to improve efficiency and reduce costs. Having an accurate prediction of how the critical minimum film thickness changes with the operating conditions can thus be beneficial in avoiding material damage or failure. This chapter will explore and quantify the influence of both phenomena on the film thickness distribution of EHD contacts.

4.2. Nomenclature and representative film thicknesses

To better follow the analysis and discussion carried out in the next sections, Figure 4.1 introduces the notation used in this chapter concerning the representative film thicknesses in a spinning contact. The film thickness at the geometrical center of the contact is noted as $\mathrm{h_c}$. $\mathrm{h_{max}}$ is the maximum film thickness in the contact area, which is associated to the streamline with entrainment velocity $\mathrm{u_e}$, marked with a black dashed line. The minimum film thickness, at

the contact's side lobes, is noted as h_m. Here, the distinction between the high and low velocity regions in the contact are indicated with the subscripts "$_+$" and "$_-$", respectively.

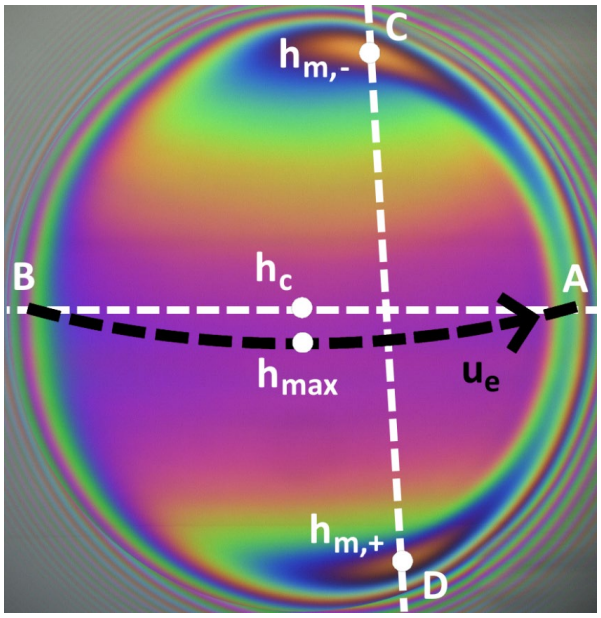

Figure 4.1. Representative film thicknesses in a spinning contact (interferogram extracted from [7]). The center of rotation of the specimen is found above the image.

In addition to this, four additional subscripts are employed to specify under which kinematic and lubrication conditions the film thicknesses are measured. They are "$_{sp}$" and "$_{ns}$" for spinning and non-spinning kinematic conditions, respectively, and "$_{ff}$" and "$_{st}$" for fully flooded and starved lubrication conditions, respectively.

4.3. Behavior of EHD circular spinning contacts in fully flooded lubrication

This section discusses the influence of spinning on the film thickness profile of fully flooded circular contacts. To do so, a series of contacts operating under isothermal conditions and with different entrainment speed and normal load are simulated. The contact is made between a steel spherical-end specimen and a steel plane (E = 210 GPa and ν = 0.30). The curvature radii in the x and y-directions, R_x and R_y, of the specimen is set to 80 mm. The lubricant selected is lubricant 2; its specific properties are reported in Chapter 3. The entrainment velocity u_e is varied between 0.5 and 10 m/s, the normal load w between 120 and 2675 N and the spin rotation velocity of the solid Ω between 0 and 5000 rad/s. These operating conditions are summarized in Table 4.1.

Parameter [Unit]	Value
u_e [m/s]	0.5 - 10
w [N]	120 - 2675
Ω [rad/s]	0 - 5000
R_x [mm]	80
R_y [mm]	80
T [°C]	30
μ_0 [mPas]	11.4
α^* [GPa^{-1}]	22.1
L [-]	4.7 - 9.9
M [-]	40.8 - 851

Table 4.1. Operating conditions of the contact simulated.

The set of operating conditions characterizing each contact is expressed as a pair of Moes dimensionless numbers [129], which are calculated according to:

$$L = (\alpha^* E') \left(2 \frac{\mu_0 u_e}{E' R_x}\right)^{0.25} \tag{4.1a}$$

$$M = \left(\frac{w}{E' R_x^2}\right) \left(2 \frac{\mu_0 u_e}{E' R_x}\right)^{-0.75} \tag{4.1b}$$

With the parameters detailed in Table 4.1, the contacts simulated are thus contained within a calculation domain registered between $L \in [4.7, 9.9]$ and $M \in [40.8, 851]$. This range of values covers a wide scope of the full EHL range.

Figures 4.2 and 4.3 show the variation of the representative film thicknesses $h_{m,-}$, $h_{m,+}$, h_c and h_{max} as a function of the dimensionless numbers L and M. This variation is expressed in terms of a ratio between the representative film thickness measured h and the same parameter evaluated under no spin and fully flooded conditions, at the same location, $(h)_{ff,ns}$. In Figure 4.2, the film thickness variation is indicated with respect to the L Moes number, with M constant at a value of 272. Similarly, in Figure 4.3, the same variation is represented with respect to the M Moes number, with L constant at a value of 6.6. In both figures, an arrow indicates the direction of increasing spin rotation velocity, which varies from 0 to 5000 rad/s.

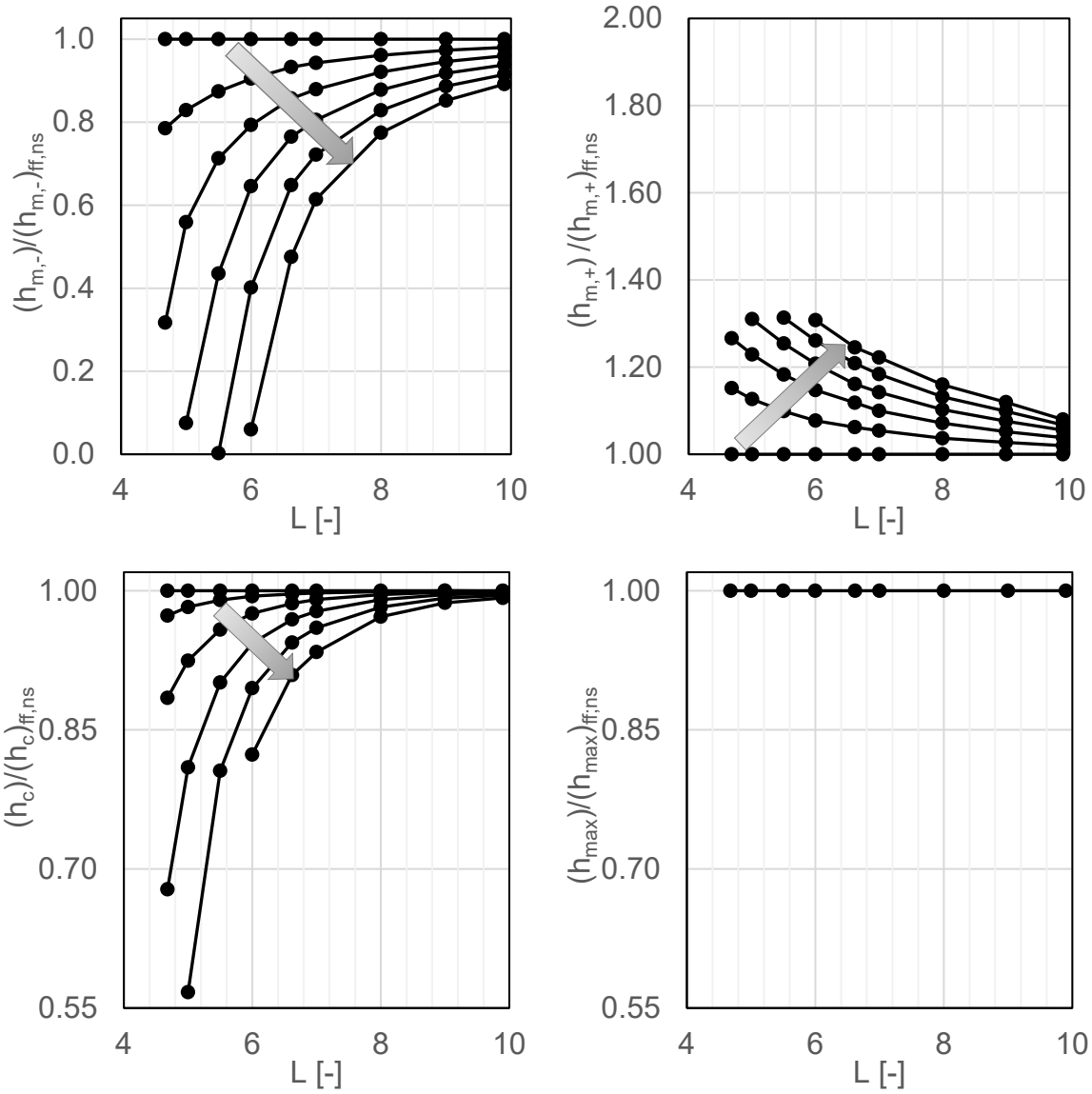

Figure 4.2. Variation of the representative film thicknesses with respect to the dimensionless number L and various spin rotation velocities, with M = 272. An arrow indicates the direction of increasing spin value.

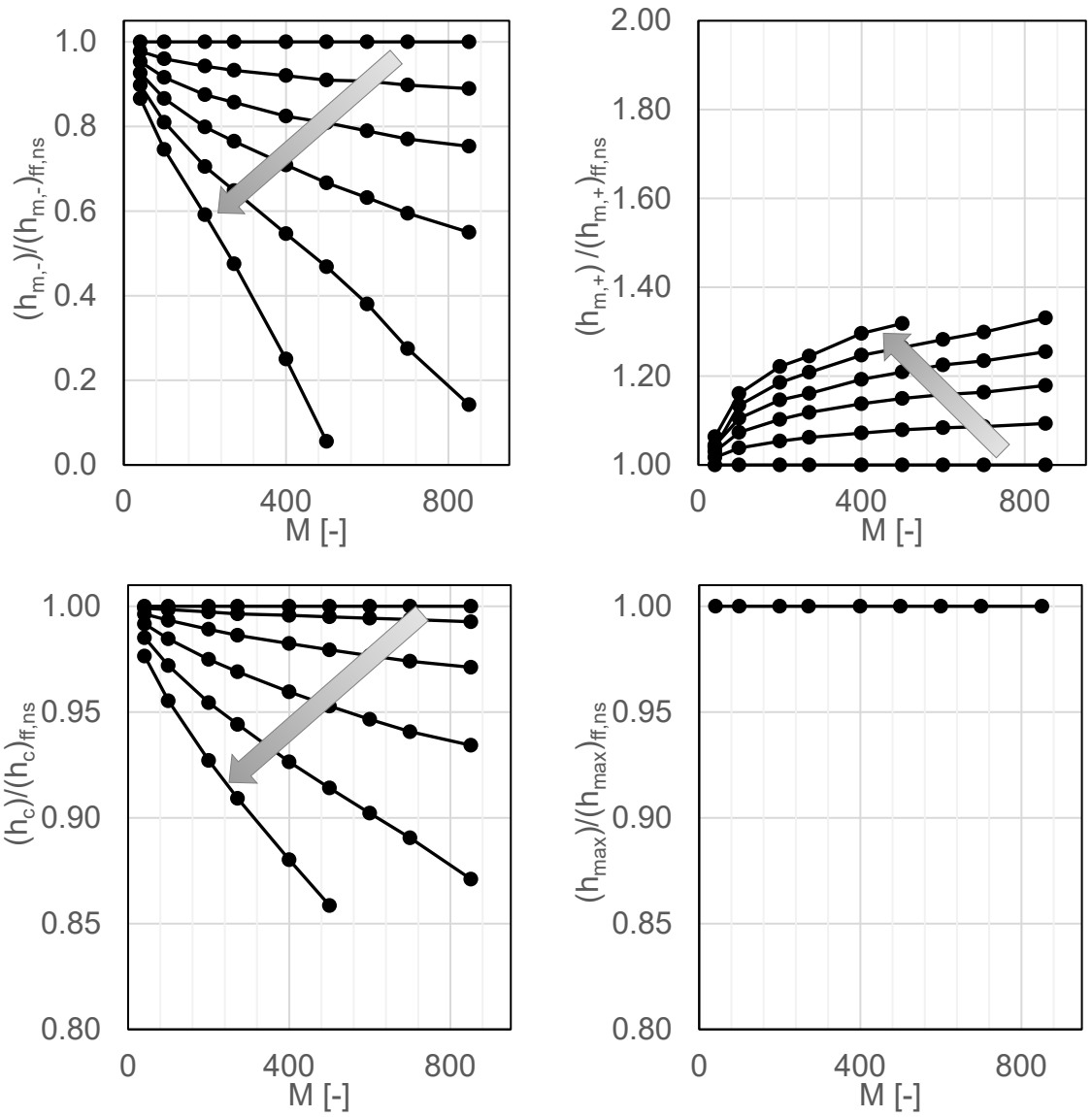

Figure 4.3. Variation of the representative film thicknesses with respect to the dimensionless number M and various spin rotation velocities, with L = 6.6. An arrow indicates the direction of increasing spin value.

The trends displayed in Figures 4.2 and 4.3 reveal specific behaviors already highlighted in the literature. When observing the variation of film thickness with spin, both figures show that increasing the spinning component of the kinematic field entails a loss in the symmetry of the contact. As a result of it, the values of $\mathrm{h_{m,-}}$ and $\mathrm{h_{m,+}}$ start to differ from the initial no-spin reference values. Furthermore, the film thickness variation of both minima is not carried at the same pace and so the film thickness reduction in the slow velocity region ($\mathrm{h_{m,-}}$) occurs faster than the gain of film thickness of its opposite minima ($\mathrm{h_{m,+}}$), where the local speed is faster. At the central region of the contact, the film thickness profile varies as well. The film thickness at the geometrical center of the contact $\mathrm{h_c}$ appears to decrease with spin. However, and more relevant, the maximum film thickness $\mathrm{h_{max}}$ experiences small to no change. When there is no

spin kinematics, $h_c = h_{max}$. This indicates that spin displaces the initial no spin value of h_c sideways in the direction where the local speed is higher (as shown in Figure 4.1).

For high L and low M values, the film thickness ratios tend to unity. On the other hand, the differences increase for low L and high M values. Moreover, these variations become significantly higher through the effect of spinning, as discussed before. Taking into account the definition of both dimensionless numbers (Equation (4.1)), the effects of the spinning movement on the film thickness profile are enhanced when the pressure distribution becomes more Hertzian in nature, that is, when the entrainment speeds are low and the normal loads applied are important. Following the same reasoning, similar consequences can be expected from small curvature radii and low lubricant viscosities. Indeed, with small curvature radii the contact area is smaller in size and thus the influence of the normal load is greater. Likewise, when the viscosity of the lubricant is low, its mobility is higher; there is less resistance to the flow.

The results in Figures 4.2 and 4.3, although obtained for a unique geometry such that $R_x = R_y$ = 80 mm, still apply to different circular geometries with different spin rotational velocities. Consider the three sets of operating conditions listed in Table 4.2, leading all to the dimensionless numbers L = 6.6 and M = 272. Their respective $h_{m,-}$ values under fully flooded conditions, for no-spin (0 rpm) and a high spin (5000 rpm) velocity are reported. They are expressed in units as well as in the dimensionless form:

$$H = h\frac{R_x}{a^2} \tag{4.2}$$

where R_x is the curvature radius in the x-direction and a the contact radius. Despite the noticeable variations in film thickness produced by the different operating conditions, under similar spinning velocities the dimensionless value is the same. The behavior and film thickness distribution of the contacts is similar. This implies that the film thickness ratios calculated would be comparable to those in the aforementioned diagrams.

Parameter [Unit]	Condition 1	Condition 2	Condition 3
u_e [m/s]	0.5	2	10
w [N]	50	800	20000
R_x (= R_y) [mm]	20	80	400
a [µm]	183.8	735.0	3675.1
$h_{m,-}$ (0 rpm) [nm]	37.3	148.6	745.5
$h_{m,-}$ (5000 rpm) [nm]	17.85	70.65	356.95
$H_{m,-}$ (0 rpm) [-]	0.0221	0.0220	0.0221
$H_{m,-}$ (5000 rpm) [-]	0.0106	0.0105	0.0106

Table 4.2. Different sets of operating conditions leading to L = 6.6 and M = 272 (fully flooded conditions). The parameters not specified (T, μ_0 and α^*) correspond to those of Table 4.1.

The study from Taniguchi *et al.* [17] portrays the variation of $h_{m,-}$ for different wide elliptical contacts as a function of a dimensionless spin number $B' = 2\Omega R_x/u_e$, from which a predictive formula is extracted. The spin-to-roll ratio, as they defined it, takes into account the spin rotational velocity Ω, the entrainment speed u_e and the curvature radius R_x of the contact. Their representation of the film thickness values indicates a linear variation with spin, with the slope being dependent exclusively on the normal load; other operating or geometric parameters were excluded from the analysis. When applying the same criteria to the $h_{m,-}$ values from Figures 4.2 and 4.3, it is revealed that the trends actually lose the linearity with high spin-to-roll ratios and bend.

An alternative definition of the spin-to-roll ratio is proposed here to consider the influence of the contact's size on spinning. The new definition of the spin-to-roll ratio reads:

$$B = \frac{2\Omega a}{u_e} \tag{4.2}$$

where a is the contact radius. By doing so, contrary to what is seen with the previous definition of the spin-to-roll ratio used by Taniguchi *et al.*, the curves tend to follow a unique trend, regardless of the operating conditions, with some distinctions for the high spin cases. This trend is illustrated in Figure 4.4. It is also important to highlight that the range of spinning values covered in Figure 4.4 is much larger than that of Taniguchi *et al.*

The $h_{m,-}$ ratios from Figures 4.2 and 4.3 are included in the form of a film thickness reduction coefficient C_{sp}, expressed as:

$$C_{sp} = 1 - \frac{(h_{m,-})_{ff,sp}}{(h_{m,-})_{ff,ns}} \tag{4.3}$$

where $(h_{m,-})_{ff,sp}$ is the value of the critical minimum film thickness under fully flooded conditions and spinning and $(h_{m,-})_{ff,ns}$ is the reference value of the same parameter under fully flooded conditions and no spin. The points from Figure 4.2 are indicated in blue and those from Figure 4.3 in yellow. They are fitted into a curve, which is represented with a continuous black line. Two arrows indicate the direction of increasing spin values and $h_{m,-}$ reduction. The best fit curve is associated to the expression:

$$C_{sp} = 0.26\left(e^{0.27B} - e^{-0.1B}\right) \tag{4.4}$$

In addition, some experimental C_{sp} values are represented, calculated from film thickness measurements obtained by Doki-Thonon [7] with Tribogyr. In this case, the contacts were performed between a steel spherical-end specimen (R_x = 80 mm) and a glass disk. The entrainment velocity was varied between 1 and 2 m/s, the load between 400 and 800 N, and the spin rotational velocity between 716 and 1050 rad/s. The lubricant employed was lubricant 2. The inlet temperature was set to 30°C. Thus, the experimental points concern $L \in [5.6, 6.6]$ and $M \in [135, 460]$.

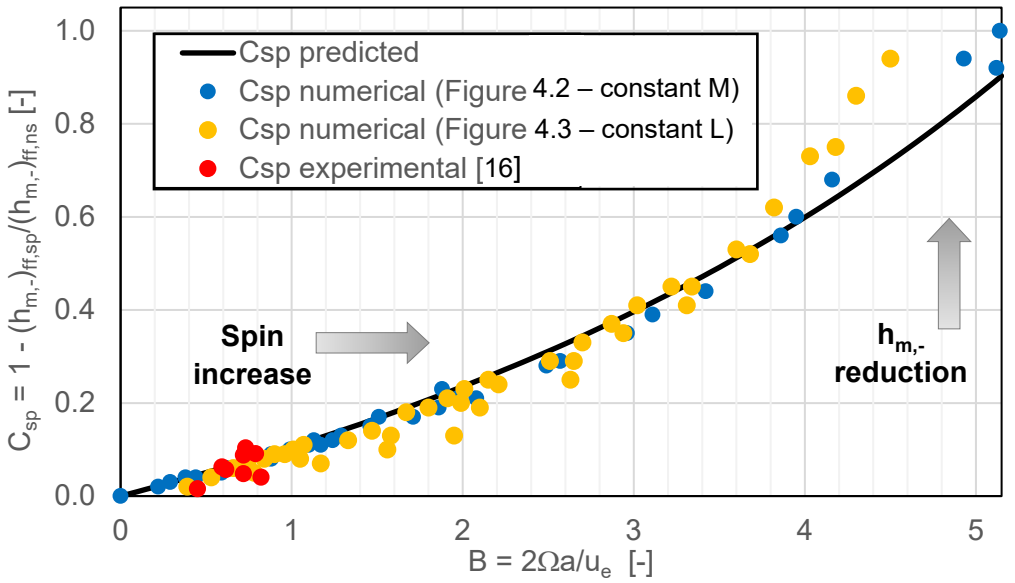

Figure 4.4. Effect of the spin-to-roll ratio B upon the critical minimum film thickness for different operating conditions. Experimental points calculated from data extracted from [7].

The points plotted indicate a continuous increase of the film reduction coefficient C_{sp} with spin, i.e. a decrease of the critical film thickness $h_{m,-}$, regardless of the operating conditions and geometric parameters chosen. The followed trend is unequivocal despite the variety of (L,M) pairs represented. However, an important deviation with respect to the predicted behavior occurs for spin-to-roll ratios above the value of 4. For these cases, the trends for the two numerical conditions considered (constant L and variable M, on the one hand, and variable L and constant M, on the other) begin to differ. In fact, the constant L points (in yellow) rise more importantly at high B ratios and reduce the film thickness in the contact's critical region faster than the points linked to constant M values (in blue). This might indicate that at high spin the normal load plays a significant influence on the film thickness minima reduction. Despite this divergence with respect to the predicted behavior found at extreme spinning conditions, the prediction is still accurate for a broad range of operating conditions. This is shown for the experimental C_{sp} points, derived from the measurements from Doki-Thonon [7]. The film thickness reduction values provided by Taniguchi *et al.* [17] cannot be represented along the previous points, as they concern wide elliptical contacts and not circular ones.

An expression can then be written to define the critical minimum film thickness of circular contacts under fully flooded and spinning conditions $(h_{m,-})_{ff,sp}$ based on the value of the same parameter under fully flooded conditions and no spin $(h_{m,-})_{ff,ns}$.

$$(h_{m,-})_{ff,sp} = (h_{m,-})_{ff,ns} \cdot (1 - C_{sp}) \tag{4.5}$$

where C_{sp} is the film thickness reduction factor due to spin, described in Equation (4.4).

4.4. Influence of starvation on EHD spinning circular contacts

4.4.1 Numerical approach

This section discusses the influence of spinning on starved circular contacts. For that task, various EHD steel-on-steel contacts combining variable amounts of spin and starvation degrees are studied. The curvature radius R_x is set to 80 mm, the normal load to 800 N and the entrainment speed to 2 m/s. The spin rotation velocity of the upper solid is changed, resulting in spin-to-roll ratios between 0 (no spin) and 3.7 (high spin). The lubricant employed is lubricant 2. The new operating conditions of the study are summarized in Table 4.3.

Parameter [Unit]	Value
R_x [mm]	80
R_y [mm]	80
u_e [m/s]	2
Ω [rad/s]	0 - 5000
B	0 - 3.7
w [N]	800
P_H [GPa]	0.71
r_c [-]	0 - 192
T [°C]	30
μ_0 [mPas]	11.4
α^* [GPa^{-1}]	22.1
L [-]	6.6
M [-]	272.3

Table 4.3. Operating conditions of the contact.

Figure 4.5 shows the variation of the maximum (h_{max}) and critical minimum ($h_{m,-}$) film thicknesses with the amount of lubricant found upstream of the contact inlet (h_{oil}). Both film thicknesses are represented in the dimensionless form:

$$R = h/h_{c,ff} \tag{4.6}$$

where , $h_{c,ff}$ is the film thickness at the geometrical center of the contact under fully flooded conditions and no spin. The oil supply h_{oil} is likewise expressed in the dimensionless form:

$$r_c = h_{oil}/\left(h_{c,ff} \cdot \bar{\rho_c}\right) \tag{4.7}$$

where $\bar{\rho_c} = \rho/\rho_0$ is the dimensionless density, used to take into account the compressibility effect of the lubricant. The corresponding R values predicted by the Chevalier model [44], for the no-spin cases, are traced as a continuous line.

The average relative deviation of the computed film thickness with respect to the prediction made by Chevalier is 9.8% for h_c and 9.5% for $h_{m,-}$, for the specific operating conditions defined in Table 4.3 and no spinning.

Alongside the prediction, the two characteristic asymptotes of the analytical model are traced with dashed lines. The asymptote $R_c = 1$ (for $r_c \geq 1$) represents the limit defined by the fully flooded contact, whereby the remaining oil flows around it. On the other hand, the asymptote $R_c = r_c$ (for $r_c \leq 1$) represents the limitation of the oil supply on the contact's film thickness as well as the amount of oil on the track. Two arrows indicate the direction of increasing spin value and degree of starvation.

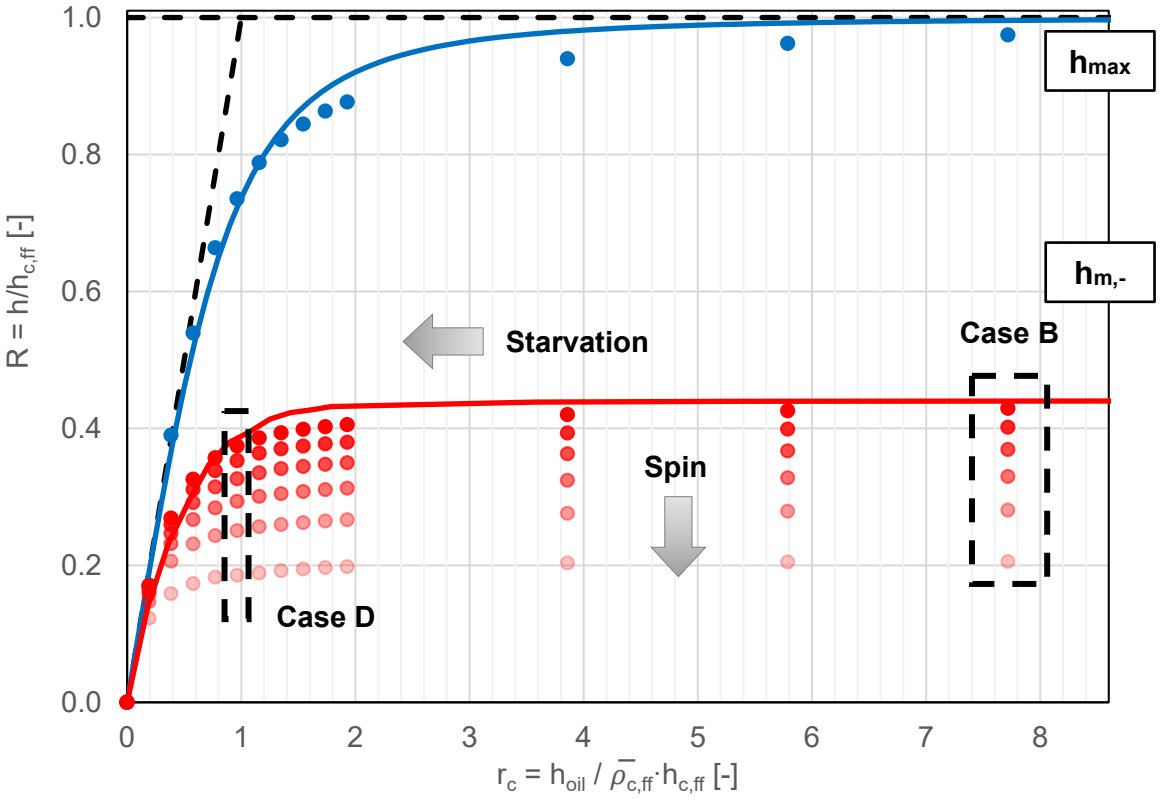

Figure 4.5. Dimensionless maximum (R_{max}) and critical minimum ($R_{m,-}$) film thickness variations with respect to the dimensionless oil supply (r_c) for different spin velocities (u_e = 2 m/s, w = 800 N, T = 30°C, R_x = R_y = 80 mm). The predictions of the Chevalier model [44] are plotted in continuous lines and concern the no-spin results only.

The local maximum and critical minimum film thickness points plotted in Figure 4.5 decrease with starvation following the two asymptotic trends defined above. A critical value for the oil supply, delimiting the fully flooded and starved domains, can be estimated at $r_c \approx 5$. This value represents a film thickness reduction of 5% of h_{max} with respect to the film thickness when $r_c = \infty$. As evidenced in Figures 4.2 and 4.3, the maximum film thickness does not vary when spinning is introduced, even when the contact is starved. The critical minimum film thickness $h_{m,-}$ on the other hand is reduced with respect the no-spin behavior. The asymptotic behavior

of the curves is maintained for the different spinning conditions, but the transition between the fully flooded and starved behaviors moves towards lower r_c values.

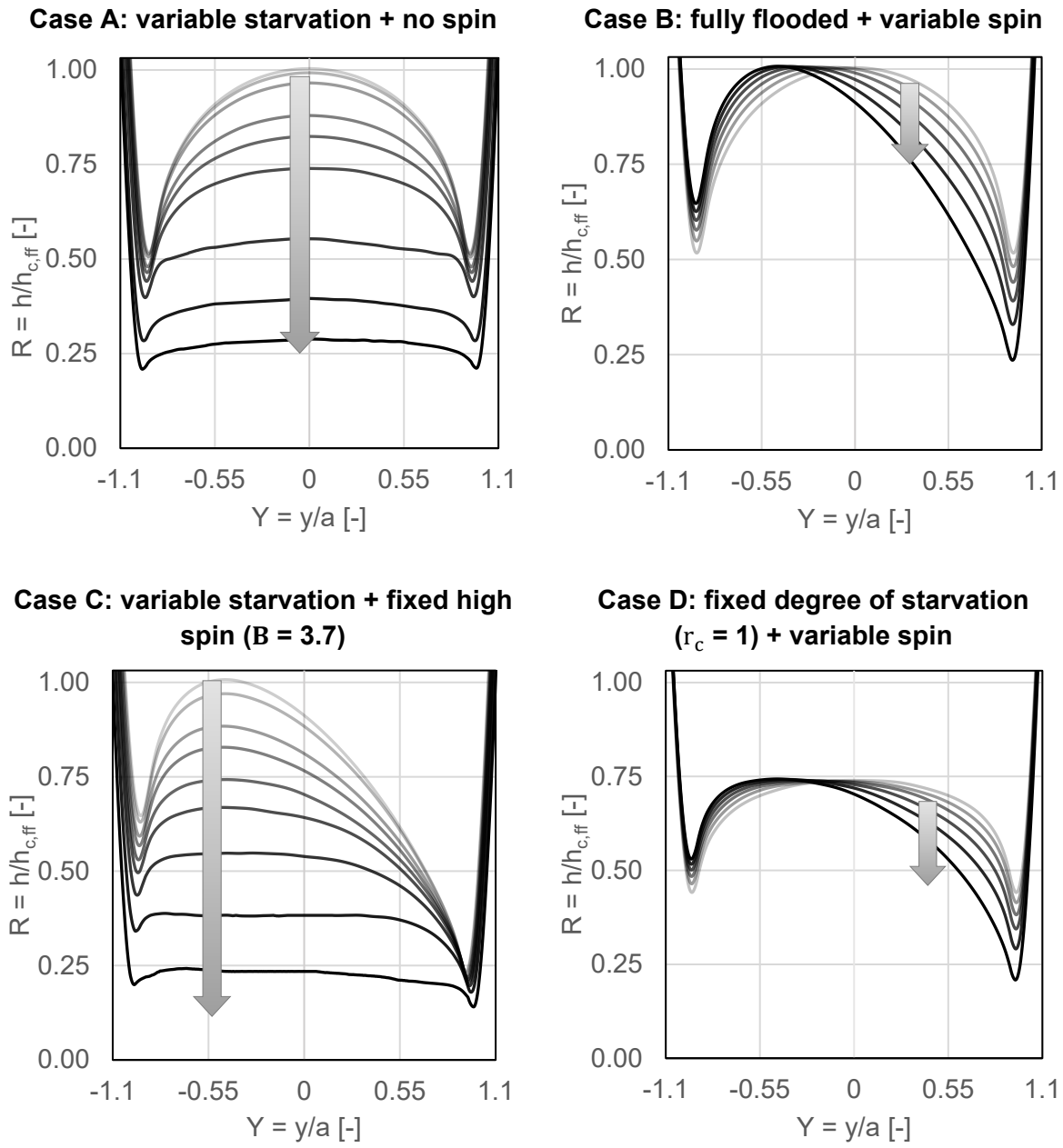

Figure 4.6. Transversal film thickness profiles for different study cases extracted from Figure 4.5. The arrows indicate the direction of increasing spin (cases B and D) or degree of starvation (cases A and C).

In order to analyze the individual and combined effects of spinning and starvation, four study cases have been extracted from Figure 4.5, two of which have been highlighted in the same figure (Case B and Case D). Figure 4.6 depicts the dimensionless film thickness profiles of the contacts along an axis transverse to the main direction of the flow, crossing the center of the contact. The film thickness values are expressed in the dimensionless form $R = h/h_{c,ff}$ to

quantify the variations in film thickness with respect to its fully flooded and no-spin case. An arrow indicates the direction of increasing spin (in study cases B and D) or degree of starvation (in study cases A and C).

The set of curves in case A corresponds to contacts with no spin and variable degrees of starvation. The film thickness profiles are symmetric with respect to the direction of the flow. For these operating conditions, the overall film thickness of the contact is reduced and depends on the amount of lubricant available at its inlet. The film thickness reduction rate is not the same for the entire profile. As seen in the figure, it occurs at a faster pace at the center of the contact than at the side lobes (75% total reduction of h_c against 40% for h_m, with respect to the cases displayed).

The set of curves in case B (also highlighted in Figure 4.5) corresponds to fully flooded contacts with variable amounts of spin. The introduction of a spinning component into the kinematic film entails a loss of the symmetry previously seen in the profiles from case A. Now, the film thickness of the local minima at both side lobes (distinguished between $h_{m,+}$ for $Y < 0$ and $h_{m,-}$ for $Y > 0$) differ. In the $Y > 0$ area, the local velocity is slower than in the opposite $Y < 0$ region and thus a thinner h_m is expected. Furthermore, the film thickness reduction in $Y > 0$ is more important than the film thickness increase in $Y < 0$ (35% total film thickness reduction against 15% film thickness increase, for the cases displayed). On the other hand, the maximum film thickness of the profiles remains constant and its location is shifted to the side with higher velocity, where the entrainment velocity u_e is found. A complete analysis on this kind of contact was carried out by Dormois *et al.* in [26].

The set of curves in case C corresponds to contacts with a fixed high spin value (B = 3.7) and variable degrees of starvation. The profiles show an asymmetric shape as a result of the spinning nature of its kinematic field, with its maximum film thickness located at a constant position Y due to the fixed value of the spinning component. By increasing the degree of starvation of the contact, the overall film thickness of the profile is lost progressively. Contrary to case B, the film thickness reduction of $h_{m,+}$ is more important than in its counterpart $h_{m,-}$ (60% against 15%); starvation is revealed to reduce the influence of spinning in the contact area. Similar to the behavior seen in case A, the film thickness reduction rate at the center of the contact is higher than at the side lobes (a total variation of 85%, with respect to the cases displayed). However, with both spinning and starvation film thicknesses are still lower than in the no-spin case (case A), which shows the combined influence of both conditions.

The set of curves in case D (also highlighted in Figure 4.5) corresponds to contacts with variable amounts of spin and a fixed lubricant supply r_c = 1 (starved conditions). The behavior of these profiles is similar to those depicted in case B. However, the curves show a reduced film thickness as a consequence of the limited oil supply, which leads the contact to operate in the starved lubrication domain. The introduction of spin brings asymmetry into the profiles. The maximum film thickness value remains independent of spin; it matches the central film thickness of the contact with no spin and identical lubrication conditions (represented in case A). This maximum film thickness is, again, shifted towards the side with higher local velocity, as seen in case B. Compared to it, the film thickness reduction in $h_{m,-}$ results in 25% against 10% for $h_{m,+}$.

In contrast, the pressure profiles associated to the contacts in Figure 4.6 confirm that, for identical lubrication conditions, spin has little to no effect on the pressure distribution. This is discussed by Dowson *et al.* [11]. Significant changes in the pressure distribution are only confirmed by limiting the oil supply [32], which affects the film formation capacity at the contact's inlet.

In order to observe the effects of starvation and spinning on the film thickness profile of the entire contact area, Figure 4.7 shows four numerical interferograms selected from the results plotted in Figure 4.6. The first and second rows represent fully flooded and starved (r_c = 1), respectively, whereas the first and second columns represent no spin and spin (B = 3.7) conditions, respectively. The numerical interferograms show that, under identical spinning conditions, their aspect is similar. Likewise, under identical lubrication conditions, the maximum film thickness in the contact area is similar.

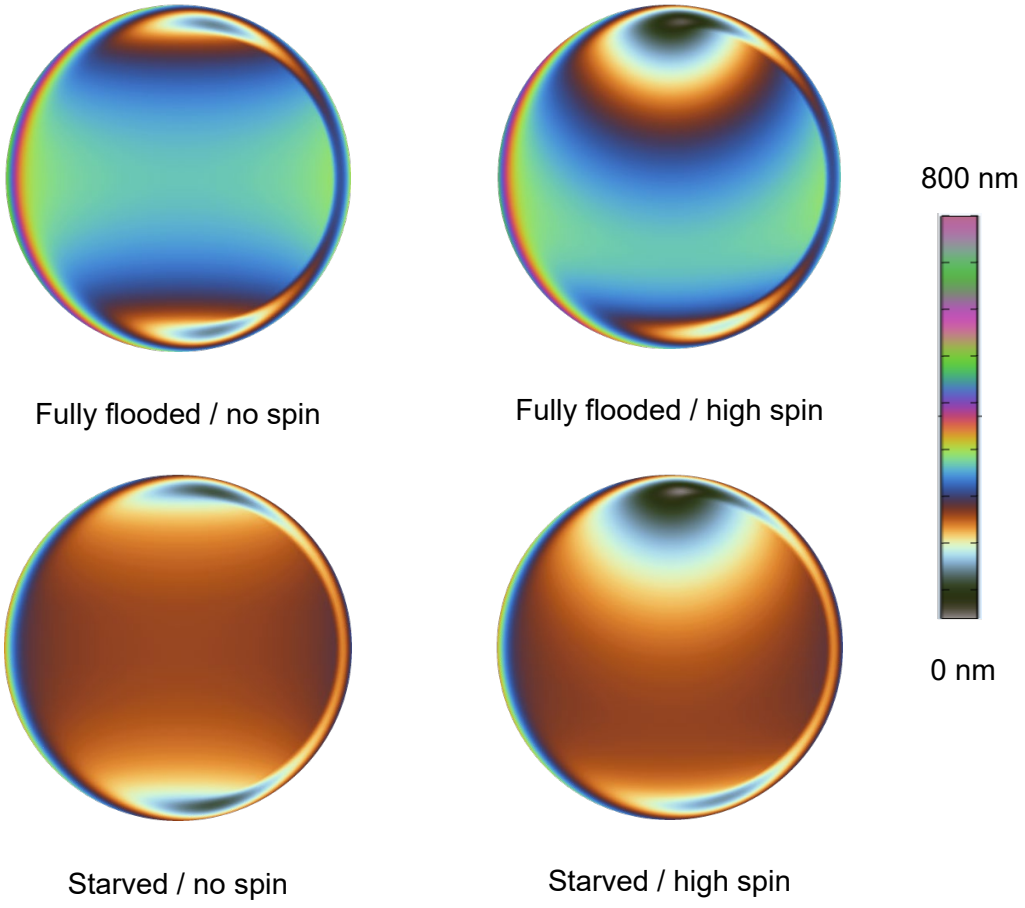

Figure 4.7. Numerical interferograms for four selected cases presented in Figure 7, for fully flooded and starved (r_c = 1) conditions, without spin and with high spin (B = 3.7).

Figure 4.8 represents the relative variation of the critical minimum film thickness $h_{m,-}$ with respect to the oil supply h_{oil}, for any kinematic condition (spin or no-spin). The oil supply is written in the dimensionless form $h_{oil}/(h_c)_{ff,ns}$, with $(h_c)_{ff,ns}$ the film thickness of the contact at

its geometrical center, under fully flooded conditions and no spinning. This variation is expressed as a film thickness reduction coefficient C_{st}, which reads:

$$C_{st} = 1 - \left(h_{m,-}\right)_{st} / \left(h_{m,-}\right)_{ff} \tag{4.8}$$

where $\left(h_{m,-}\right)_{st}$ is the critical minimum film thickness under starvation and $\left(h_{m,-}\right)_{ff}$ is the same parameter under fully flooded conditions; both are measured in the same spinning conditions.

The blue points represent the reduction coefficient C_{st} relative to the minimum film thickness values from Figure 4.6 (L = 6.6 and M = 272.3), with its operating conditions indicated in Table 4.3. The film thickness reduction coefficient of three no-spin additional operating conditions are plotted. They relate to a variable lubricant supply and no spinning. For each case, both the numerical value of the coefficient and its corresponding experimental value (obtained with Jerotrib, already presented in the previous chapter) are plotted. They are represented in red (L = 6.2 and M = 117.3), yellow (L = 7.4 and M = 69.3) and green (L = 8.2 and M = 51.1). They represent different operating conditions: steel-on-glass contact, under entrainment speeds of 0.16, 0.32 and 0.48 m/s, respectively. The lubricant considered is lubricant 1 and the curvature radii of the test ball is R_x = R_y = 12.7 mm. The temperature is set to 30 °C.

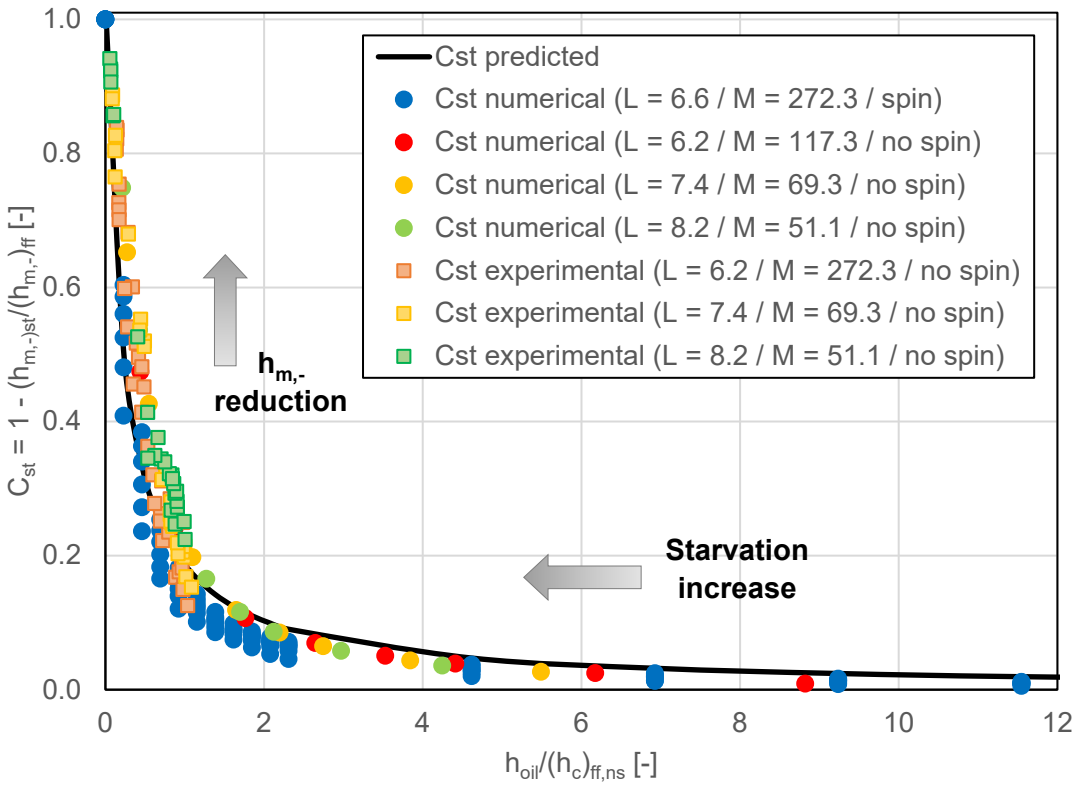

Figure 4.8. Variation of the critical film thickness reduction C_{st} as a function of the oil supply and for different operating conditions (L and M pairs), with and without spinning obtained from simulations and experiments. The arrows indicate the direction of increasing starvation and $h_{m,-}$ reduction.

The effect on starvation on the critical minimum film thickness $h_{m,-}$, indicated through C_{st}, is then fitted into an expression depending exclusively on $h_{oil}/(h_c)_{ff,ns}$. The best predictive function is expressed as:

$$C_{st} = 1 - \frac{0.228}{\frac{h_{oil}}{(h_c)_{ff,ns}} + 0.223} \tag{4.9}$$

with h_{oil} the equivalent oil film thickness upstream of the contact inlet and $(h_c)_{ff,ns}$ the central film thickness under fully flooded conditions and no spinning.

Equation (4.9) only takes into account the influence of the oil supply on the film thickness. In Figure 4.8, one can observe the reduction of the critical minimum film thickness (expressed through the rate C_{st}) with the degree of starvation. This evolution seems, in fact, nearly independent of the spinning kinematics of the contact, as the spin and no-spin film thickness values are superposed with each other. However, the vertical deviation of the spin measures in blue (same oil supply, but different spin rotational velocity) indicate that the kinematics of the contact still exerts an influence on the results, even though the effect is relatively weak. The maximum deviation with respect to the fitted behavior is found for the highly starved cases. Here, the difference with respect to the predicted value from Equation (4.9) is 12%. For mildly starved contacts (i.e. $h_{oil}/(h_c)_{ff,ns} > 2$), this difference is less than 5%. The validity of Equation (4.9) is therefore limited. Further research is required to observe to what extent does the parameter C_{st} vary with respect to the fit curve for high spin rotational velocities (e.g. Ω = 5000 rad/s) and high degrees of starvation ($h_{oil}/(h_c)_{ff,ns}$ < 1).

It is observed in Figure 4.5 that, under identical lubricant supply, the introduction of a spinning component in the kinematic field reduces the critical film thickness value. If the contact is also starved, it further drops down and the differences between the film thickness measures of similarly spinning contacts are reduced. However, this last variation with the lubricant supply is not linear. Figure 4.5 confirms that variations of the film thickness occur at a faster pace the higher the degree of starvation. Thus, the original slope $R = h/h_{c,ff}$ relative to the minimum film thickness becomes steeper.

This behavior results from combining two effects related to the velocity and pressure fields of the contact. When there is no spinning motion, the velocity along the y-direction of the lubricant entering the contact area does not change. However, when spinning is introduced, a speed gradient inside the contact area is generated. Hence, higher local speeds entail a higher flow of lubricant in this specific contact region, while regions with slower local speeds receive less lubricant amount. This entails that the effect of starvation on the local film thickness is more important in the high velocity region ($Y < 0$) than in its slower counterpart ($Y > 0$). Therefore, spinning intensifies the local effects of starvation and starvation compensates the dissymmetry entrained by spinning. This can be observed in Figure 4.6 (case C), where the difference between both local minima at the side lobes is reduced by increasing the degree of starvation. Starvation inhibits the film formation capacity of the contact at its inlet region [33], affecting the pressure distribution to become more Hertzian-like in nature. On the other hand, spin has little to no effect on the pressure profile [11]. For starved contact conditions, the amount of lubricant entrapped within the contact region is smaller, which supposes a smaller relative difference

between the film thickness minima at the side lobes. The comparison between the curves for cases B and D in Figure 4.6 confirm this behavior. Even though the dissymmetry originally entrained by spinning still exists, the film thickness profiles tend to be uniform. With less amount of lubricant entrapped in the contact area, less oil is redistributed from one side of the contact to the opposite one due to internal flows, which are generated by spinning.
With the above description of the behavior of a spinning and starved contact, its critical minimum film thickness $\left(h_{m,-}\right)_{st,sp}$ can be estimated according to Equation (4.10), valid for the specific operating conditions presented in this section and for circular contact geometries. Taking Equation (4.5) as a starting point, the predictive function results in:

$$\left(h_{m,-}\right)_{st,sp} = \left(h_{m,-}\right)_{ff,ns} \cdot \left(1 - C_{sp}\right) \cdot \left(1 - C_{st}\right) \tag{4.10}$$

with C_{sp} the film thickness reduction factor due to spin, described in Equation (4.4), and C_{st} the film thickness reduction factor due to starvation, defined in Equation (4.9). $\left(h_{m,-}\right)_{ff,ns}$ is the critical minimum film thickness under fully flooded conditions and no spin.

4.4.2 Film thickness measurements

The latest results presented in section 4.4.1 have been validated experimentally by Tribogyr, described in Chapter II. The Interferograms of contacts combining spinning and starvation in different degrees have been obtained, from which the respective film thickness profiles and $h_{m,-}$ values have been extracted. A roller (R_x = 11 mm and R_y = 269 mm) was placed upstream of the test ball in order to limit its oil supply and thus starve it. The spherical-end specimen employed (R_x = R_y = 50 mm) has been tilted a spin angle λ of 0.8° (high spin), 1.6°, 3° and 9° (low spin) and has been put into rotation with a rotational velocity Ω of 928, 358, 125 and 62 rad/s, respectively. The temperature at the contact's inlet is 30°C. Lubricant 1 was used for the experiences. The operating conditions are gathered in Table 4.4.

Parameter [Unit]	Condition 1	Condition 2	Condition 3	Condition 4
R_x (= R_y) [mm]	50			
u_e [m/s]	0.5			
w [N]	400			
P_H [GPa]	0.50			
T [°C]	30			
μ_0 [mPas]	148.0			
α^* [GPa^{-1}]	21.2			
Ω [rad/s] / B [-]	628 / 1.580	358 / 0.901	125 / 0.315	62 / 0.156
λ [°]	0.8	1.6	3	9
L [-]	5.9	5.9	5.9	5.9
M [-]	119.2	119.2	119.2	119.2

Table 4.4. Operating conditions of the contact operated during spinning experiments with and without starvation conditions.

Figure 4.9 presents the series of interferograms from Tribogyr associated to the operating conditions from Table 4.4: condition 1 for images a to e and condition 2 for images f to i. Although the geometry of the spherical-end specimen ($R_x = R_y$) is expected to generate a circular contact area, upon close examination of images a-e, related to a high spin angle, the ellipticity ratio of the contacts is estimated to be around 1.2. This deviation with respect to the expected contact shape is more likely due to the local wear and plastic deformation of the specimen's head as a result of extreme contact conditions from previous experiences at this specific spin angle. This permanent deformation of the specimen's head could not be corrected by a standard polishing procedure and would require a more extensive and dedicated work. On the other hand, the high spin angle images f-i do not present this issue and their contact area appears circular. Indeed, amongst other factors, low spin angles are generally linked to high spin rotational velocities, with their center of rotation being close to the contact area.

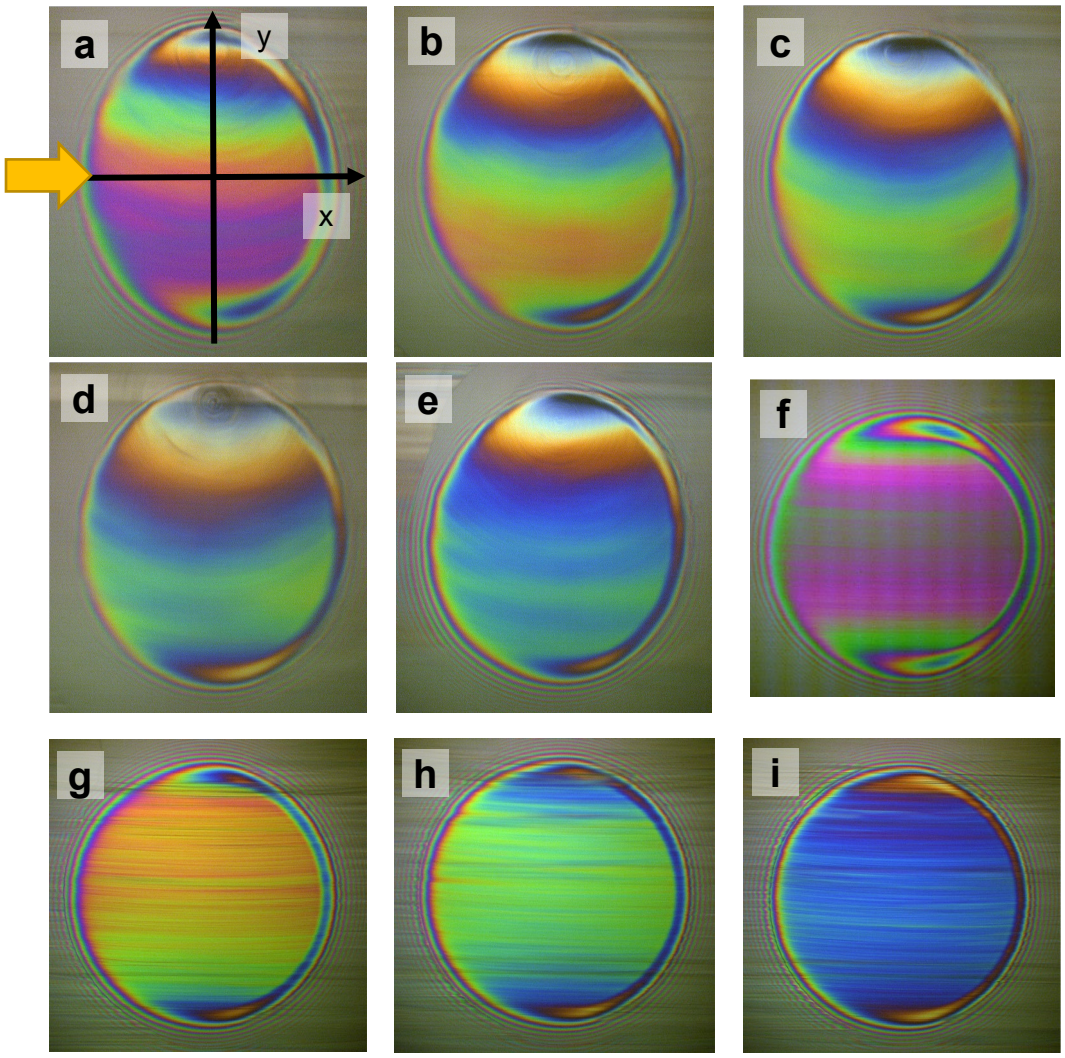

Figure 4.9. Experimental interferograms for the operating conditions in Table 4.4. Images a-e correspond to high spinning/low spin angle (condition 1: h_{oil} = inf, 669, 591, 573 and 508 nm) and images f-i to low spinning/high spin angle (condition 4: h_{oil} = inf, 574, 464 and 300 nm).

Figure 4.10 shows the film thickness profiles along an axis transversal to the direction of the main flow for interferograms a to e. The behavior observed is similar to case C in Figure 4.6: while the local side lobe minima decreases in a small proportion, the main film thickness variation takes places with respect to the maximum film thickness value, when the oil supply is limited. This trend can also be perceived intuitively through the series of interferograms shown in Figure 4.9. Starting from the original fully flooded contact, depicting a continuous color variation along the y-direction (from blue to violet, going through green, yellow and orange), the color of the contact area becomes uniform the more starved the lubrication conditions are. Compared to the fully flooded contact, the color of the contact area becomes predominantly blue, indicating that there is less film thickness variation. Indeed, this is verified by the set of curves traced in Figure 4.10.

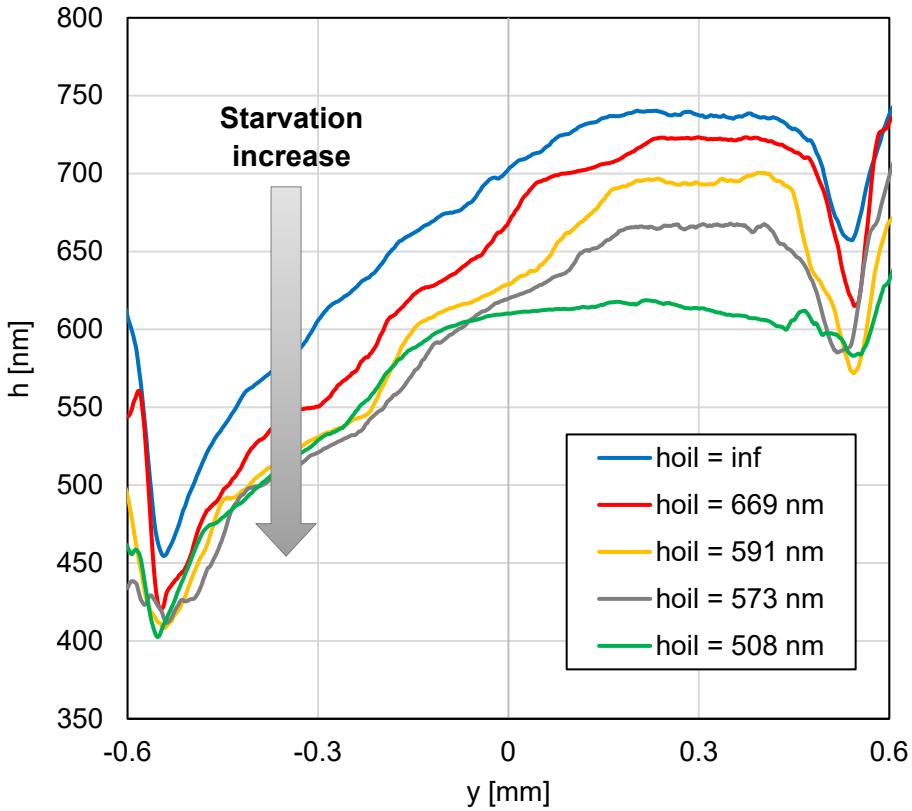

Figure 4.10. Experimental film thickness profiles for interferograms a to e (u_e = 0.5 m/s, w = 400 N, Ω = 628 rad/s, λ = 0.8°, T = 30°C, R_x = R_y = 50 mm).

Table 4.5 lists the $h_{m,-}$ values represented in the set of interferograms from Figure 4.10 (noted as “Experim.”) and compares them to the estimations from the analytical formula in Equation (4.10) (noted as “Analytical”) and the Hamrock and Dowson formula [19] (noted as “HD”). In the case of the Hamrock and Dowson formula, it is only applicable for the fully flooded cases (images a and f). It is relevant to note that no reference $h_{m,-}$ value (fully flooded and no-spin conditions) was able to be obtained experimentally. Therefore, in order to apply Equation (4.9), the $h_{m,-}$ measurement from Image f (λ = 9°) is taken as a reference (no-spin/fully flooded) value and so the spin-to-roll ratio B is assumed 0 for the subsequent film thickness predictions.

This assumption, used only for the high spin angle λ, is made on the basis of the experimental study on spinning conducted by Dormois in [26], whereby it is shown that the influence of spinning on the contact's film thickness distribution is negligible when $\lambda \geq 9°$. The actual spinning conditions for this set of contacts is indicated in parenthesis.

	Ω [rad/s]	B [-]	h_{oil} [nm]	$h_{m,-}$ [nm]		
				Experim.	Analytical	HD
Image a	628	1.580	inf	468.0	459.1	380
Image b	628	1.580	669	417.8	366.4	n/a
Image c	628	1.580	591	411.2	356.9	n/a
Image d	628	1.580	573	407.5	354.4	n/a
Image e	628	1.580	508	402.6	344.2	n/a
Image f	0 (62)	0 (0.156)	inf	557.4	557.4	435
Image g	0 (62)	0 (0.156)	573	468.0	429.0	n/a
Image h	0 (62)	0 (0.156)	464	390.0	406.8	n/a
Image i	0 (62)	0 (0.156)	300	224.4	353.9	n/a

Table 4.5. Operating conditions for the images illustrated in Figure 4.8 and comparison of $h_{m,-}$ estimated by: experiments ("Experim."), the numerical model from the present study ("Analytical") and Hamrock and Dowson formula [19] ("HD").

The apparent ellipticity of contacts a to e have not been taken into account for any of the previous calculations. The next section explores this issue in more detail and proposes an extension of Equation (4.10) to these conditions. However, with the current model, in spite of the simplifications made, a fair degree of accuracy in the estimations is achieved. For images a to h the relative error is below 14.5%, only for the highly starved lubrication conditions of image i the error goes well above this value.

Figure 4.11 gathers the $h_{m,-}$ values for the four spinning angles and operating conditions listed in Table 4.4 and plots them with respect to h_{oil}, the corresponding lubricant supply of the contact. Both film thickness and oil supply are represented in the dimensionless form R (Equation (4.6)) and r_c (Equation (4.7)), respectively. The characteristic asymptotes of the Chevalier model [44] are likewise traced. Qualitatively, it can be observed that the behavior of $h_{m,-}$ remains asymptotic with starvation in spite of the spinning component of the velocity, corroborating one of the main trends from Figure 4.5. Similarly, it is also seen, particularly for the fully flooded results, that spinning induces a reduction of the film thickness. However, for the operating conditions performed this variation is only about 14%, between the low and high spin angle cases. The limited experimental data points out that these differences are reduced with starvation (superposition of the points where $r_c \approx 0.33$), but further experimental film thickness measurement would be helpful to delimit independently each angle's trend accurately.

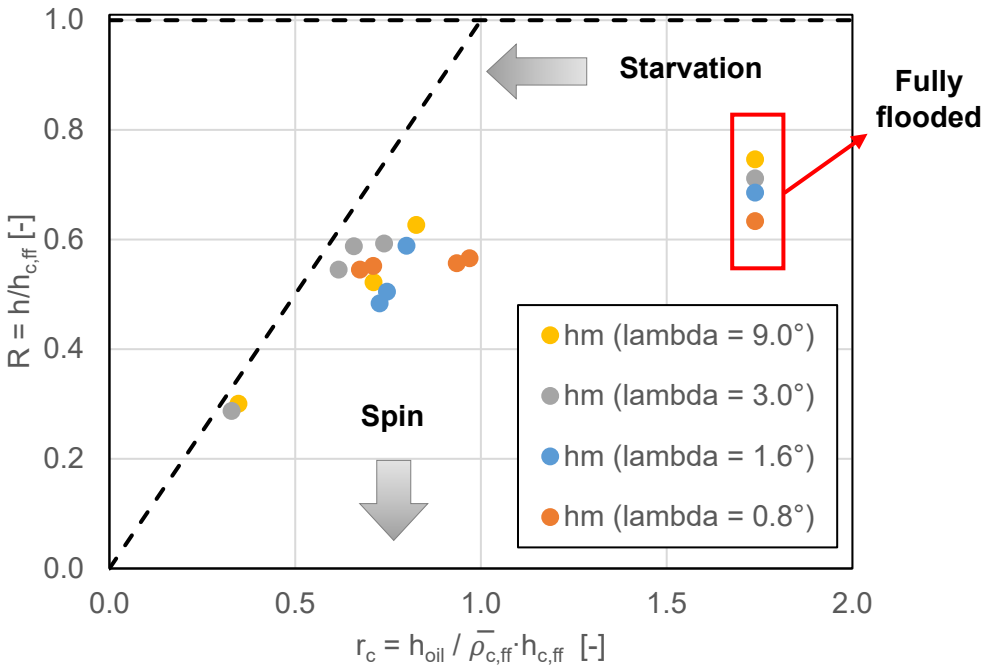

Figure 4.11. Dimensionless critical minimum ($R_{m,-}$) film thickness variation with respect to the dimensionless oil supply (r_c) for different spin velocities (u_e = 0.5 m/s, w = 400 N, T = 30°C, R_x = R_y = 50 mm).

4.5. Influence of spinning on EHD elliptical contacts

The previous sections focused on circular-shaped spinning contacts and explored how the film thickness distribution evolved under fully flooded and starved lubrication conditions. In this section, the study is extended to elliptical contacts, both slender ($k < 1$) and wide ($k > 1$), and analyzes how the shape of the contact affects the film thickness distribution under similar lubrication conditions.

4.5.1. Fully flooded lubrication conditions

In order to study the influence of the contact's ellipticity under fully flooded conditions, the operating conditions from Table 4.3 are taken up. The entrainment speed and normal load are kept constant, together with the lubricant properties and temperature. The ellipticity ratio, defined by:

$$k = \frac{b}{a} = 1.0339 \left(\frac{R_y}{R_x}\right)^{0.636} \tag{4.11}$$

is varied between 0.75 and 4. Two conditions are explored. In the first case, the dimensionless numbers L and M are fixed at the values of 6.6 and 272.3, respectively, by setting the curvature radius in the x-direction R_x constant and only varying that in the y-direction R_y (see Equations (4.1a) and (4.1b)); the Hertzian pressure p_H thus varies for each contact geometry. The second

condition keeps the Hertzian pressure p_H constant (p_H = 0.71 GPa) and varies the ellipticity of the contact by changing both curvature radii R_x and R_y; therefore, L and M vary for each contact geometry. The set of operating conditions examined is summarized in Table 4.6.

Parameter [Unit]	Constant numbers L, M	Constant pressure
R_x [mm]	80	35 - 97
R_y [mm]	48 - 671	80 - 241
k [-]	0.75 - 4	1 - 3.5
u_e [m/s]	2	2
Ω [rad/s]	0 - 4000	0 - 4000
B	0 - 3.7	0 - 3.7
w [N]	800	800
P_H [GPa]	0.39 - 0.84	0.71
a [µm]	494 - 794	393 - 735
b [µm]	571 - 1983	138 -735
T [°C]	30	30
μ_0 [mPas]	11.4	11.4
α^* [GPa^{-1}]	22.1	22.1
L [-]	6.6	6.3 - 8.1
M [-]	272.3	214.2 - 754.2

Table 4.6. Operating conditions of the contact.

Figure 4.12 shows the variation of the film thickness reduction coefficient C_{sp} as a function of the spin-to-roll ratio B for the two group of contacts defined in Table 4.6. The group of curves characterized by the constant numbers L and M is traced in red while the group of curves defined by a constant Hertzian pressure is traced in blue. The curve for k = 1 relates to both cases and is traced in green color; it can be directly fitted to the solution given in Figure 4.4 for circular-shaped contacts.

The curves show an increase in the reduction rate of $h_{m,-}$ (i.e., higher C_{sp} values) with spinning. Moreover, these trends are not linear, meaning that the effect of spinning on the film thickness is accentuated the greater the value of the spin-to-roll ratio. Taking the k = 1 curve as a reference, the curves relative to slender elliptical contacts ($k < 1$) lead to smaller film thickness reduction coefficients C_{sp} for similar B ratios. Conversely, the curves associated to wide elliptical contacts ($k > 1$) lead to greater C_{sp} values for similar B ratios. In addition to it, for each group of curves plotted, the reduction rate of $h_{m,-}$ becomes more important with ellipticity for any given B value. The set of curves confirm that the experimental reduction coefficients calculated by Taniguchi *et al.* [17] cannot be fitted to the analytical solution from Figure 4.4 accurately, as they correspond to wide elliptical contact geometries. At the same time, it evidences the influence of the contact's geometry on the impact of spinning. Indeed, in the case of slender elliptical contacts, the influence of spinning is reduced compared to circular or wide elliptical contacts. In fact, the greater the ellipticity of the contact (b greater than a), the

more important the influence of spinning. As the contact becomes larger in the y-direction, relative to the x-direction, the velocity variation along this line also becomes more significant, thus achieving low local velocities (and hence low local film thicknesses) in its outer region. In slender elliptical contacts, however, issues concerning film thickness thinning associated to the particular contact's geometry have to be considered [130].

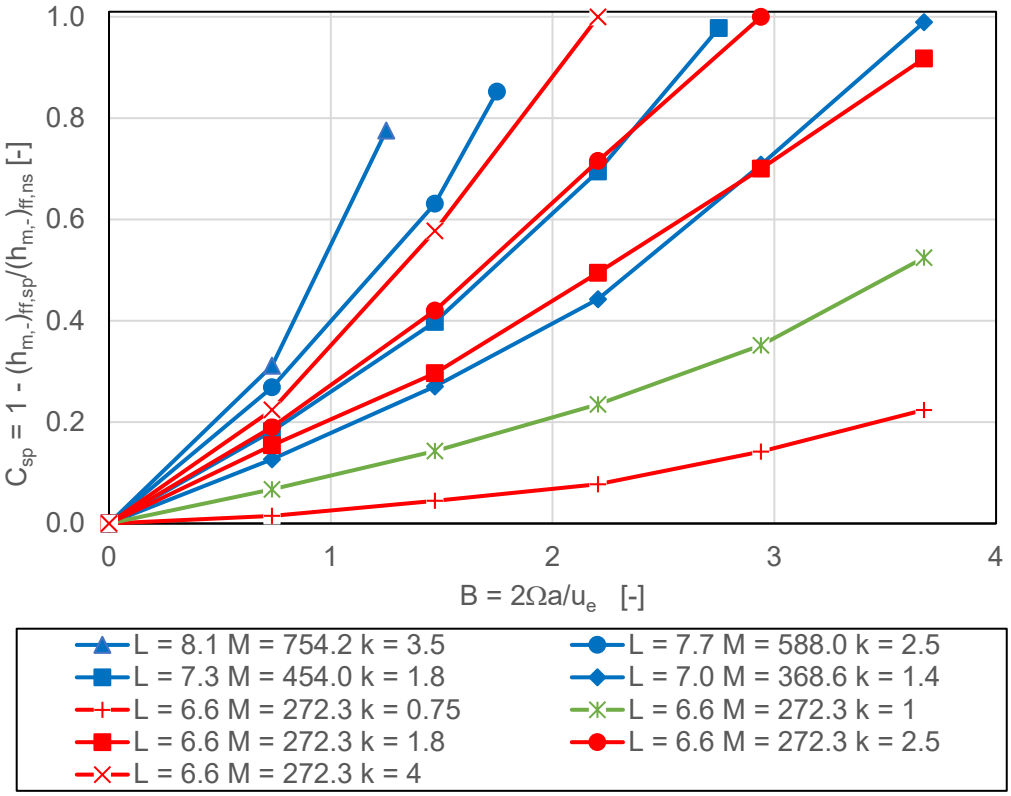

Figure 4.12. Effect of the spin-to-roll ratio B upon the critical minimum film thickness for different ellipticity ratios k, geometric and operating conditions (Table 4.6).

Consider the pair of curves (L = 6.6, M = 272.3, k = 2.5) and (L = 7.3, M = 454.0, k = 1.8), traced in Figure 4.12. Both curves share a similar behavior with B in spite of being defined by different L, M and k parameters. To simplify the analysis, the effect of L on the reduction rate C_{sp} is neglected, as the two L numbers highlighted are similar. For these two curves, the M and k pairs display opposite trends, which indicates that the effects of a high M number are compensated by a low k ratio, and vice versa. Taking into account Equation (4.1b), high M numbers might be induced by high normal loads, low entrainment speeds and/or low curvature radii in the x-direction. As indicated in Figure 4.3, high M numbers define contacts that are more Hertzian-like in nature, whose film thickness distribution is more sensitive to spinning. However, at the same time, a low k ratio implies that the size of the contact in the y-direction is smaller compared to that in the x-direction. Thus, the effect of spinning on $h_{m,-}$ is reduced. In addition, if low C values are associated to high M numbers, in order to define low ellipticity ratios, equally low R_y values are necessary (Equation 4.11). Conversely, the same analysis can be conducted for low M numbers paired with high k ratios: low M numbers (low normal

loads, high entrainment speeds and/or high curvature radii in the x-direction) may generate thicker film thicknesses. Nevertheless, a high ellipticity leads to a high reduction rate of $h_{m,-}$, which requires high R_y values, relative to R_x. A second example that corroborates this behavior is found in the pair of curves (L = 6.6, M = 272.3, k = 1.8) and (L = 7.0, M = 368.6, k = 1.4).

An analytical formula for predicting the C_{sp} factor of elliptical contacts can be built by taking the B-dependent expression of C_{sp} (Equation (4.4)) for circular contacts and multiplying it by a k and M-dependent factor C_{el} that alters the slope of the original curve. The expression of the coefficient C_{el} reads:

$$C_{el} = 1 + \frac{k^2 - 1}{k} \cdot 0.0137M^{0.72} \tag{4.12}$$

This expression corresponds to the best fit associated to the set of points in Figure 4.12. Figure 4.13 compares the film thickness reduction ratios determined from the simulations (y-axis) against the same values determined analytically by the product $C_{sp} \times C_{el}$ (x-axis), from Equation (4.4) and (4.12). The black line indicates a perfect correlation between both values. The red points correspond to the group of curves with constant L and M numbers, the blue points correspond to the group of curves with constant Hertzian pressure and the green points corresponds to the k = 1 curve.

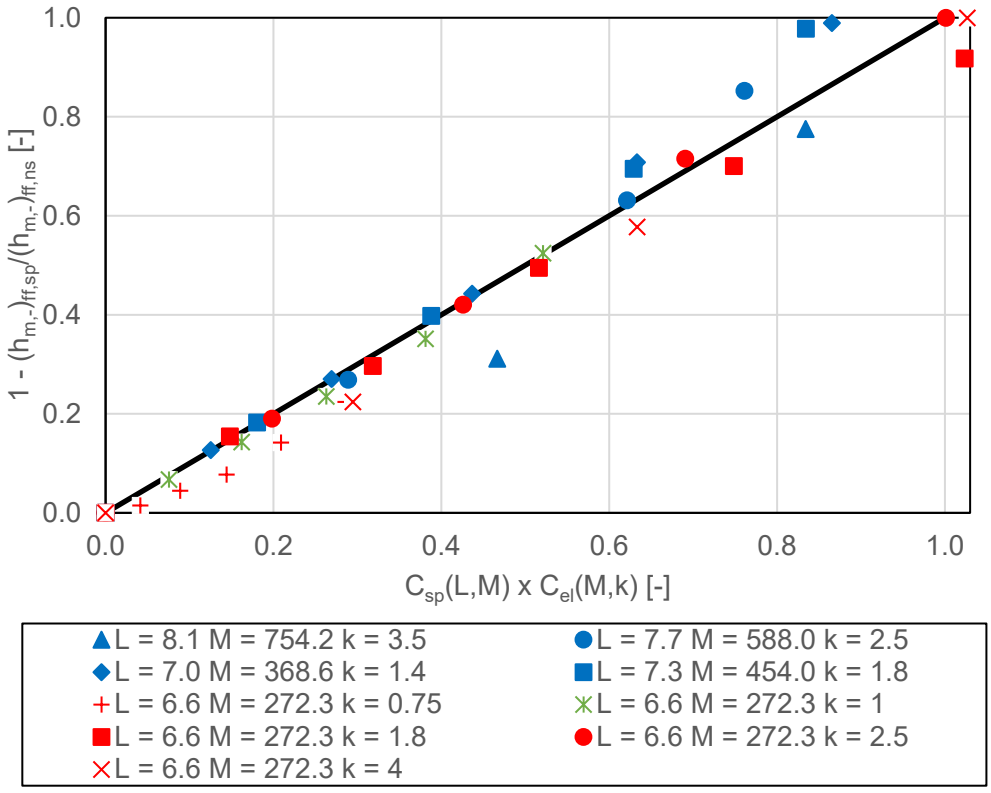

Figure 4.13. Film thickness reduction ratios from the simulations (y-axis) against the same reduction ratios calculated analytically as $C_{sp} \times C_{el}$ (x-axis). The black line indicates a perfect correlation between both values.

The maximum deviation achieved is 15.5% and corresponds to the (k = 3.5 M = 754.2) case, which is highly sensitive to spinning. These conditions may be related to high normal loads, low entrainment speeds and/or low curvature radii (see Equation (4.1b). Likewise, high deviations might also be achieved for high spin-to-roll conditions, for which the critical film thickness $h_{m,-}$ is almost completely reduced ($C_{sp} \times C_{el} \approx 1$).

Table 4.7 selects three contacting cases from [17] and compares their corresponding C_{sp} reduction rates (noted "$_{exp}$") to those estimated from the analytical formulae from Taniguchi *et al.* [17] (subscript "$_{Tan}$"), Hamrock and Dowson [19] (subscript "$_{HD}$") and the analytical expression presented in this study (subscript "$_{anal}$"), integrating the coefficient C_{el} described in Equation (4.12).

	Case A	Case D	Case E
u_e [m/s]	14.5	14.5	14.5
w [N]	1100	500	500
p_H [GPa]	1.01	0.68	0.90
a [mm]	0.33	0.30	0.21
R_x [mm]	23.2	32.2	16.1
k [-]	3.2	2.5	4.1
Ω [rad/s]	2500	1000	2500
L [-]	11.7	10.8	12.8
M [-]	283.5	85.6	202.8

	Case A	Case D	Case E
$(C_{sp})_{exp}$ [-]	0.120	0.030	0.085
$(C_{sp})_{Tan}$ [-]	0.120	0.034	0.081
$(C_{sp})_{anal}$ [-]	0.119	0.018	0.099
$(C_{sp})_{HD}$ [-]	0.082	0.033	0.082

Table 4.7. Operating conditions for three contact cases extracted from [17] (left) and comparison between experimental C_{sp} values to three analytical models: Taniguchi *et al.* [17] ("$_{Tan}$"), Hamrock and Dowson [19] ("$_{HD}$") and the present study ("$_{anal}$").

The results from the present analytical model show a good approximation to the experimental C_{sp} values, with a maximum deviation found for Case D. The L dimensionless number being very similar for the three selected cases, the main difference between them lies in the M dimensionless number and the ellipticity k. Although close ellipticity ratio values to that of Case D have been included in this study, its M number is outside the range of values represented in Figure 4.12, used in defining the analytical expression. Therefore, greater variations might be expected for these conditions. Furthermore, the Newtonian and isothermal behavior of the lubricant flow initially assumed might not be accurate for these operating conditions and other mechanisms or factors not included in the model might have a greater influence on the film thickness.

Some considerations have to be made regarding the different approaches compared. While the expressions from both Hamrock and Dowson [19] and Taniguchi *et al.* [17] are very similar in how they tackle the ellipticity of the contact, they differ in how they model spinning. Hamrock and Dowson's expression encompasses the lubricant and material properties of the contact through their dimensionless spinning parameter. On the other hand, the solution from

Taniguchi *et al.* omits the influence of the lubricant or other effects and focuses on the load. However, their dimensionless spinning parameter considers the velocity and the geometry of the equivalent solid (through R_x). All these aspects are indirectly included in the present model by dimensioning the spin rotational velocity through the contact radius a. Furthermore, the influence of the geometry, the entrainment velocity and the load, among others, is explicitly included by the number M. In addition to it, the expression is applicable to both wide and slender configurations, unlike the models from the literature.

4.5.2. Starved lubrication conditions

The analysis regarding the influence of starvation on the film thickness distribution of spinning elliptical contacts is carried out through the study of two specific elliptical configurations from Table 4.6: k = 0.75 (slender) and k = 1.8 (wide). The operating conditions of the study are summarized in Table 4.8.

Parameter [Unit]	**k = 0.75**	**k = 1.8**
R_x [mm]	80	80
R_y [mm]	48.3	191.3
u_e [m/s]	2	2
Ω [rad/s]	0 - 4000	0 - 4000
B	0 - 3.7	0 - 3.7
w [N]	800	800
P_H [GPa]	0.84	0.54
T [°C]	30	30
μ_0 [mPas]	11.4	11.4
α^* [GPa^{-1}]	22.1	22.1
L [-]	6.6	6.6
M [-]	272.3	272.3

Table 4.8. Operating conditions of the contact.

Figure 4.14 represents the variation of h_{max} and $h_{m,-}$ as a function of the lubricant supply h_{oil} for the aforementioned elliptical contacts: slender (above) and wide (below). For each contact geometry and oil amount, four spin rotational velocities are simulated (Ω = 0, 1000, 2500 and 4000 rad/s). The representative film thickness values plotted are expressed in the dimensionless form R (Equation (4.6)) and the lubricant supply as r_c (Equation (4.7)). The asymptotes $R_c = 1$ (for $r_c \geq 1$) and $R_c = r_c$ (for $r_c \leq 1$), delimiting the behavior of the fully flooded and starved contact [44], respectively, are traced as dashed lines. The predicted behavior of h_{max} and $h_{m,-}$ for no-spin conditions, according to Chevalier's model [44] and its extension to elliptical contacts [45], can only be represented for the wide elliptical contact. Their calculations do not consider slender configurations nor the estimation of the minimum film thickness; they only hold for the central film thickness of wide elliptical contacts.

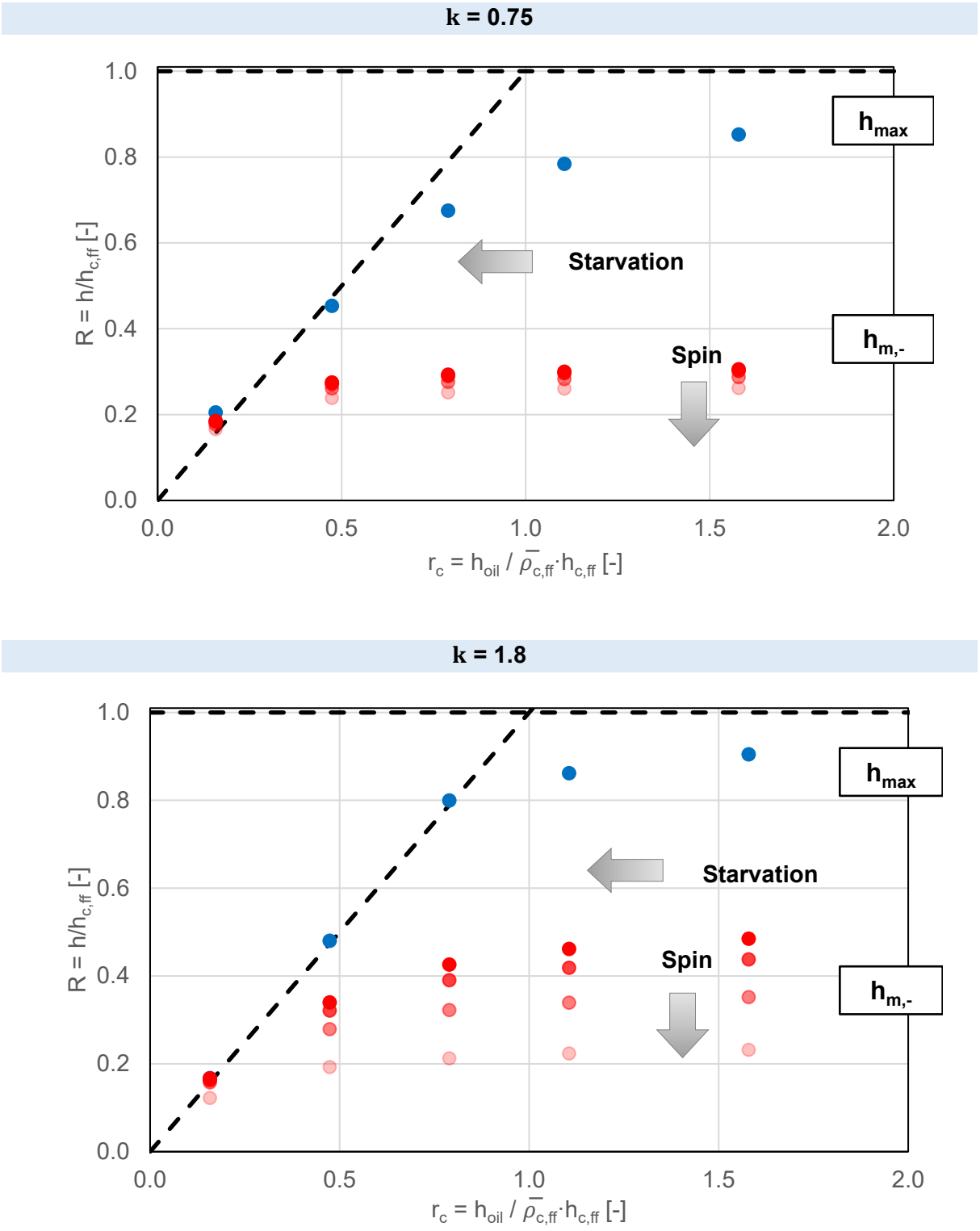

Figure 4.14. Dimensionless maximum (R_{max}) and critical minimum ($R_{m,-}$) film thickness variations with respect to the dimensionless oil supply (r_c) for different spin velocities (u_e = 2 m/s, w = 800 N, T = 30°C, R_x = 80 mm) and to ellipticities: k = 0.75 (above) and k = 1.8 (below).

Figure 4.14 reveals that the conclusions previously extracted for starved and spinning circular contacts (Figure 4.5) still apply to elliptical geometries, both slender and wide. The maximum and minimum film thicknesses still decrease asymptotically with the oil supply for the various spin velocities considered. When fully flooded, the film thickness values remain constant with the amount of lubricant. By limiting the amount of lubricant upstream of the contact, the local maximum film thickness value in the contact is changed according to the asymptote defined by Chevalier [44]. A similar trend is observed for the critical minimum film thickness. As discussed above, while the local maximum does not experience any noticeable variation with spinning, the critical minimum does change. As was reflected in Figure 4.12, this variation is more important for the wide elliptical contact than for the slender one. In fact, for the slender elliptical contact, the difference of $h_{m,-}$ between the no-spin condition and the maximum spin velocity represented (Ω = 4000 rad/s), considering fully flooded conditions, is only 3%. In the case of the wide elliptical contact, this difference increases to 25%. However, the variations that arise due to spinning are reduced by limiting the oil supply, as the trends tend to collapse following the previously stated asymptote.

The comparison between the sets of curves from the slender and wide elliptical contacts also reflects the difference in side flow resistance from the contact. This is shown in the transition between the fully flooded and starved domains, which extends over a wider range in the slender geometry. In Chevalier and Damien's model this aspect is indicated by the dimensionless parameter γ, which also depends on the dimensionless numbers L and M. For the operating conditions listed in Table 4.6, the wide elliptical contact has a resistance value $\gamma \approx 5.1$, whereas for the circular contact (see Table 4.3) the value is 3.5; the literature review does not offer any resource to calculate the γ value for the slender case. With a higher resistance to the side flow, associated to contacts with high M and low L numbers and/or high ellipticity ratios, more lubricant flows into the contact area, which becomes more robust to variations of the oil supply. This phenomenon is related to the fact that (a) the pressure gradient in the x-direction becomes greater than that in the y-direction, and (b) the distance travelled by the lubricant to be ejected from the track is higher for wide elliptical contacts than circular (or slender elliptical) ones. In order to define a more realistic model, adaptable to any elliptic contact geometry and operating conditions, the coefficient C_{st} describing the influence of starvation on the film thickness should incorporate γ. Nevertheless, this area remains open for future research.

Figure 4.15 shows different sets of transversal film thickness profiles for different ellipticity ratios (k = 0.75, 1, 1.8) and lubrication conditions whereas spinning is kept identical (Ω = 4000 rad/s). The profiles from slender and wide elliptical contacts have been extracted from Figure 4.11, whereas the profiles from the circular contact have been taken from Figure 4.5. The film thickness values are expressed in the dimensionless form R (Equation (4.6)) and the y-coordinate as $Y = y/b$.

The three sets of film thickness profiles evidence the influence of the contact's ellipticity on the film thickness loss when exposed to starvation at high spinning rotational velocities. Regarding the slender elliptical contact, the displacement of h_{max} to the high velocity region of the contact area manifests the dissymmetry of the profiles due to spinning. However, at the same time, this displacement is not as pronounced as in the case of the wide elliptical contact (for a much lower value of k, the contact is expected to be close to symmetrical). The difference between

both local minima at the side lobes is equally minor, about 5% in the fully flooded case, when compared to the circular (47%) and wide elliptical (69%) contacts for the same oil amount. The main film thickness variation with starvation occurs for h_{max} (around 70% for the cases represented); differences in $h_{m,-}$ only start to become noticeable for high degrees of starvation. The opposite effect is observed in the wide elliptical contact. It can be seen that the displacement of h_{max} to the side lobe is more important and the difference between the two local minima is significantly higher (69%). Moreover, the effect of starvation is more notable at the high velocity lobe than in the slender elliptical case, even at mild degrees of starvation, experiencing a total decrease of 63% for the cases represented.

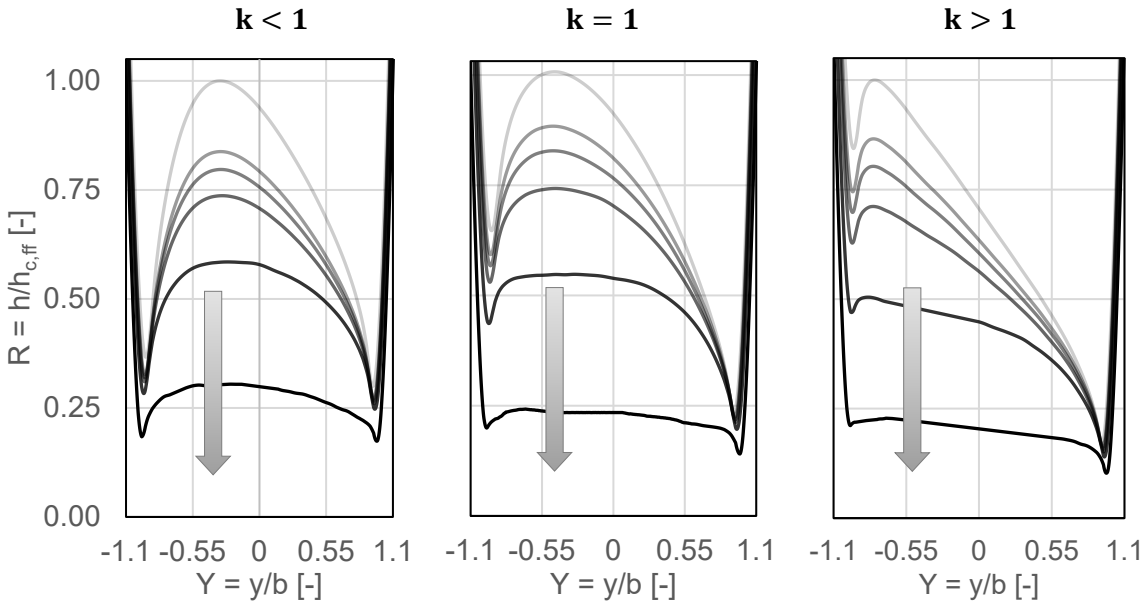

Figure 4.15. Transversal film thickness profiles for different ellipticity ratios (k = 0.75, 1, 1.8) and identical spinning and lubrication conditions (u_e = 2 m/s, w = 800 N, T = 30°C, R_x = 80 mm, Ω = 4000 rad/s). Film thickness values extracted from Figures 4.5 and 4.11. An arrow illustrates the direction of increasing degrees of starvation.

Compared to the two elliptical contacts illustrated, the circular contact represents an intermediate situation. While the shape of the profiles stands in between the two cases, in dimensionless terms, similar behaviors for $h_{m,-}$ and h_{max} as those observed in the wide elliptical contact are encountered. The description for this specific set of curves has been reported before in relation to Case 4 (Figure 4.6).

To sum up, the resulting analytical expression for the minimum film thickness $h_{m,-}$, regardless of the geometry, spinning or lubrication conditions, is:

$$\left(h_{m,-}\right)_{st,sp} = \left(h_{m,-}\right)_{ff,ns} \cdot \left(1 - C_{sp} \cdot C_{el}\right) \cdot \left(1 - C_{st}\right) \tag{4.13}$$

where the values of C_{sp}, C_{st} and C_{el} are determined according to Equations (4.4), (4.9) and (4.12), respectively.

To validate the expression, the contacts from images a to i (Figure 4.8) are taken up and their $h_{m,-}$ values are estimated using Equation (4.13) and are compared to the corresponding experimental film thickness measurements. Contrary to the prediction previously done in Table 4.5, the new analysis considers the actual shape of the contact area and integrates the ellipticity ratio of the contact into the calculation. The updated operating conditions for the selection of interferograms as well as the experimental (noted as "Experim.") and analytical (noted as "Analytical") $h_{m,-}$ values are reported in Table 4.9. For the application of Equation (4.13), and following the same criteria as in Table 4.5, the $h_{m,-}$ measurement from Image f (λ = 9°) is taken as a reference (fully flooded/no-spin) value for the prediction. Thus, its spin-to-roll ratio B is assumed 0 for the calculations. However, the real spinning conditions are still indicated in parenthesis.

	Ω [rad/s]	B [-]	h_{oil} [nm]	k [-]	$h_{m,-}$ [nm]	
					Experim.	Analytical
Image a	628	1.580	inf	1.2	468.0	541.2
Image b	628	1.580	669	1.1	417.8	399.5
Image c	628	1.580	591	1.1	411.2	389.0
Image d	628	1.580	573	1.1	407.5	396.4
Image e	628	1.580	508	1.1	402.6	375.3
Image f	0 (62)	0 (0.156)	inf	1.0	557.4	557.4
Image g	0 (62)	0 (0.156)	573	1.0	468.0	429.0
Image h	0 (62)	0 (0.156)	464	1.0	390.0	406.8
Image i	0 (62)	0 (0.156)	300	1.0	224.4	353.9

Table 4.9. Updated operating conditions for the images illustrated in Figure 4.8 and comparison of $h_{m,-}$ estimated by: experiments ("Experim.") and the numerical model described in Equation (4.12) ("Analytical").

The analytical film thickness values for images f to i have not changed with respect to those from Table 4.5, as they correspond to circular contact geometries. On the other hand, the contact areas represented in images a to e are characterized by ellipticity ratios between 1.1 and 1.2 and therefore their film thickness predictions have been recalculated. With the exception of the fully flooded case (image a), the predictions show a better approximation to the experimental film thickness measurements than the previously calculated values, in which the ellipticity was not taken into account. For images a to e, the relative error lies below 15.6%.

4.6. Conclusions

In this chapter, the experimental procedure and numerical scheme previously introduced have been applied to evaluate the individual and combined effects of starvation and spinning on the film thickness distribution in EHD large-size contacts. As a result of the current lubrication

trends and common operating conditions of the roller-end/flange contact, the focus is set on quantifying the influence of both conditions on the critical minimum film thickness, that is, the local minimum in the low velocity region of the contact. For this purpose, a series of simulations combining variable operating conditions (entrainment speeds, normal loads, spinning motion), lubrication conditions (from fully flooded to highly starved conditions) and geometries (circular and elliptical contacts) have been performed. At the same time, several assumptions have been made that limit the applicability of the present work, namely the Newtonian behavior of the lubricant and the isothermal conditions of the contacts. The numerical analysis performed has been supported by experimental film thickness measurements obtained with Tribogyr for the specific operating conditions investigated, as well as other measurements extracted from previous studies.

It has been observed that spinning affects the behavior of the lubricant supply at the contact's inlet. Indeed, the variation of the local velocity along the transverse direction to the main flow induces changes on the rate at which lubricant enters the contact. Despite of it, the maximum film thickness achieved in the contact area does not vary significantly.

The effects of starvation add up to those of spinning. Previous studies evidence that spinning induces an asymmetric film thickness profile, producing a local maximum and minimum at each side of the contact area. Starvation reduces the overall film thickness of the whole contact area. When spin also acts on the contact, the film thickness of the local minimum in the high velocity region of the contact decreases faster than that of the opposite local minimum, in the low velocity region. Therefore, with increasing degree of starvation, the film thickness profile of the spinning contact becomes more uniform, approaching a Hertzian profile. The dissymmetry originally introduced through spinning is attenuated.

Finally, the set of results accomplished through this study has allowed to write a predictive formula for estimating the critical minimum film thickness under specific operating (spinning) and lubrication conditions (degree of starvation) and for a given contact geometry (i.e., ellipticity ratio). The prediction is built on the minimum film thickness value of the corresponding fully flooded no-spinning contact. This equation decouples the effects on the film thickness profile due to spinning to those induced by starvation or the contact's ellipticity.

General conclusions

This thesis was devoted to the study of the roller-end/flange contact, focusing on the influence of the lubricant supply of the contact and its effects on the film thickness profile when combined with the spinning motion of the mating elements. For this purpose, a numerical-experimental strategy was chosen.

Chapter I provides a general introduction to the subject. After addressing the particular kinematics of the contact region, the chapter gathers the main bibliography on the roller-end/flange contact, emphasizing on the aspects of the contact previously investigated at LaMCoS (friction coefficient, thermal dissipation and contact geometry). A lack of information on starved spinning contacts is evidenced following a brief literature review on the subject of starvation. It was then concluded that, in order to reflect the actual conditions of the roller-end/flange contact and represent the various phenomena involved more accurately, further research in this area is needed.

Chapter II is dedicated to the experimental tools of the study. The chapter discusses the most important issues encountered in current experimental techniques to effectively starve a contact and reproduce its results. Moreover, it introduces the two tribometers used in the study, Jerotrib and Tribogyr, and the modifications implemented into them to induce and control starvation on the test ball. These modifications revolve around a roller placed upstream of the ball-disk contact for generating a uniform lubricant film layer to feed it. Two criteria are considered for selecting an appropriate roller: the ratio between the roller-disk and ball-disk contact sizes and the uniformity of the lubricant layer at the outlet of the roller-disk contact. Additionally, some limitations regarding the range of film thicknesses measured are examined, as well as the influence of the shape and the location of the roller-disk contact's inlet meniscus on the quality of the results. A formula for estimating the film thickness of the lubricant layer feeding the ball-disk contact is presented, for which pure rolling conditions are assumed. This value constitutes an input parameter of the numerical model and is essential for defining the starving conditions of the ball-disk contact.

Chapter III is dedicated to the numerical model employed. After briefly introducing the main set of equations for evaluating fully flooded EHD spinning contacts, the chapter develops a new strategy for computing starved lubrication conditions based on the biphasic fluid theory. The new approach defines the content entrapped between the two solids in contact as an equivalent fluid with variable volume fractions of air and lubricant, depending on the local pressure conditions. For each fluid regime considered (vapor, mixture or liquid), specific expressions to describe the behavior of the equivalent fluid are deduced. Each regime is delimited by a boundary pressure, calculated from the fluid's properties. Altering the amount of lubricant upstream of the contact studied varies these boundary pressure values, thus reflecting a unique degree of starvation. The model was then validated experimentally via the two previously mentioned test rigs: Jerotrib was used to analyze the lubrication aspect of the

model under pure rolling conditions, whereas Tribogyr examined the combination of starvation and spinning for low spin conditions.

In chapter IV the numerical model was used to evaluate the influence of starvation on spinning contacts. For the study, two main hypothesis are considered, namely, that the lubricant is Newtonian in nature and the flow is isothermal. The analysis is carried out in terms of the global minimum film thickness of the contact area, found in the low velocity region of the contact. This global minimum is the result of the varying velocity profile generated by spinning, which induces an asymmetric film thickness profile. A parametric study under fully flooded conditions and variable entrainment speed and normal load shows that the value of this parameter is reduced with spinning and the difference between the two local minima increases. Starvation compensates these differences and leads the contact to behave more Hertzian-like. While starvation on its own reduces the film thickness of the entire contact area, particularly its center region, the inflow of lubricant at the spinning contact's inlet is variable along the normal direction to the main flow. The high velocity region, with the thicker of the two local minima, requires greater quantities of lubricant to sustain the lubricant film and therefore experiences greater film thickness losses the more important the degree of starvation. The analysis was first realized on circular-shaped contacts and was later extended to elliptical cases, both slender and wide. Similar conclusions to the circular contact geometry under spinning and starvation were extracted for the elliptical cases. Furthermore, the global minimum film thickness of slender elliptical contacts proved to be more robust to variations with spinning than its wider counterpart, as a result of the smaller velocity gradients in the contact area. However, no preliminary validation of the starved no-spin results could be performed due to the lack of predictive models for these conditions in the literature. The findings concerning the circular geometries were able to be verified by experimental measures from Tribogyr, combining different spinning angles and degrees of starvation, for two entrainment speeds. Finally, the film thickness variation of the global minimum was quantified through a predictive formula that decouples the effects of spinning, starvation and the contact's ellipticity.

In conclusion, spinning and starvation are conditions inherent to the roller-end/flange contact, the consequences of which are cumulative and can affect the behavior of the contact, and in consequence the bearing. When both parameters act in sufficiently large proportions, the amount of lubricant entrapped within the contact area might not be enough to sustain the contact safely in the long term and the surface, the mating elements or the bearing itself may fail. The results presented in this thesis can help bearing manufactures understand the phenomena involved during the operation of a bearing with a limited lubricant supply and provide a tool to predict the critical film thickness encountered in the contacts for given operating conditions, thus increasing awareness of the demanding contact conditions of the system.

Recommendations for future work

The following points document several perspectives for future lines of research:

Experimental film thickness measures of starved and spinning elliptical contacts. This work has presented experimental film thickness measures of circular contacts working under spinning, starvation and a combination of both parameters. This data has been used to validate the results obtained from simulations as well as the proposed prediction formulae for the critical film thickness in the contact area. However, a lack of experimental film thickness measurements concerning elliptical contacts operating under starvation or spinning and starvation at the same time was evidenced. An extension of the experimental work presented herein in this direction could therefore result advantageous.

Furthermore, additional experimental operating conditions could be envisaged too. In this sense, the data shown in this work always assumed pure rolling conditions, which allowed for an accurate estimation of the contact's inlet oil supply. This might not always be the case in actual roller bearings. Thus, a new experimental campaign could be planned in the future to observe how sliding conditions might affect the inflow of lubricant into the contact area under starvation. For this purpose, modifications on the oil supply evaluation formula should be tackled, as the slide-to-roll ratio of the rolling elements ceases to be zero.

Surface roughness. Another assumption considered throughout this study was that the surfaces of the elements in contact were mirror polished. The actual quality of the bearing components' surfaces are not perfect and present small defects and crevices, some of them resulting from the polishing of the elements prior to being mounted. Depending on the orientation of these with respect to the direction and movement of the rotating element, they could interfere with how lubricant flows inside the contact area and is evacuated from it, opposing or aiding it. The next step for studying the roller-end/flange contact should hence include considerations to the real state of the surfaces in contact. Common surface finishes applied by bearing manufacturers to rolling-element bearing components should be considered. Moreover, alternative techniques to the one presented in this work to experimentally evaluate film thicknesses should be explored, as optical interferometry might not be a reliable way to study them anymore.

Successive over-rollings. In this study, the roller-end/flange contact was modelled as a ball-on-plane contact with a fixed and stationary lubricant supply at its inlet. As has been indicated, the oil supply of a rolling element is directly influenced by the operating conditions of the preceding one. In a rolling-element bearing, the roller-end/flange contact generated by a rolling element does not operate in an isolated manner, but interacts with the rest of rotating elements. In fact, a high spinning motion of the surfaces might redirect part of the exiting flow from the contact back to its inlet, limiting the amount of oil fed to the next contact. Thus, its oil supply

might not be static and change over time. Similarly, predictive models on lubricant loss might not be accurate for not taking into consideration the spinning component of the kinematic field. In an age in which manufacturers optimize the amount of lubricant included in a bearing, predicting when the bearing (through its different lubricated contacts) has reached its limit and requires oil replenishment becomes crucial. The numerical model should therefore reflect, in a simple manner, the number of additional contacts integrated to the original one being studied and its influence on the lubricating conditions. Experimentally, several (two or more) rolling elements with identical geometry to the one being studies, should be introduced upstream of it. However, given the space limitations in the current test rig configuration, this aspect might be challenging to integrate.

Annex A:

Dimensionless equations

This annex transcribes the set of equations first introduced in Chapter III and later used in the present study into their dimensionless formulation. For this purpose, the following parameters are defined:

$$X = \frac{x}{a} \tag{A.1a}$$

$$Y = \frac{y}{b} \tag{A.1b}$$

$$P = \frac{p}{p_h} \tag{A.1c}$$

$$H = \frac{hR_x}{a^2} \tag{A.1d}$$

$$\bar{\rho} = \frac{\rho}{\rho_0} \tag{A1.e}$$

$$\bar{\mu} = \frac{\mu}{\mu_0} \tag{A1.f}$$

$$\overline{T} = \frac{T}{T_0} \tag{A1.g}$$

with x and y the space coordinates, a and b the contact radii in the x and y-directions, p the pressure, p_h the Hertzian pressure, h the gap height and R_x the curvature radius in the x-direction. Regarding the lubricant, ρ is the density, μ is its viscosity and ρ_0 and μ_0 are the density and the viscosity at ambient conditions ($p = P_{atm}$). T is temperature of the lubricant at the point studied, while T_0 is the lubricant temperature at the contact inlet.

The dimensionless equations are then written:

- Reynolds equation:

$$\frac{\partial}{\partial X}\left(\bar{\varepsilon}\frac{\partial P}{\partial X}\right) + \frac{\partial}{\partial Y}\left(\bar{\varepsilon}\frac{\partial P}{\partial Y}\right) - U_{mx}\frac{\partial}{\partial X}(\bar{\rho}H) - U_{my}\frac{\partial}{\partial Y}(\bar{\rho}H) = 0 \tag{A.2}$$

where

$$\bar{\varepsilon} = \frac{\bar{\rho}H^3}{\bar{\mu}\bar{\lambda}} \tag{A.3a}$$

$$\bar{\lambda} = \frac{12u_{ref}\mu_0 R_x^2}{a^3 p_H} \tag{A.3b}$$

$$U_{mx} = \frac{u_{mx}}{u_{ref}} \qquad U_{my} = \frac{u_{my}}{u_{ref}} \tag{A.3c}$$

$$u_{ref} = \sqrt{u_{mx}^2 + u_{my}^2} \tag{A.3d}$$

u_{mx} and u_{my} are the mean entrainment velocities in the x and y-directions.

- Film thickness equation:

$$H(X,Y) = H_0 + \frac{X^2}{2} + \frac{Y^2}{2} + \frac{2}{\pi^2}\int_{-\infty}^{+\infty}\int_{-\infty}^{+\infty}\frac{P(X',Y')dX'dY'}{\sqrt{(X-X')^2 + (Y-Y')^2}} \tag{A.4}$$

- Load balance equation:

$$\int_{-\infty}^{+\infty}\int_{-\infty}^{+\infty} P(X,Y)dXdY = \frac{2\pi}{3} \tag{A.5}$$

- Lubricant density (Murnaghan equation of state [96]):

$$\frac{V}{V_0} = \frac{\rho_0}{\rho_f} = \left(1 + \frac{K_0'}{K_0}Pp_h\right)^{-\frac{1}{K_M'}} \tag{A.6}$$

with

$$K_0 = K_{00}e^{-\beta_K \bar{T}T_0} \tag{A.7}$$

and

$$\frac{V_0}{V_R} = \frac{\rho_R}{\rho_0} = 1 + a_v(\bar{T}T_0 - T_R) \tag{A.8}$$

V and ρ_f are the volume and the density of the lubricant at a given pressure and temperature. V_0, ρ_0 and K_0 are the volume, the density and the bulk modulus measured at environmental conditions. K_0' is a constant representing the dependence of K_0 to pressure values close to ambient conditions. K_{00} is the value of K_0 when $T = 0$ K and β_K is the bulk modulus-temperature coefficient. T_R is a reference temperature of the lubricant at ambient pressure, a_v is the volume-temperature constant and V_R is the volume corresponding to the reference temperature T_R.

- Lubricant viscosity (modified Williams-Landel-Ferry (WLF) correlation [97]):

$$\bar{\mu}(P,\bar{T}) = \frac{\mu_G}{\mu_0}\exp\left(\frac{-2.303C_1(\bar{T}T_0 - T_g)F}{C_2 + (\bar{T}T_0 - T_g)F}\right) \tag{A.9}$$

with

$$T_g(P) = T_{g0} + A_1 \ln(1 + A_2 P p_h) \quad \text{(A.10a)}$$

$$F(P) = (1 + b_1 P p_h)^{b_2} \quad \text{(A.10b)}$$

A_1, A_2, b_1, b_2, C_1 and C_2 are constants of the WLF law, μ_G is the viscosity at the glass transition temperature T_g and at a pressure p. T_{g0} is the glass transition temperature at ambient pressure and F is the relative thermal expansion of the free volume.

Annex B:
Film thickness prediction formulae for starved contacts

Throughout this document, several analytical formulae for predicting the central and minimum film thickness of EHD starved contacts have been cited. The expressions referenced here assume isothermal conditions and no spinning kinematics.

As indicated in previous chapters, two groups of prediction formulae are distinguished. The first group encompasses the models from Wedeven *et al.* [32] and Hamrock and Dowson [34]. They focus on the location of the inlet meniscus (S or m, respectively) and determine a critical position (S_f or m^*, respectively) below which the contact can be considered starved.

- **Wedeven *et al.*** [32] expressions (applicable only to circular contacts).

$$\frac{H_c'}{H_{cff}'} = \left(\frac{S}{S_f} \cdot \left(2 - \frac{S}{S_f}\right)\right)^{1/2} \tag{B.1}$$

where

$$S_f = 3.52 \cdot (R_x H_{cff}')^{2/3} \cdot a^{-1/3} \tag{B.2a}$$

$$S = x_i - a \tag{B.2b}$$

a is the contact radius of the circular contact and x_i the position of the inlet meniscus in absolute coordinates. H_c' is the dimensionless central film thickness under starvation and H_{cff}' the value of the same parameter under fully flooded conditions. The contact is said to be starved if $S \geq S_f$.

- **Hamrock and Dowson** [34] expressions (applicable to circular and elliptical contacts).

$$\frac{H_c'}{H_{cff}'} = \left(\frac{m-1}{m^*-1}\right)^{0.29} \tag{B.3a}$$

$$\frac{H_m'}{H_{mff}'} = \left(\frac{m-1}{m^*-1}\right)^{0.25} \tag{B.3b}$$

where

$$m^* = 1 + 3.06\left(\left(\frac{R_x}{b}\right)^2 H_{cff}'\right)^{0.58} \text{ or } m^* = 1 + 3.34\left(\left(\frac{R_x}{b}\right)^2 H_{mff}'\right)^{0.56} \tag{B.4a}$$

$$m = \frac{x_i}{b} \tag{B.4b}$$

b is the contact radius in the main direction of the flow and R_x is the curvature radius in the x-direction. The contact is said to be starved if $m \geq m^*$.

The second, and more recent, group of expressions includes the model from Chevalier [103] for circular starved contacts and its later extension to elliptical contacts by Damiens *et al.* [45]. This model, unlike the previous ones, focus on the amount of lubricant found upstream of the contact. This quantity is indicated as an equivalent film thickness H_{oil} of the lubricant layer.

- **Chevalier** [103] and **Damiens *et al.*** [45] expressions (applicable to circular and elliptical contacts).

$$R_c = \frac{r_c}{\sqrt[\gamma]{1 + r_c^{\gamma}}} \tag{B.5}$$

where

$$R_c = \frac{H_c}{H_{cff}} \tag{B.6a}$$

$$r_c = \frac{H_{oil}}{H_{cff} \cdot \bar{\rho}(p_H)} \tag{B.6b}$$

$\bar{\rho}(p_H)$ is the dimensionless density of the lubricant at the Hertzian pressure p_H. γ is a dimensionless parameter describing the resistance to the sideflow. Its value is dependent on the operating conditions of the contact, expressed by the Moes numbers L and M, as well as the contact's shape, defined by the ellipticity ratio k. The value of γ can be determined through charts drawn with experimental film thickness measures.

References

[1] J.-D. Wheeler, "Non-elliptical point contacts: the torus-on-plane conjunction," PhD Thesis, Institut National des Sciences Appliquées de Lyon, N° d'ordre 2016LYSEI131, 2016.

[2] G. W. Stachowiak and A. W. Batchelor, Engineering Tribology, Amsterdam (The Netherlands): Elsevier Science Publishers B.V., 1993.

[3] R. Gohar, Elastohydrodynamics, London (Great Britain): Imperial College Press, 2001.

[4] W. Habchi, "A full-system finite element approach to elastohydrodynamic lubrication problems: application to ultra-low viscosity fluids," PhD Thesis, Institut National des Sciences Appliquées de Lyon, N° d'ordre 2008-ISAL-0038, 2008.

[5] H. Dormois, "Frottement dans les contacts EHD de grandes dimensions, rôle du pivotement," PhD Thesis (in French), Institut National des Sciences Appliquées de Lyon, N° d'ordre 2008-ISAL-0091, 2008.

[6] H. Dormois, N. Fillot, P. Vergne, G. Dalmaz, M. Querry and E. Ioannides, "First traction results of high spinning large-size circular EHD contacts from a new test rig: Tribogyr," *Tribology Transactions,* vol. 52, no. 2, pp. 171-179, 2009.

[7] T. Doki-Thonon, "Thermal effects in elastohydrodynamic spinning circular," PhD Thesis, Institut National des Sciences Appliquées de Lyon, N° d'ordre 2012ISAL0058, 2012.

[8] T. A. Harris, M. N. Kotzalas and W. K. Yu, "On the causes and effects of roller skewing in cylindrical roller bearings," *Tribology Transactions,* vol. 41, no. 4, pp. 572-578, 1998.

[9] Y. Yang, S. Danyluk and M. Hoeprich, "On the measurement of skew of tapered roller bearings," *Tribology Letters,* vol. 6, pp. 221-223, 1999.

[10] Y. Yang, S. Danyluk and M. Hoeprich, "A study of rolling-element skew measurement in a tapered roller bearing with a specialized capacitance probe," *Transactions of the ASME,* vol. 122, pp. 534-538, 2000.

[11] D. Dowson, C. M. Taylor and H. Xu, "Elastohydrodynamic lubrication of elliptical contacts with spin and rolling," *Proc Instn. Mech. Eng. Part C: Journal of Mechanical Engineering Science,* vol. 205, pp. 165-174, 1991.

[12] P. Yang and J. Cui, "The influence of spinning on the performance of EHL in elliptical contacts," *Proceedings of the IUTAM Symposium on Elastohydrodynamics and Micro-elastohydrodynamics,* pp. 81-92, 2006.

[13] Q. Zou, C. Huang and S. Wen, "Elastohydrodynamic film thickness in elliptical contacts with spinning and rolling," *Transactions of the ASME,* vol. 121, pp. 686-692, 1999.

[14] D. Dowson, C. M. Taylor and H. Xu, "Elastohydrodynamic lubrication of elliptical contacts with pure spin," *Proc Instn Mech Engrs,* vol. 207, pp. 83-92, 1993.

[15] F. Colin, F. Chevalier, J.-P. Chaomleffel, J. de Mul and G. Dalmaz, "Starved elastohydrodynamic lubrication of the rib-roller end contact in tapered roller bearings:

film thickness, traction and moments," *Proceedings of the 24th Leeds-Lyon Symposium on Tribology "Tribology for Energy Conservation", London 4-6 September 1997, Tribology Series,* vol. 34, D. Dowson (Editor), pp. 253-263, Elsevier, Amsterdam, 1998.

[16] X. Liu, S. Li, P. Yang and P. Yang, "On the lubricating mechanism of roller skew in cylindrical roller bearing," *Tribology Transactions,* vol. 56, no. 6, pp. 929-942, 2013.

[17] M. Taniguchi, D. Dowson and C. M. Taylor, "The effect of spin motion upon elastohydrodynamic elliptical contacts," *Proceedings of the 23rd Leeds-Lyon Symposium on Tribology "Elastohydrodynamics - '96 Fundamentals and Applications in Lubrication and Traction", Leeds 10-13 September 1996, Tribology Series,* vol. 32, D. Dowson (Editor), pp. 599-610, Elsevier, Amsterdam, 1997.

[18] B. J. Hamrock and D. Dowson, "Isothermal elastohydrodynamic lubrication of point contacts. Part III -- Fully flooded results," *Trans. ASME J. Lubr. Technology,* vol. 99, no. 2, pp. 264-276, 1977.

[19] B. J. Hamrock and D. Dowson, "Minimum film thickness in elliptical contacts for different regimes of fluid-film lubrication," NASA RP--1342, 1978.

[20] J. L. Tevaarwerk and K. L. Johnson, "The influence of fluid rheology on the performance of traction drives," *Journal of Lubrication Technology,* vol. 101, no. 3, pp. 266-273, 1979.

[21] S. Poon, "Some calculations to asses the effect on the tractive capacity of rolling contact drives," *Proc. I. Mech. Eng.,* vol. 185, pp. 1015-1022, 1970.

[22] O. S. Cretu and R. P. Glovnea, "Traction drive with reduced spin losses," *Journal of Tribology,* vol. 125, pp. 507-512, 2003.

[23] S. Y. Poon and D. J. Haines, "Frictional behavior of lubricated rolling-contact elements," *Proc. Instn. of Mech. Engrs.,* vol. 181, pp. 363-376, 1996-97.

[24] J. L. Tevaarwerk, "A simple thermal correction for large spin traction curves," *Journal of Mechanical Design,* vol. 103, no. 2, pp. 440-445, 1981.

[25] J. Newall and A. Lee, "Measurement and prediction of spin losses in EHL point contacts of the full toroidal variator," *Proceedings of the 30th Leeds-Lyon Symposium on Tribology "Transient Processes in Tribology", Lyon 2-8 September 2003, Tribology Series,* vol. 43, D. Dowson (Editor), pp. 769-779, Elsevier, Amsterdam, 2004.

[26] H. Dormois, N. Fillot, W. Habchi, G. Dalmaz, P. Vergne, G. Morales-Espejel and E. Ionnades, "A numerical study of friction in isothermal EHD rolling-sliding sphere-plane contacts with spinning," *Journal of Tribology,* vol. 132, no. 2, pp. 021501-10, 2010.

[27] X. M. Li, F. Guo, B. Fan and P. Yang, "Influence of spinning on the rolling EHL films," *Tribology International,* vol. 43, no. 11, pp. 2020-2028, 2010.

[28] P. Ehret, D. Dowson and C. Taylor, "Thermal effects in elliptical contacts with spin conditions," *Proceedings of the 25th Leeds-Lyon Symposyum on Tribology "Lubrication at the Frontier: The Role of the Interface and Surface Layers in the Thin Film and Boundary Regime", Lyon 8-11 September 1998, Tribology Series,* vol. 36, D. Dowson (Editor), pp. 685-703, Elsevier, Amsterdam, 1999.

[29] X. Jiang, P. L. Wong and Z. Zhang, "Thermal non-Newtonian EHL contact analysis of rib-roller end contact in tapered roller bearings," *J. Tribol,* vol. 117, no. 4, pp. 646-654, 1995.

[30] Z. Zhang, X. Qiu and Y. Hong, "EHL analysis of rib-roller en contact in tapered roller bearings," *Tribology Transactions,* vol. 31, no. 4, pp. 461-467, 1988.

[31] N. Gadallah and G. Dalmaz, "Hydrodynamic lubrication of the rib-roller end contact of a tapered roller bearing," *J. Tribology,* vol. 106, no. 2, pp. 265-272, 1984.

[32] L. D. Wedeven, D. Evans and A. Cameron, "Optical analysis of ball bearing starvation," NASA TM X-52869, Cleveland, Ohio, 1970.

[33] L. D. Wedeven, D. Evans and A. Cameron, "Optical analysis of ball bearing starvation," *Journal of Lubrication Technology,* vol. 93, no. 3, pp. 349-361, 1971.

[34] B. J. Hamrock and D. Dowson, "Isothermal elastohydrodynamic lubrication of point contacts. IV - Starvation results," *Journal of Lubrication Technology,* vol. 99, no. 1, pp. 15-23, 1977.

[35] A. P. Ranger, C. M. M. Ettles and A. Cameron, "The solution of the point contact elasto-hydrodynamic problem," *Proceedings of the Royal Society of London. Series A, Mathematical and Physical Sciences,* vol. 346, no. 1645, pp. 227-244, 1975.

[36] P. Castle and D. Dowson, "A theoretical analysis of the starved lubrication problem for cylinders on line contact," *Proceedings of the Institution of Mechanical Engineers: Elastohydrodynamic Lubrication Symposium (London),* pp. 131-137, 1972.

[37] A. W. Crook, "The lubrication of rollers II: film thickness with relation to viscosity and speed," *Philosophical Transactions of the Royal Society of London. Series A, Mathematical and Physical Sciences,* vol. 250, no. 981, pp. 387-409, 1958.

[38] W. Lauder, "Hydrodynamic lubrication of proximate cylindrical surfaces of large relative curvature," *Proceedings of the Institution of Mechanical Engineers,* vol. 180, no. 2, pp. 101-112, 1965.

[39] R. J. Boness, "Isoviscous lubrication of rigid cylinders: a modification to classical theory," *Journal of Mechanical Engineering Science,* vol. 8, no. 3, pp. 276-283, 1966.

[40] H. S. Cheng and B. Sternlicht, "A numerical solution for the pressure, temperature, and film thickness between two infinitely long, lubricated rolling and sliding cylinders, under heavy loads," *Journal of Basic Engineering,* vol. 87, no. 3, pp. 695-704, 1965.

[41] D. Dowson and A. V. Whitaker, "A numerical procedure for the solution of the elastichydrodynamic problem of rolling and sliding contacts lubricated by a newtonian fluid," *Proceedings of the Institution of Mechanical Engineers, Conference Proceedings,* vol. 180, no. 2, pp. 57-71, 1965.

[42] H. M. Martin, "Lubrication of gear teeth," *Engineering, London,* vol. 102, pp. 119-121, 1916.

[43] F. K. Orcutt and H. S. Cheng, "Lubrication of rolling-contact instrument bearings," *Proceedings of the gyro-spin axis hydrodynamic bearing Symposium,* vol. 2, pp. 1-25, 1966.

[44] F. Chevalier, A. A. Lubrecht, P. M. E. Cann, F. Colin and G. Dalmaz, "Film thickness in starved EHL point contacts," *Journal of Tribology,* vol. 120, no. 1, pp. 126-133, 1998.

[45] B. Damiens, C. Venner, P. Cann and A. Lubrecht, "Starved lubrication of elliptical EHD contacts," *ASME J. Tribol.,* vol. 126, no. 1, pp. 105-111, 2004.

[46] P. Svoboda, D. Kostal, I. Krupka and M. Hartl, "Experimental study of starved EHL contacts based on thickness of oil layer in the contact inlet," *Tribology International,* vol. 67, pp. 140-145, 2013.

[47] E. Kingsbury, "Cross flow in starved EHD contacts," *ASLE Transactions,* vol. 16, no. 4, pp. 276-280, 1973.

[48] J. Pemberton and A. Cameron, "A mechanism of fluid replenishment in elastohydrodynamic contacts," *Wear,* vol. 37, no. 1, pp. 185-190, 1976.

[49] F. Chevalier, A. A. Lubrecht, P. M. E. Cann, F. Colin and G. Dalmaz, "The evolution of lubricant film defects in the starved regime," *Proceedings of the 24th Leeds-Lyon Symposium on Tribology "Tribology for energy conservation", London 4-6 September 1997, Tribology Series,* vol. 34, D. Dowson (Editor), pp. 233-242, Elsevier, Amsterdam, 1998.

[50] Y. P. Chiu, "An analysis and prediction of lubricant film starvation in rolling contact systems," *Tribology Transactions,* vol. 17, no. 1, pp. 22-35, 1974.

[51] P. M. E. Cann, B. Damiens and A. A. Lubrecht, "The transition between fully flooded and starved regimes in EHL," *Tribology International,* vol. 37, pp. 859-864, 2004.

[52] T. Nogi, H. Shiomi and N. Matsuoka, "Starved elastohydrodynamic lubrication with reflow in elliptic contacts," *ASME Journal of Tribology,* vol. 140, p. 011501, 2018.

[53] T. Nogi, "An analysis of starved EHL point contacts with reflow," *Tribology Online,* vol. 10, no. 1, pp. 64-75, 2015.

[54] T. Nogi, "Film thickness and rolling resistance in starved elastohydrodynamic lubrication of point contacts with reflow," *ASME Journal of Tribology,* vol. 137, no. 4, p. 041502, 2015.

[55] B. J. Hamrock and D. Dowson, Ball bearing lubrication: the elastohydrodynamics of elliptical contacts, New York: Wiley, 1981.

[56] J. J. Coy and E. V. Zaretsky, "Some limitations in applying classical EHD film thickness formulas to a high-speed bearing," *Journal of Tribology,* vol. 103, no. 2, pp. 295-301, 1981.

[57] A. N. Grubin and I. E. Vinogradova, Investigations of the contact of machine components, Moscow: Central Scientific Research Institute for Technology and Mechanical Engineering, 1949.

[58] J. F. Archard and E. W. Cowking, "Elastohydrodynamic lubrication at point contacts," *Proceedings of the Institution of Mechanical Engineers (London),* vol. 180, no. 2, pp. 47-56, 1965.

[59] D. Dowson and G. R. Higgngson, Elastohydrodynamic lubrication: the fundamental of roller and gear lubrication, Oxford (Great Britain): Pergamon Press, Inc., 1966.

[60] H. S. Cheng, "Isothermal elastohydrodynamic theory for the full range of pressure-viscosity coefficient," *Journal of Lubrication Technology,* vol. 94, no. 1, pp. 35-43, 1972.

[61] E. Kingsbury, "Parched elastohydrodynamic lubrication," *ASME Journal of Tribology,* vol. 107, no. 2, pp. 229-232, 1985.

[62] C. R. Singleterry, "Some factors affecting the movement of oil over metal surfaces," *Gyro Spin Axis Hydrodynamic Bearing Symposium,* vol. 2, 1966.

[63] G. Guangteng and H. A. Spikes, "The role of surface tension and disjoining pressure in starved and parched lubrication," *Proceedings of the Institution of Mechanical Engineers, Part J: Journal of Engineering Tribology,* vol. 210, no. 2, pp. 113-124, 1996.

[64] G. Guangteng, P. M. E. Cann and H. A. Spikes, "A study of parched lubrication," *Wear,* vol. 153, no. 1, pp. 91-105, 1992.

[65] S. van der Vegte and C. H. Venner, "Inkjet based drplet on demand lubrication system for EHL contacts," in *6th World Tribology Congress 2017*, Beijing (China), 2017.

[66] W. van der Kruk, S. Smit, T. Segers, X. Li and C. Venner, "Drop-on-demand printing as novel method for oil supply in elastohydrodynamic lubrication," *Tribology Letters,* vol. 67, no. 3, 2019.

[67] B. Derby, "Inkjet printing of functional and structural materials: fluid property requirements, feature stability, and resolution," *Annual Review of Materials Research,* vol. 40, no. 1, pp. 395-414, 2010.

[68] L. Fadel, S. Poirier, S. Vinsonneau, F. Meslingrente and P. Temple-Boyer, "Experimental temperature compensation on drop-on-demand inkjet printing," *Micro and Nanosystems,* vol. 2, no. 2, pp. 137-141, 2010.

[69] D. Kostal, P. Sperka and M. Hartl, "Controlling and measuring starvation severity in EHL contacts," *Engineering Mechanics,* vol. 21, no. 5, pp. 321-328, 2014.

[70] D. Kostal, P. Sperka, P. Svoboda, I. Krupka and M. Hartl, "Influence of lubricant film thickness on elastohydrodynamically lubricated contact starvation," *ASME Journal of Tribology,* vol. 139, no. 5, p. 051503, 2017.

[71] J. Molimard, M. Querry and P. Vergne, "New tools for the experimental study of EHD and limit lubrication," *Proceedings of the 25th Leeds-Lyon Symposium on Tribology "Lubrication at the Frontier", Lyon 8-11 September 1998, Tribology Series,* vol. 36, D. Dowson (Editor), pp. 717-726, Elsevier, Amsterdam, 1999.

[72] J. Molimard and M. V. P. Querry, "Lubricant rheology in real conditions: measurements and confrontation with a ball/disk contact," *Revue de Métallurgie,* vol. 98, no. 2, pp. 141-148, 2002.

[73] J. P. Chaomleffel, G. Dalmaz and P. Vergne, "Experimental results and analytical predictions of EHL film thickness," *33rd Leeds Lyon Symposium on Tribology "Tribology at theInterface", Leeds 2006, Tribology International,* vol. 40, D. Dowson (Editor), pp. 1543-1552, Elsevier, Amsterdam, 2007.

[74] S. N. Ndiaye, "Ultimate behavior of confined fluids under very high pressure and shear stress," PhD Thesis, Institut National des Sciences Appliquées de Lyon, N° d'ordre 2017LYSEI104, 2017.

[75] P. Cusseau, P. Vergne, L. Martinie, D. Philippon, N. Devaux and F. Briand, "Film forming capability of polymer-base oil lubricants in elastohydrodynamic and very thin film regimes," *Tribology Letters,* vol. 67, no. 2, p. 45, 2019.

[76] T. Doki-Thonon, N. Fillot, G. E. Morales-Espejel, D. Philippon, N. Devaux and P. Vergne, "A dual experimental / numerical approach for film thickness analysis in TEHL spinning skewing circular contacts," *Tribology Letters,* vol. 50, no. 1, pp. 115-126, 2013.

[77] J.-D. Wheeler, N. Fillot, D. Philippon, N. Devaux, G. E. Morales-Espejel and P. Vergne, "A numerical and experimental approach of the flange-roller end contact," *International Tribology Conference ITC2015, Japanese Society of Tribologists,* 2015.

[78] M. Hartl, I. Krupka, R. Poliscuk and M. Liska, "An automatic system for real-time evaluation of EHL film thickness and shape based on the colorimetric interferometry," *Tribology Transactions,* vol. 42, no. 2, pp. 303-309, 1999.

[79] M. Hartl, J. Molimard, I. Krupka, P. Vergne, M. Querry, R. Poliscuk and M. Liska, "Thin film lubrication study by colorimetric interferometry," *Proceedings of the 26th Leeds-Lyon Conference "Thinning Films and Tribological Interfaces", Leeds 14-17 September 1999, Tribology Series,* vol. 38, D. Dowson (Editor), pp. 695-704, Elsevier, Amsterdam, 2000.

[80] M. Hartl, I. Krupka, R. Poliscuk, M. M. J. Liska, M. Querry and P. Vergne, "Thin film colorimetric interferometry," *Tribology Transactions,* vol. 44, no. 2, pp. 270-276, 2001.

[81] K. Johnson, Contact Mechanics, 1st ed., Cambridge: Cambridge University Press, 1985.

[82] M. Born and E. Wolf, Principles of Optics: electromagnetic theory of propagation, interference and difraction of light, Cambridge: Cambridge University Press, 1999.

[83] J.-D. Wheeler, J. Molimard, N. Devaux, D. Philippon, D. Fillot, P. Vergne and G. Morales-Espejel, "A generalized differential colorimetric interferometry method: extension to the film thickness measurement of any point contact geometry," *Tribology Transactions,* vol. 61, no. 4, pp. 648-660, 2018.

[84] C. Badulescu, M. Bornert, J.-C. Dupré, S. Equis, M. Grédiac, J. Molimard, P. Picart, R. Rotinat and V. e. a. Valle, "Demulation of spacial carrier images: Performance analysis of several algorithms using a single image," *Experimental Mechanics,* vol. 53, pp. 1357-70, 2013.

[85] G. Nijenbanning, C. H. Venner and H. Moes, "Film thickness in elastohydrodynamically lubricated elliptic contacts," *Wear,* vol. 176, pp. 217-229, 1994.

[86] T. Maruyama and T. Saitoh, "Relationship beween supplied oil flow rates and oil film thickness under starved elastohydrodynamic lubrication," *Lubricants,* vol. 3, pp. 365-380, 2015.

[87] H. Liang, D. Guo and J. Luo, "Experimental investigation of lubrication film starvation of polyalphaolephin oil at high speeds," *Tribology Letters,* vol. 56, no. 3, pp. 491-500, 2014.

[88] H. Liang, D. Guo, L. Ma and J. Luo, "Experimental investigation of centrifugal effects on lubricant replenishment in the starved regime at high speeds," *Tribology Letters,* vol. 59, no. 3, pp. 1-9, 2015.

[89] J. Sugimura, M. Hashimoto and Y. Yamamoto, "Study of elastohydrodynamic contacts with fluorescence microscope," *Proceedings of the 26th Leeds-Lyon Conference "Thinning Films and Tribological Interfaces", Leeds 14-17 September 1999, Tribology Series,* vol. 38, D. Dowson (Editor), pp. 609-617, Elsevier, Amsterdam, 2000.

[90] V. Bruyère, N. Fillot, G. Morales-Espejel and P. Vergne, "A two-phase flow approach for the outlet of lubricated line contacts," *Journal of Tribology,* vol. 134, no. 4, p. 041503, 2012.

[91] W. Habchi, D. Eyheramendy, S. Bair and G. E. Morales-Espejel, "A full-system approach to the elastohydrodynamic line/point contact problem," *ASME Journal of Tribology,* vol. 130, no. 1, pp. 21501-10, 2008.

[92] W. Habchi, D. Eyheramendy, S. Bair, P. Vergne and G. Morales-Espejel, "Thermal elastohydrodynamic lubrication of point contacts using a Newtonian/generalized Newtonianl lubricant," *Tribology Letters,* vol. 30, no. 1, pp. 41-52, 2008.

[93] J.-D. Wheeler, N. Fillot, P. Vergne, D. Philippon and G. E. Morales-Espejel, "On the crucial role of ellipticity on elastohydrodynamic film thickness and friction," *Proceedings of the Institution of Mechanical Engineers, Part J: Journal of Engineering Tribology,* vol. 230, no. 12, pp. 1503-1515, 2016.

[94] O. Reynolds, "On the theory of Lubrication and its Application to Mr. Beauchamps Tower's Experiments, including an Experimental Determination of the Viscosity of Olive Oil," *Phil. Trans.,* vol. 177, pp. 157-234, 1886.

[95] B. Hamrock and D. Dowson, "Isothermal elastohydrodynamic lubrication of point contacts - Part II: Ellipticity parameter results," *ASME J Tribol,* vol. 98, no. 3, pp. 375-383, 1976.

[96] F. D. Murnaghan, "The compressibility of media under extreme pressures," *Proc. Natl. Acad. Sci. USA,* vol. 30, no. 9, pp. 244-247, 1944.

[97] S. Bair, C. Mary, N. Bouscharain and P. Vergne, "An improved Yasutomi correlation for vscosity at high pressure," *Proceedings of the Institution of Mechanical Engineers, Part J: Journal of Engineering Tribology,* vol. 227, no. 9, pp. 1056-1060, 2013.

[98] P. L. Kapitzka, "The lubrication of rollers and spheres," *Zhurn. Tekh. Fiz;,* vol. 25, pp. 747-762, 1955.

[99] B. Jakobsson and L. Floberg, The finite journal bearing considering vaporization, vol. 190, Gothenburg: Chalmers University of Technology, 1957, pp. 1-116.

[100] K.-O. Olsson, Cavitation in dynamically loaded bearings, Gothenburg: Chalmers University of Technology, 1965.

[101] H. G. Elrod and M. Adams, "A computer program for cavitation and starvation problems," *1st Leeds-Lyon Symposium on Cavitation and Related Phenomena in Lubrication,* vol. 103, D. Dowson (Editor), pp. 37-41, Mechanical Engineering Publications Ltd., London, 1974.

[102] H. Elrod, "A cavitation algorithm," *Journal of Lubrication Technology,* vol. 103, no. 3, pp. 350-354, 1981.

[103] F. Chevalier, "Modélisation des conditions d'alimentation dans les contacts élastohydrodynamics ponctuels," PhD Thesis (in French), Institut National des Sciences Appliquées de Lyon, N° d'ordre 96ISAL0124, 1996.

[104] F. Chevalier, A. A. Lubrecht, P. M. E. Cann, F. Colin and G. Dalmaz, "Starvation phenomena in EHL point contacts: influence of inlet flow distribution," *Tribology Series,* vol. 31, pp. 213-223, 1996.

[105] Y. H. Wijnant, "Contact dynamics in the field of elastohydrodynamic lubrication," PhD Thesis, University of Twente, 1998.

[106] G. Popovici, "Effects of lubricant starvation on performance of elasto-hydrodynamically lubricated contacts," PhD Thesis, University of Twente, 2005.

[107] L. Floberg, "Cavitation boundary conditions with regard to the number of streamers and tensile strength of the liquid," *Proceedings of the 1st Leeds-Lyon Symposium on Tribology "Cavitation and related phenomena in lubrication", Leeds September 1974,* D. Dowson (Editor), pp. 31-35, Mechanical Engineering Publications Ltd., London, 1975.

[108] H. Swift, "The stability of lubricating films in journal bearings," *Proceedings of the Institute of Civil Engineering,* vol. 233, pp. 267-288, 1932.

[109] W. Stieber, Das Schwimmlager: Hydrodynamische Theorie, (in German) Berlin (Germany): VDI Verlag, 1933.

[110] G. Bayada, M. Chambat and M. El Alaoui, "Variational formulations and finite element algorithms for cavitation problems," *Journal of Tribology,* vol. 112, no. 2, pp. 398-403, 1990.

[111] G. Bayada, M. Chambat and C. Vázquez, "Characteristics method for the formulation and computation of a free boundary cavitation problem," *Journal of Computational and Applied Mathematics,* vol. 98, no. 2, pp. 191-212, 1998.

[112] C. Gu, X. Meng and Y. Xie, "A universal model for both flooded and starved lubrication regimes and its application in ring-liner system," *Tribology Transactions,* vol. 60, no. 3, pp. 506-515, 2017.

[113] S. Wu, "A penalty formulation and numerical approximation of the Reynolds-Hertz problem of elastohydrodynamic lubrication," *International Journal of Engineering Science,* vol. 24, no. 6, pp. 1001-1013, 1986.

[114] D. Dowson and C. Taylor, "Fundamental aspects of cavitation in bearings," *Proceedings of the 1st Leeds-Lyon Symposium on Tribology "Cavitation and related phenomena in lubrication", Leeds September 1974,* D. Dowson (Editor), pp. 15-25, Mechanical Engineering Publications Ltd., London, 1975.

[115] M. Braun and R. Hendricks, "An experimental investigation of the vaporous/gaseous cavity characteristics of an eccentric journal bearing," *ASLE Transactions,* vol. 27, no. 1, pp. 1-14, 1984.

[116] I. Etsion and L. Ludwig, "Observation of pressure variationin the cavitation region of submerged journal bearings," *Journal of Lubrication Technology,* vol. 104, no. 2, pp. 157-163, 1982.

[117] D. Vijayaraghvan and T. G. Keith, "An efficient, robust, and time accurate numerical scheme applied to a cavitation algorithm," *Journal of Tribology,* vol. 112, no. 1, pp. 44-51, 1990.

[118] M. Fensanghary and M. Khonsari, "A modification of the switch function in the Elrod cavitation algorithm," *Journal of Tribology,* vol. 133, no. 2, p. 024501, 2011.

[119] F. Sahlin, A. Almqvist, L. Larsson and S. Glavatskih, "A cavitation algorithm for arbitrary lubricant compressibility," *Tribology International,* vol. 40, pp. 1294-1300, 2007.

[120] D. van Odyck and C. Venner, "Compressible Stokes flow in thin films," *Journal of Tribology,* vol. 125, pp. 543-551, 2003.

[121] G. Bayada and L. Chupin, "Compressible fluid model for hydrodynamic lubrication cavitation," *Journal of Tribology,* vol. 135, no. 4, pp. 041702-15, 2013.

[122] G. Bayada, "From a compressible fluid model to new mass conserving algorithms," *Tribology International,* vol. 71, pp. 38-49, 2014.

[123] W. H. McAdams, W. K. Wood and R. L. Bryan, "Vaporization inside horizontal tubes: Benzene-oil mixtures," *Trans. Am. Soc. Mech. Eng.,* vol. 64, pp. 193-200, 1942.

[124] A. Kubota, H. Kato and H. Yamaguchi, "A new modeling of cavitation flows: A numerical study of unsteady cavitation on a hydrofoil," *ASME J. Fluid Mech.,* vol. 240, pp. 59-96, 1992.

[125] M. Masjedi and M. M. Khonsari, "On the effect of surface roughness in point-contact EHL: Formulas for film thickness and asperity load," *Tribology International,* vol. 82, no. A, pp. 228-244, 2015.

[126] P. Evans and R. Snidle, "The isothermal elastohydrodynamic lubrication of spheres," *ASME J. Lubr. Technol.,* vol. 103, pp. 547-557, 1981.

[127] R. J. Chittenden, D. Dowson, J. F. Dunn and C. M. Taylor, "A theoretical analysis of the isothermal elastohydrodynamic lubrication of concentrated contacts -- Part 2: General case, with lubricant entrainment along either principal axis of the hertzian contact ellipse or at some intermediate angle," *Proc. R. Soc. London,* vol. A397, pp. 271-294, 1985.

[128] J.-D. Wheeler, P. Vergne, N. Fillot and D. Philippon, "On the relevance of analytical film thickness EHD equations for isothermal point contacts: Qualitative or quantitative predictions?," *Friction,* vol. 4, no. 4, pp. 369-379, 2016.

[129] H. Moes, "Optimum similarity analysis with applications to elastohydrodynamic lubrication," *Wear,* vol. 159, no. 1, pp. 57-66, 1992.

[130] H. P. Evans and R. W. Snidle, "Analysis of elastohydrodynamic lubrication of elliptical contacts with rolling along the major axis," *Proc. Inst. Mech. Eng. Part C: J. Mech. Eng. Sci.,* vol. 197, no. 3, pp. 209-211, 1983.

FOLIO ADMINISTRATIF

THESE DE L'UNIVERSITE DE LYON OPEREE AU SEIN DE L'INSA LYON

NOM : PORRAS VAZQUEZ DATE de SOUTENANCE : 07/12/2020

Prénoms : Alberto

TITRE : Lubricant starvation in elastohydrodynamic large-size spinning contacts

NATURE : Doctorat Numéro d'ordre : 2020LYSEI109

Ecole doctorale : Mécanique, Energétique, Génie Civil, Acoustique

Spécialité : Génie Mécanique

RESUME :

Cette thèse est dédiée à l'étude des contacts pivotants de grandes dimensions situés à l'interface entre l'extrémité du rouleau et le collet de la bague des roulement. L'objectif principal de l'étude est d'évaluer l'influence de la sous-alimentation sur la distribution d'épaisseur de film du contact et d'analyser comment le pivotement pourrait affecter ce mécanisme. En raison de son importance dans la fiabilité et la performance du roulement, l'accent est mis sur l'épaisseur de film minimale locale située dans la région de faible vitesse de la zone de contact. Pour résoudre ce problème, une double approche numérique-expérimentale est proposée.

La distribution de l'épaisseur de film des contacts pivotants est étudiée numériquement à l'aide d'un modèle d'éléments finis préalablement validé par deux bancs d'essai dédiés: Jerotrib et Tribogyr. La simulation de différentes conditions opératoires, cinématiques, géométriques et de lubrification permet d'écrire une expression analytique pour prédire l'épaisseur critique du film précédent. En même temps, de nouvelles techniques pour induire et contrôler expérimentalement la sous-alimentation au contact sont mises en œuvre dans les deux bancs d'essai et leurs résultats sont comparés à ceux de la simulation. Il est démontré que les effets du pivotement et de la sous-alimentation s'additionnent, de sorte que la distribution de l'épaisseur de film du contact pivotant reste asymétrique mais tend à une distribution plus hertzienne, et donc plus mince, lors de la limitation de l'alimentation en huile en amont de l'entrée du contact.

MOTS-CLÉS : Lubrification, élasto-hyrdodynamique, sous-alimentation, pivotement, contact de grande dimension, Tribogyr, épaisseur de film, modélisation, expérimentation, contact ponctuel

Laboratoire (s) de recherche :Laboratoire de Mécanique des Contacts et des Structures (LaMCoS)

Directeur de thèse: P. Vergne, D. Philippon, G. E. Morales-Espejel

Président de jury :

Composition du jury : J. Cayer-Barrioz, R. Glovnea, I. Křupka, D. Philippon, J. Seabra, P. Vergne, N. Fillot, G. E. Morales-Espejel